Dissertation
submitted to the
Combined Faculties for the Natural Sciences and for Mathematics
of the Rupertus Carola University of
Heidelberg, Germany
for the degree of
Doctor of Natural Sciences

presented by
Diplom-Physicist **Udo Weigel**
born in Mannheim

Oral examination: 26th November 2003

Cold Intense Electron Beams from Gallium Arsenide Photocathodes

Referees: **Prof. Dr. Andreas Wolf**
Prof. Dr. H.-Jürgen Kluge

Kurzfassung

Kalte intensive Elektronenstrahlen aus
Gallium Arsenid Photokathoden

Für die Anwendung von Gallium Arsenid mit negativer Elektronenaffinität als Quelle kalter intensiver Elektronenstrahlen wurde die Elektronentransmission des Halbleiter-Vakuum Übergangs mittels der Messung von Energieverteilungen der photoemittierten Elektronen untersucht. Es konnte durch eine verbesserte Transmission die Ausbeute an kalten Photoelektronen mit einer Aktivierung von nur 0.7 Monolagen Cäsium Bedeckung um 30-50% gegenüber konventioneller Aktivierung gesteigert werden. Bei der Beschränkung der Photoelektronenverteilung auf den mit der GaAs-Temperatur thermalisierten Teil bei 77 K wurde für Photokathoden mit reproduzierbar hohen Quantenausbeuten eine Ausbeute an kalten Elektronen von $\approx$ 1.3-1.5% erzielt.
Der Einsatz dieser Elektronenquelle in der neuen Elektronentargetsektion (ETS) des Speicherrings TSR mit Elektronenströmen von etwa einem Milliampere erfordert bei den erreichten Quantenausbeuten für kalte Elektronen ein Beleuchtung mit bis zu einem Watt Laserleistung. Die sich bei hoher Laserleistung ergebende sehr starke Aufheizung des GaAs konnte mit dem Bau einer neuen Elektronenkanone deutlich reduziert werden, was ihren Betrieb bei hohen Elektonenströmen ($>$ 1 mA) ermöglicht und die Photokathode bei Temperaturen um 95 K stabilisiert. Desweiteren wurde mit der Implementierung einer neuen, im Vakuum anwendbaren Grundreinigungsmethode der Photokathoden mittels atomarem Wasserstoff praktisch ein geschlossener Betriebszyklus der Photokathoden unter Vakuum ermöglicht.

Abstract

Cold Intense Electron Beams from
Gallium Arsenide Photocathodes

For the application of gallium arsenide with negative electron affinity as a source of cold intense electron beams, the transmission of the GaAs-vacuum interface was studied by measurements of the photoelectron energy distribution. It was found that the yield of cold electrons was increased by 30-50% for activations with only 0.7 monolayers of cesium coverage in comparison to conventional activations. For that part of the photoelectron distribution which is thermalized with the GaAs bulk temperature at 77 K a yield of cold electrons of $\approx$ 1.3-1.5% could be achieved for photocathodes with reproducible high quantum efficiencies. The operation of this electron source in the new electron target section (ETS) of the storage ring TSR with electron currents of about one milliampere requires at the achieved cold electron yield a laser illumination of up to 1 W. The resulting strong cathode heating was reduced in a new electron gun arrangement. It enables us to operate at high electron currents ($>$ 1 mA) and to stabilize the GaAs-temperature at about 95 K. Furthermore, with the implementation of a new in-vacuum cleaning technique based on atomic hydrogen it is made possible to operate the photocathodes in a practically closed cycle continuously under vacuum.

Contents

1. Introduction

Electron beams with low energy spreads are a useful tool in several fields of physics like ion collision experiments in atomic physics, scattering and diffraction studies in surface physics (HREELS, LEED) or storage ring applications (electron cooling). The high importance, attached to the low longitudinal and transverse energy spreads of "cold electron beams" arises from the enhanced resolution and performance, reached with these beams. Different methods, aiming at reducing the initial spreads of the broad Maxwell energy distributions obtained for hot electrons in commonly used thermionic emission, are applied. In surface studies, a monochromator selects usually electrons in a small energy window taking the loss of total electron yield. Electron coolers in ion storage rings benefit from a strong decrease of longitudinal spreads in the co-moving frame of the electrons when they are accelerated to be merged with a circulating ion beam at zero relative velocity and additionally low transverse spreads can be achieved by means of an adiabatic transverse expansion technique of the beam-guiding magnetic fields. The electron cooling transfers in Coulomb-interactions energy from the initially hot ion beam to a cold electron beam which is renewed at every circulation. In most ion storage rings, the electron cooler device serves also for ion collision experiments with stored ions. This double usage requires a trade off between providing optimal cooling conditions and optimal conditions for collision experiments.

In a new electron target section (ETS), built at the Max-Planck-Institute for Nuclear Physics, the idea was carried out to combine a separate ETS device, based on electron cooler techniques and dedicated to provide the best possible resolution in ion collision experiments, with an existing electron cooler (see Fig.1.1). At one linear section of the Heidelberg Test Storage Ring (TSR), the electron cooler is installed and the new ETS device was inserted at the following linear section into the storage ring. Molecular and charged fragments as collision products are recorded in detectors placed at the next dipole magnet downstream of the ETS.

One important new idea followed in the development of the new electron target is the use of sources for *initially* cold electrons in contrast to conventional thermally produced electrons. A promising candidate for a cold electron source are GaAs photoemitters. Compared to the energy spreads of thermionic electron guns of ≈110 meV ($T_{\mathrm{cathode}} = 1300$ K), energy spreads of

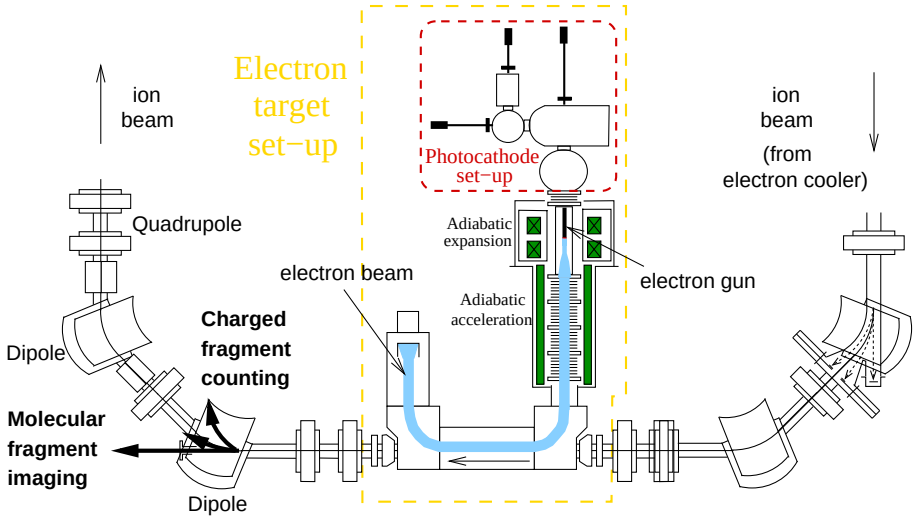

Fig. 1.1: *Overview of the linear section with the the photocathode set-up assembled at the ETS in the storage ring TSR.*

electrons in the conduction band of gallium arsenide under steady state laser illumination are thermalized with the bulk temperature. The GaAs temperature can be chosen freely to some extend and energy spreads at LN_2-cooled GaAs samples are as low as ≈ 8 meV. However, the emitted photoelectron distribution showed noticeable higher energy spreads.

The goal to make a longitudinally and transversely cold and intense electron beam, based on GaAs photoemission, available for the collision experiments at the ETS required to introduce ourselves to semiconductor techniques of sample preparation and handling as well as to study the electron emission process and the photoelectron energy distributions up to the final step of building a GaAs photocathode electron gun with parameters meeting the demands of our application. First measurements of the mean energy distribution for photoelectron sub-ensembles, performed with a test electron gun, and a preparation of GaAs samples up to quantum yields comparable to reported values in semiconductor physics was obtained by [Pas97]. Complete electron energy distributions as a function of their longitudinal and transverse degree of freedom were measured for the first time by Orlov *et al.* [Orl01a].

In this work, decisive steps were done to achieve in practice intense and cold electron beams from GaAs photocathodes. First, the electron yield with respect to the cold part of the photoelectrons was optimized by a factor of 1.3-1.5 in the preparation technique. A cleaning procedure based on atomic hydrogen was implemented and tested. It enables us to refresh samples in vacuum and operate practically with a set of four samples for a few months without opening any part of the set-up to atmosphere in this time. A new cryoelectron gun was designed, built and the sample heating problem at the operation under high laser illumination was solved. A

main point was the operation of the photocathode under strong laser illumination ($\approx$ 1 W) at low temperatures ($\approx$ 90 K). Thus, the thermal conductance between the sample and the LN_2-reservoir had to be optimized in a new construction. This new arrangement was built and it was shown that the GaAs samples indeed remain at $T \lesssim 95$ K at laser illuminations of 1 W. This set-up was constructed directly for integration into the ETS and its installation is currently in progress.

The following chapter reviews the present understanding of the GaAs surface state allowing for electrons in the conduction band to be emitted to the vacuum and the photoemission process. Photoelectron energy distributions and electron beam transport principles are introduced. Essential elements of photocathode handling and operation are discussed in chapter 3. In chapter 4, the underlying photoelectron energy measurement techniques and results of studies on the transmission of the semiconductor-vacuum interface and low temperature operation are presented. Obtained yields for cold electrons and results on the implemented atomic hydrogen cleaning technique are reported. Chapter 5 is dedicated to the new cryogenic GaAs-photoelectron gun. The conclusion and an outlook on the photocathode project at the ETS in chapter 6 will be given.

2. GaAs(Cs,O) photocathodes and electron beam formation

In studies on deposition of cesium and oxygen on the surface of p-doped GaAs, Scheer and van Laar discovered in 1965 a surface state characterized by a vacuum level located energetically below the level of the conduction band minimum in the GaAs bulk. This state of effective negative electron affinity (NEA) allows electrons excited to the conduction band, after tunneling through a surface potential barrier, to escape to the vacuum. That opened up a development of efficient NEA-GaAs photoemitters.
A concept of NEA formation will be presented in section 2.1. Section 2.2 is dedicated to the photoemission from NEA-GaAs and recombination processes competing with the emission of excited electrons to vacuum. Possible practical limits in the operation of GaAs(Cs,O) photocathodes at high electron dc-currents of a few milliamperes are discussed in section 2.4. The closing section 2.5 is concerned with the principles of the electron beam transport at the electron target and with the basics of photoelectron energy distribution analysis.

2.1 Concept of effective negative electron affinity formation

The energy band diagram at an p^+-GaAs/vacuum interface is illustrated in Fig.2.1 (a). Gallium arsenide features at room temperature a band gap energy (E_{gap}), given by the spacing between the conduction band minimum (E_{cbm}) and the valence band maximum (E_{vb}) of 1.42 eV. In the GaAs bulk, p-doping with zinc fixes the Fermi level close to the acceptor level in the vicinity of E_{vb}[1].
The work function φ is defined as the minimum energy necessary for an electron at the Fermi level (E_{F}) to overcome the surface barrier and escape to the vacuum (E_{vac}). The respective minimum escape energy for electrons located energetically at E_{cbm} is given by the electron

1 The shallow acceptor ionization energy of Zn in GaAs amounts to ≈ 25 meV [Mil73]. Nevertheless, additional levels and many-body effects by clustering of Zn dopants at high doping levels [Ebe99] broaden the acceptor levels in a way that the situation comes close to an *acceptor band*.

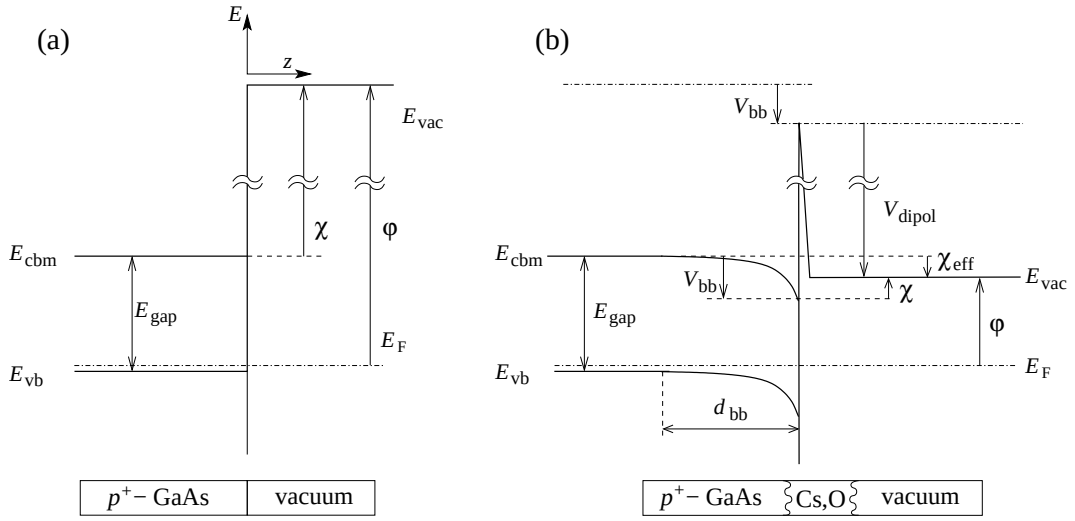

Fig. 2.1: *Sketch of the electronic conditions at the strongly p-doped* GaAs-*vacuum interface before (a), and after activation to negative electron affinity (b), by deposition of (*Cs,O*) on the surface.*

affinity χ and amounts in case of GaAs to about 4 eV [Ada85].

In case of highly p-doped GaAs, a deposition of cesium and oxygen can reduce the vacuum level strongly, shown in Fig.2.1 (b). The *effective* electron affinity, defined with respect to the conduction band minimum *in the bulk* as $\chi_{\mathrm{eff}} := E_{\mathrm{cbm,bulk}} - E_{\mathrm{vac}}$ even takes negative values. This favorable energetic situation, referred to as *effective* **n**egative **e**lectron **a**ffinity, enables conduction band electrons to be emitted to the vacuum after tunneling through a thin residual surface barrier. Several structures of the (Cs,O)-activation layer have been proposed for the formation of NEA [Sch65, Fis72, Ueb70, Bur78]. However, the results of comparative studies on the role of the oxidizing species (showing no significant influence with respect to their chemical nature [Pas96, Cic91]), and of photoelectron energy distribution measurements as a function of the (Cs,O) layer thickness (showing rising NEA and subsequent saturation at higher thicknesses for commonly used activation layers of 1-2 monolayer (Cs,O)-coverage [Orl01b]) are only consistent with the (double) dipole layer model.

Two additive effects provoke the lowering of E_{vac} at the surface, at one side a band bending (V_{bb}) and on the other side the potential of the dipole surface layers (V_{dipol}).

Band bending effects originate from donor-like surface states contributing their electrons to the bulk. The positive charge of these surface states is compensated by an accumulation of negatively charged acceptors accompanied by a depletion of holes within a distance d_{bb}. The enhanced occupancy of bulk acceptors in the surface-near region is described with a downwards shift of E_{vb} by the value V_{bb}. By the same amount V_{bb}, the work function φ is decreased.

The donor-like surface states, which can be present even prior to the deposition of cesium on the surface in form of defect-induced states, were found to be dominated by cesium adsorption [Alp94, Alp95b]. In order to provide favorable conditions for the photocathode application, i.e. high V_{bb} and low d_{bb}, a high doping level of $\mathrm{n_{Zn}} \approx 5 \cdot 10^{18}\mathrm{cm}^{-3}$ is employed with reported values for V_{bb} of 0.3-0.5 eV [Alp95a, Dro85] at typical dimensions d_{bb} of ≈ 10 nm.

A majority of the Cs-adatoms becomes only polarized and electrons remain with the cesium atom. The resulting dipole layer on the surface can be compared in a simple picture to a parallel-plate capacitor and leads to a strong decrease of the vacuum level close to E_{cbm}. Co-deposition of oxygen enhances the lowering to V_{dipol} (see Fig.2.1 (b)). This effect is still not completely understood. It can be interpreted in some models as formation of additional dipole layers on top of the initial one [Fis72].

2.2 NEA photoemission

Three steps characterize the photoemission from NEA-GaAs according to an early model by Spicer *et al.* [Spi77, Spi58], the excitation of an electron by photon absorption, the transport of the electron to the surface and its emission to the vacuum (see Fig.2.2 (a)).
The absorption of exciting photons is described in the vicinity of the band gap of GaAs by an absorption coefficient $\alpha(\mathrm{h}\nu_{\mathrm{ex}}) \propto \sqrt{\mathrm{h}\nu_{\mathrm{ex}} - E_{\mathrm{gap}}}$ and typical absorption lengths of $\alpha^{-1} \approx 1\ \mu$m for $\mathrm{h}\nu_{\mathrm{ex}}$ slightly above E_{gap}. Figure 2.2 (b) illustrates this process in the energy momentum diagram. Due to the photon energy $\mathrm{h}\nu_{\mathrm{ex}}$ and negligible photon momentum, the excitation is represented by vertical arrows of length $\mathrm{h}\nu_{\mathrm{ex}}$. Only those electrons in the heavy hole (hh), light hole (lh) and split-off (so) subbands with a specific set of $\vec{k}$-vectors matching the energy and momentum conservation condition can be excited to the conduction band. Therefore, the final energetic position is determined by the excitation energy and the band structure of GaAs. In a second step, electrons undergo relaxation and thermalize at the conduction band minimum. Emission of phonons[2] and scattering of electrons with heavy holes accompanied by hh−lh conversion, especially at high doping levels (above $\approx 10^{18}\mathrm{cm}^{-3}$ [Zak82]) and accordingly high hole densities, are the main energy loss mechanisms (see Fig.2.2 (b)). The time of hot electrons to be thermalized in the conduction band amounts to typically 10^{-13}-10^{-12}s, corresponding to thermalization lengths of about 100 nm. Thermalized in states close to the conduction band minimum, electrons live typically about nanoseconds before they recombine with holes in the valence band. The respective diffusion length amounts to 4-5 μm. In the third step, electrons reaching the surface cross the band bending region and tunnel through the thin barrier to

2 Typical energies of longitudinal optical phonons are $E_{\mathrm{phonon}} \approx 35$ meV.

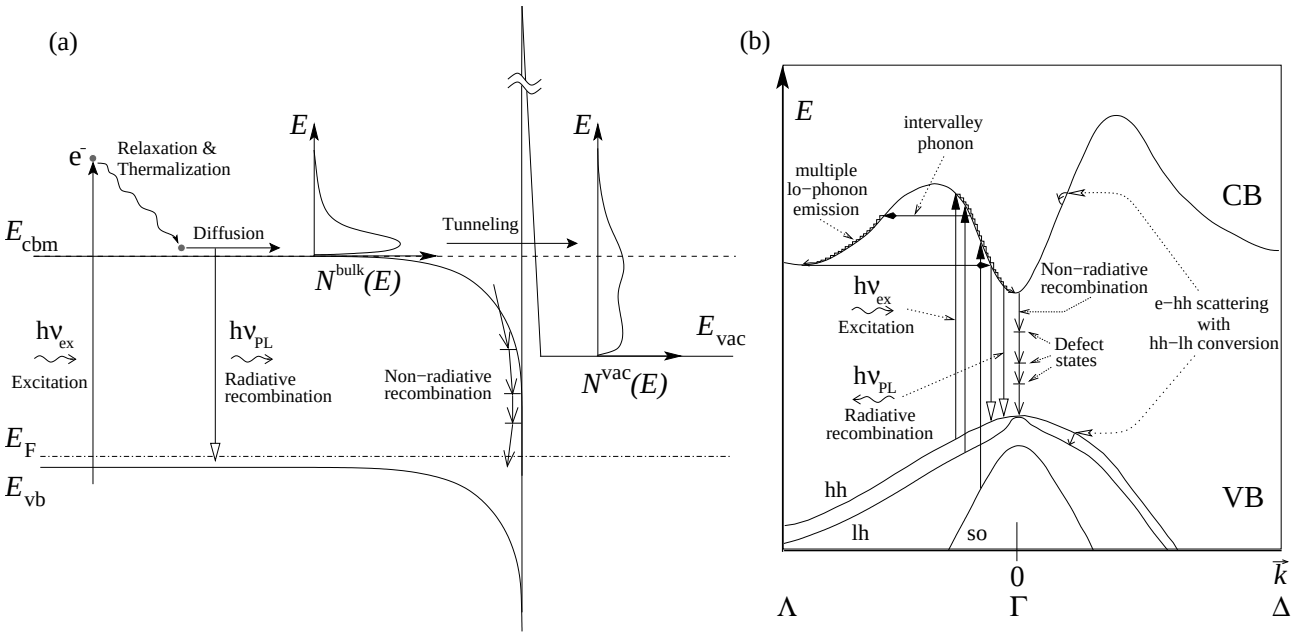

Fig. 2.2: *(a) Sketch of the photoemission and competing recombination processes in the electronic band diagram. (b) The excitation, the dominating thermalization mechanisms (lo-phonon emission and e-hh scattering with hh-lh conversion) as well as recombination processes are indicated in the E-$\vec{k}$−diagram.*

escape to the vacuum. In the final step, a more complex emission mechanism than assumed by the simple Spicer model was proved by strong energy loss and momentum relaxation in photoelectron energy distributions (see section 2.3).
In order to estimate the efficiency of the photoemission process, the quantum efficiency QE is defined as photoelectron yield (N_{el}) per irradiated photons ($N_{\mathrm{h}\nu}$):

$$QE = \frac{N_{\mathrm{el}}}{N_{\mathrm{h}\nu}} = \frac{\mathrm{h}\nu}{\mathrm{e}} \frac{I_{\mathrm{ph}}}{P_{\mathrm{light}}}, \tag{2.1}$$

with photocurrent I_{ph} and laser power P_{light}. Radiative and non-radiative recombination processes in the bulk and at the surface (see Fig.2.2), competing with the electron emission, reduce the QE.

Excited electrons can recombine with holes in the valence band radiatively under emission of a photoluminescence (PL) photon with energy $\mathrm{h}\nu_{PL} \approx E_{\mathrm{gap}}$[3]. The non-radiative recombination probability of excited electrons is strongly enhanced in multiple step deexcitation via inner band states. Since the density of these defect states is very high near the semiconductor-

3 It allows for probing E_{gap} in the bulk accurately since it is quite insensitive to surface effects (cp. PL temperature measurements p.35).

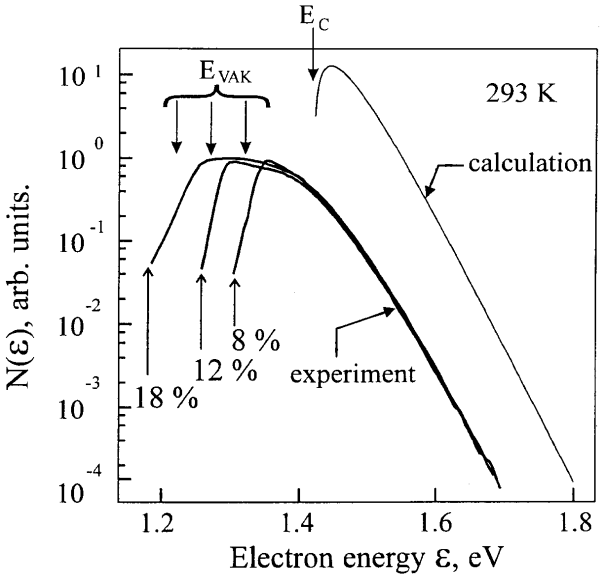

Fig. 2.3: *Comparison of longitudinal energy distributions [Ter95] in the* GaAs *bulk (thin line) with photoemitted distributions taken at different activation steps of the* GaAs*-photocathode (QE = 8%, 12% and 18% corresponding to different values of* $\chi_{\text{eff}} := E_{cbm,bulk} - E_{vac}$*). The longitudinal energy scale is referred to* E_{F}*.*

vacuum interface, excited electrons are drained efficiently to lower states at the surface and give up their energy to the GaAs surface region. Holes are supplied to the near-surface depletion region from the bulk and recombine with the deexcited electrons.

2.3 Photoelectron energy distributions

Under steady-state conditions of dc-illumination with photon energies slightly exceeding E_{gap}, the thermalized electron energy distribution *in the bulk* is well understood. It follows the multiplied density of states in the conduction band ($\propto \sqrt{E - E_{\text{gap}}}$) with the Boltzmann distribution. The emitted photoelectron distribution can be characterized by their longitudinal energy, viz the energy corresponding to an electron momentum perpendicular to the semiconductor surface, and the transverse energy component (cp. section 2.5.1).

Longitudinal photoelectron energy distributions

Figure 2.3 (reproduced from [Ter95]) shows a comparison of longitudinal energies measured for photoemitted electrons with a calculated bulk distribution. Three vacuum levels represent different activation steps to the indicated QE. The experimental high energy tail above E_{cbm} follows well the calculated thermalized exponential shape, differs however by almost two orders of magnitude in size; the electron transmission through the surface barrier could be obtained

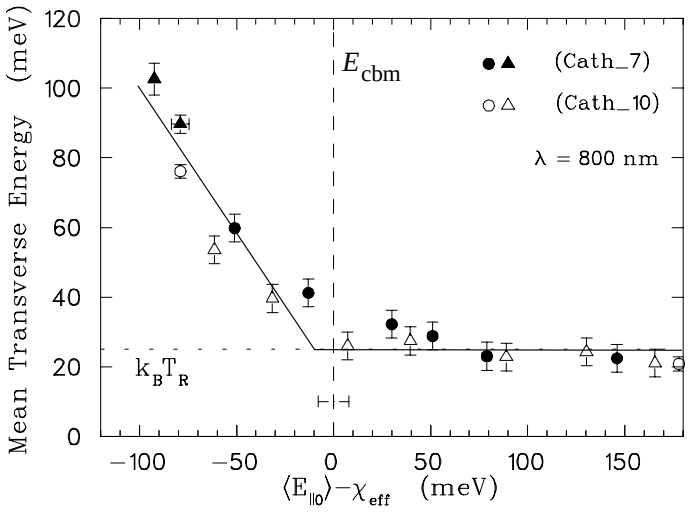

Fig. 2.4: *Mean transverse photoelectron energy distribution for subensembles defined by a minimum longitudinal energy. The abscissa indicates the mean longitudinal energy of the ensemble referred to* E_{cbm}*. Data was taken for two different (*Cs,O*) activated cathodes at room temperature.*

quantitatively in this experiment. One can see that a longitudinally *thermalized* subensemble of photoelectrons, suited for the production of thermalized electron beams, can be obtained at higher energy. Below E_{cbm}, the extension of the experimental curves to E_{vac} indicates an energy (or momentum) transfer towards lower energy (or higher transverse momentum) at the emission process. Known energy loss mechanisms in the band bending region may contribute to the energy transfer, but are insufficient to explain alone longitudinal energy losses of the observed degree. The nature of possible additional energy loss mechanisms (cp. [Ter95, Orl00, Kir83]) can not be accessed by the longitudinal energy distribution curve (long. EDC), since distinguishing of elastic or inelastic scattering processes requires information on the transverse energy component.

Transverse and complete photoelectron energies

Studies based on the principle of adiabatic transverse expansion of magnetized electron beams (see section 2.5) performed by Pastuszka *et al.* [Pas97] allowed to access the *mean* transverse energy (MTE) for subensembles of photoelectrons in dependence of their mean longitudinal energy (MLE), see Fig.2.4. The results show an almost constant MTE close to $k_{\mathrm{B}}T_{\mathrm{RT}}$ ($\approx$ 25 meV) for subensembles with MLEs above E_{cbm} (corresponding to E_{c} in figure 2.3). At lower longitudinal energy, the figure reveals strongly enhanced mean transverse energies. A method developed by Orlov *et al.* [Orl01a] at the Max-Planck-Institute for Nuclear Physics, applying an adiabatic compression technique, accessed for the first time the complete photoelectron energy distribution and was employed in a similar way (method, see section 4.1) in studies on the

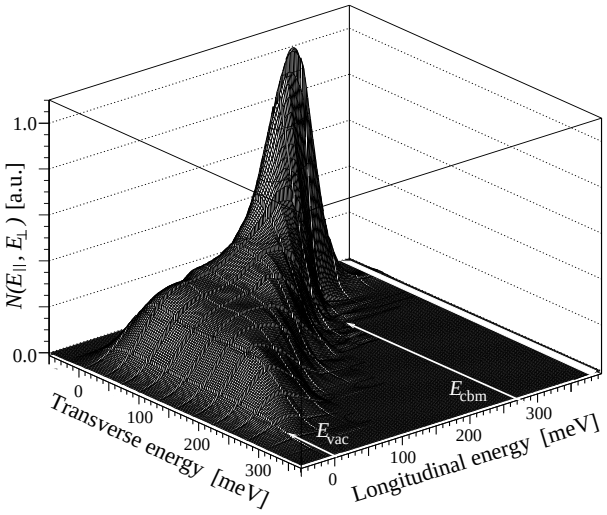

Fig. 2.5: *Two-dimensional photoelectron distribution as a function of the longitudinal and transverse energy [Orl01a]. The* GaAs(Cs,O) *photocathode was activated to maximum quantum efficiency at* χ_{eff} *= 280* meV*. Energies are referred to* E_{vac}*.*

transmission of the residual surface potential barrier [Orl01b] and on cryogenic sample temperature [Orl03] (see sections 4.4, 4.2). Figure 2.5 features an exponential drop of the electron yield above E_{cbm} with an e^{-1}-interval of $\approx k_{\text{B}}T_{\text{bulk}}$ in the longitudinal *and* transverse direction. This subensemble of the distribution proved to be suited for the production of longitudinally and transversely thermalized photoelectron beams (see chapter 4.3). Below E_{cbm}, contributions at transverse energies between 100-300 meV demonstrated the influence of elastic and inelastic scattering during the passage of electrons through the GaAs(Cs,O)−vacuum interface. Further studies of energy distributions with this experimental method, aiming to optimize the yield of cold electrons were performed in this work (see chapter 4).

2.4 Photocathodes operated under high laser illumination

The definition of quantum efficiency implies a linear photocurrent response on the power of the irradiated light. However, deviation from this behavior due to **surface photovoltage** were found at higher light intensities with a significantly lower electron yield. This saturation effect is a sign of an electron accumulation at the semiconductor surface. At moderate light intensities, excited electrons recombine with holes sufficiently fast at the surface. With an increasing number of electrons, a limited recombination rate could result in their partial trapping in surface states. Recombination at the surface requires an efficient hole transport, which is dominated by tunneling for strongly *p*-doped GaAs [Jar97], to the hole depletion region near

the surface. The raised negative space charge at the surface reduces in consequence the band bending and the negative electron affinity, respectively, leading to a reduced quantum yield with higher light intensities [Her96]. Well prepared cathodes, however, are in the linear regime up to laser intensities of a few W/cm^2 [Ter98]. Finite residual rises of $|\chi_{\text{eff}}|$ due to surface photovoltage effects can be accounted for in the beam preparation by an appropriate cutting of the emitted distribution as mentioned at the end of section 4.4.

Photoemission and radiative recombination lead away most part of their excitation energy with the photoelectron and the photoluminescence photon, respectively. The dominating process, the non-radiative recombination, in contrast contributes the excitation energy of the electrons to the GaAs bulk which is heated up in consequence. Energy contributions caused by thermalization in the bulk can be efficiently minimized by an appropriate choice of the excitation laser light with photon energies only slightly above E_{gap}. Nevertheless, heating effects during a high laser illumination have to be taken into account at the photocathode operation. Therefore, efficient cooling is required. The necessary technical developments to make possible a high current operation are studied in this work (see section 5.1).

2.5 Electron beam transport principles

2.5.1 Magnetized electron beams

Their common space charge constantly subjects the electrons forming a beam to Coulomb repulsion. In order to avoid a beam divergence, a longitudinal magnetic field along the beam axis z can suppress this effect and confine the electrons, if the field strength B_z exceeds the electron density dependent, so-called *Brillouin*-field [Jan90]:

$$B_{\text{B}} = \sqrt{\frac{2n_e \cdot m_e}{\epsilon_0}}, \tag{2.2}$$

n_e denotes the electron density. For the electron densities used in the studies on the electron energy distributions ($\lesssim 10^5$ cm^{-3}), B_{B} amounts to a few Gauss, whereas the magnetic guiding field was greater than 500 Gauss. In addition, the strong magnetic field decouples the longitudinal and the transverse degree of freedom, such that beam temperatures, defined via the standard deviation of the electron velocity distribution, can be separated:

$$\frac{1}{2}k_{\text{B}}T_{\parallel} = \frac{1}{2}m_e\Big(\langle v_{\parallel}^2\rangle - \langle v_{\parallel}\rangle^2\Big), \tag{2.3}$$

$$k_{\text{B}}T_{\perp} = \frac{1}{2}m_e\Big(\langle v_{\perp}^2\rangle - |\langle \vec{v}_{\perp}\rangle|^2\Big). \tag{2.4}$$

In the beam center, due to vanishing mean transverse velocity, the transverse temperature equals the mean transverse energy (MTE)

$$k_{\mathrm{B}}T_{\perp} = m_e\langle v_{\perp}^2\rangle = \langle E_{\perp}\rangle. \tag{2.5}$$

In the beam rest frame the mean longitudinal velocity vanishes ($\langle v_{\parallel}\rangle = 0$) and the mean longitudinal energy (MLE) is given by:

$$\frac{1}{2}k_{\mathrm{B}}T_{\parallel} = \langle E_{\parallel}\rangle. \tag{2.6}$$

An acceleration of the electron beam by the potential Φ reduces the longitudinal beam temperature in the rest frame. At non-relativistic velocities, the longitudinal temperature after acceleration (denoted by the index $'$) can be described by the kinematic transformation :

$$\frac{1}{2}k_{\mathrm{B}}T'_{\parallel} = \frac{(k_{\mathrm{B}}T_{\parallel})^2}{4e\Phi} = \frac{\langle E_{\parallel}\rangle^2}{\langle E'_{\parallel}\rangle}. \tag{2.7}$$

The transverse temperature remains, however, unaffected by the acceleration:

$$k_{\mathrm{B}}T_{\perp} = \langle E'_{\perp}\rangle = \langle E_{\perp}\rangle. \tag{2.8}$$

2.5.2 Adiabatic magnetic field change

Passing through a region of spatially varying magnetic field strength, the electrons are accelerated by a longitudinal component of the Lorentz-force $\vec{F}_{\mathrm{L}}$. Since $\vec{F}_{\mathrm{L}}$ is still perpendicular to $\vec{v}$, energy conservation holds:

$$E_{\mathrm{tot}} = E_{\parallel} + E_{\perp} = const.\ , \tag{2.9}$$

For a sufficiently slowly (adiabatic) varying magnetic field,

$$\frac{E_{\perp}}{B} = const. \tag{2.10}$$

is an adiabatic invariant [Jac98]. Adiabaticity is evaluated by the parameter ξ, defined as the product of the relative magnetic field change and the spiral length of a cyclotron revolution, λ_c:

$$\xi = \frac{\lambda_c}{B}\cdot\left|\frac{dB}{dz}\right| \text{ with } \lambda_c = \frac{2\pi}{eB}\cdot\sqrt{2m_eE_{\parallel}}, \tag{2.11}$$

which should be small compared to unity. In the apparatus described below (see section 4.1.2), used in the studies of electron energy distributions, values of ξ amounting to ≈ 0.0014

were reached. After an adiabatic passage from the initial longitudinal field B_i to the final longitudinal field B_f, the longitudinal energy $E_{\parallel f}$ is given by eqn.2.9 and 2.10 as:

$$\begin{aligned} E_{\parallel f} &= E_{\parallel i} + (1-\alpha)\, E_{\perp i} \\ E_{\perp f} &= E_{\perp i} - (1-\alpha)\, E_{\perp i}, \end{aligned} \tag{2.12}$$

where α denotes the ratio of final and initial longitudinal field strength:

$$\alpha = \frac{B_f}{B_i}. \tag{2.13}$$

Due to Coulomb interaction, the adiabatic invariant for a single electron (eqn.2.10) does not necessarily hold for dense electron ensembles. However, for strongly magnetized beams it can be shown [O'N85], that

$$\frac{\langle E_\perp \rangle}{B} = const.. \tag{2.14}$$

The adiabatic invariant 2.10 can alternatively be phrased by

$$R^2 \cdot B = const.\ , \tag{2.15}$$

with R denoting the electron beam radius. Thus, in a spatially increasing magnetic field ($\alpha > 1$) the beam diameter decreases. This process is called adiabatic transverse compression and was applied for the electron distribution studies in order to transfer a controlled part of the transverse electron energy to the longitudinal degree of freedom according to eqn. 2.13 (cp. section 4.1.2). The opposite case, an adiabatic transverse expansion (ATE), leads to a decrease in transverse energy from $\langle E_{\perp i} \rangle$ to $\langle E_{\perp f} \rangle = \alpha \langle E_{\perp i} \rangle$. It is employed up to expansion factors $\alpha = 1/40$ at the new electron target set-up to decrease the transverse energy spreads of the electron beam [Sch00, Spr03].

2.5.3 Relaxation processes

In order to investigate electron-ion interactions at low relative velocity in the ETS, the produced electrons have to be accelerated to the respective ion velocity. This longitudinal expansion of the electron beam leads to a strongly anisotropic ensemble with respect to its longitudinal and transverse distribution, which can show relaxation phenomena as discussed here:

Longitudinal-longitudinal relaxations

Inside the beam, prior to the acceleration, the kinetic energy and the potential energy with

respect to the Coulomb repulsion of the electrons are in equilibrium. After acceleration, an increased potential energy related to the anisotropic density distribution relaxes into kinetic energy. Due to magnetic decoupling of the transverse temperature from the longitudinal one, the main effect of relaxations is an increase of the longitudinal temperature. This so-called longitudinal-longitudinal relaxation (LLR) results in an additional contribution to the longitudinal beam temperature of [Jan90, Kra92]:

$$\delta E_{\parallel}^{\mathrm{LLR}} = \frac{1}{2} \cdot C \cdot \frac{e^2 n_e^{1/3}}{4\pi\epsilon_0} \tag{2.16}$$

where n_e denotes the electron density and the particular mode of acceleration is quantified by the value of C (of the order of one). At the higher acceleration voltages used at the ETS, this term limits the longitudinal temperature [Sch00].

Transverse-longitudinal relaxation

The anisotropy in the longitudinal and transverse temperature leads to the relaxation of kinetic energy in binary collisions [Kud82]. The increase of the much smaller longitudinal temperature in this transverse-longitudinal relaxation (TLR) is enhanced with higher electron density and drift time but can be suppressed by a strong magnetic field. A discussion of TLR at different regimes in the ETS can be found in Sprenger *et al.* [Spr03].

Both contributions add up to the final longitudinal temperature

$$\frac{1}{2} k_{\mathrm{B}} T_{\parallel}^{\mathrm{relax}} = \frac{1}{2} k_{\mathrm{B}} T'_{\parallel} + \delta E_{\parallel}^{\mathrm{TLR}} + \delta E_{\parallel}^{\mathrm{LLR}}. \tag{2.17}$$

All studies of electron energy distributions, performed in this work, used low electron densities, so that the relaxation effects were negligible. This was also tested experimentally. The influences from relaxation on the studies of the electron distribution in chapter 4 were estimated by the measured broadening of an initially longitudinally well defined electron ensemble in dependence of the electron density in the beam. The width of the distribution was found to be determined by the resolution of the analyzer (analyzer transmission is well described by a fitted Gaussian with $\sigma_{\parallel} \approx 17$ meV) at the electron densities used in this thesis.

3. Photocathode handling and operation

Negative electron affinity formation and photoemission from NEA-GaAs cathodes are extremely surface-sensitive processes. They put high demands on base vacuum conditions and residual gas composition and require a careful control of the multi-step cathode preparation procedure. Contamination of the surface at any preparation step or during the cathode operation make a direct negative impact on the quantum efficiency, transverse electron energy spread and lifetime of the photocathode and as a result on the performance of the electron gun. Hence, handling and operation should aim to provide the best conditions from the first step of the surface cleaning up to the final emitter application at the electron target. After an introduction to our photocathode samples in 3.1 and a description of the experimental set-up in 3.2, section 3.3 is dedicated to the presentation of the surface cleaning techniques and the surface activation procedure. Practical operation limits as well as the present lifetimes of the cathodes and activation layers, respectively are finally discussed in section 3.4.

3.1 Samples

Photocathodes used in this thesis were produced at the Institute of Semiconductor Physics in Novosibirsk. Three different cathode types are utilized, shown in Fig.3.1. In general, there are two kinds of photocathodes distinguished according to the basic operation with respect to the incident laser light, reflection mode (c) and transmission mode (a,b) types. Those samples designed for illumination from the front (reflection mode) are technologically easier to fabricate and in consequence commercially available.
Our reflection mode semiconductor structure consists of a GaAs wafer (ϕ x h = 6 mm x 400 μm) cut from liquid encapsulated Czochralski (LEC) grown undoped bulk crystals and a Zn-doped ($n_{\mathrm{Zn}} = 5 \cdot 10^{18}$ cm^{-3}) GaAs epilayer grown by liquid phase epitaxy in orientation (100) $\pm$ 0.5°. The wafer is soldered directly to the titanium holder.
The transmission mode cathode with a glass substrate (a) and sapphire substrate (b) are based on the same GaAs/AlGaAs heterostructure grown by liquid phase epitaxy. These structures are thermo-compression bonded to the substrates (see Fig.3.2) and metallized for electrical

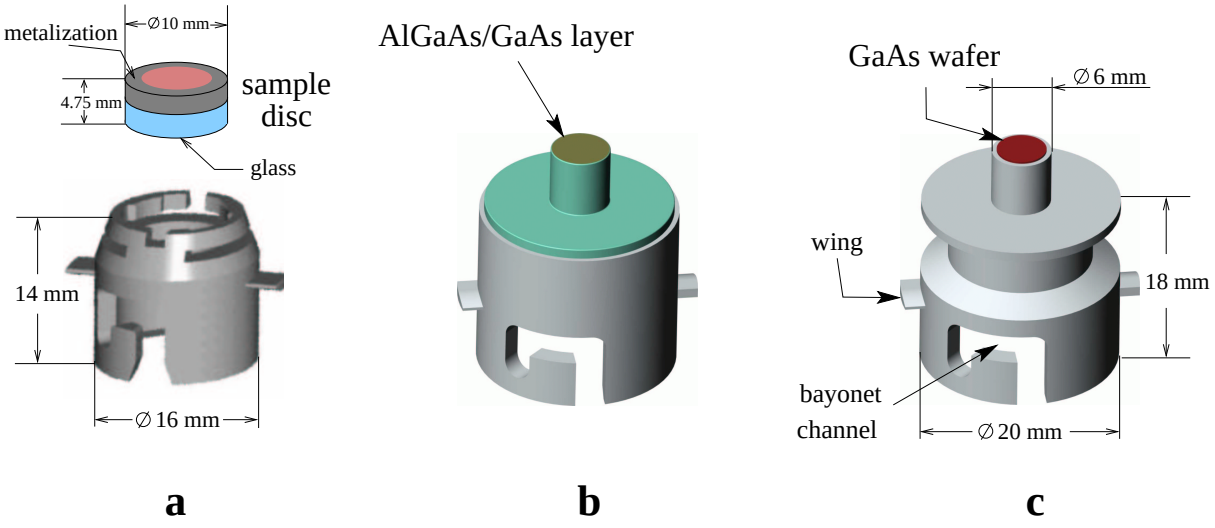

Fig. 3.1: *Three different photocathode types with sample holders: A transmission mode photocathode used in the test electron gun (a), the transmission mode type designed for the new cryogenic electron gun (b) and a reflection mode photocathode (c) for use in the new gun.*
All metal holder parts were made of titanium and employ the same concept of bayonet-joints to the manipulators and wings for fixation in the different positions of the vacuum set-up. Principal sizes of type (b) correspond to those indicated in (c).

contact. The active p^+-GaAs layer was prepared with the same doping level and doping species as mentioned before in case of reflection mode cathodes. Thicknesses amount to 1.5 μm in case (a) and 2 μm in case (b). These thin layers are chosen to combine almost complete light absorption by photoelectron excitation ($\lambda_{\mathrm{abs,GaAs}} \approx 1$ μm for the used wavelength) with limited diffusion paths ($\lambda_{\mathrm{diff,GaAs}} = 4\text{-}5$ μm) for conduction band electrons to reach the surface. An AlGaAs buffer layer of 2 μm with a bandgap exceeding that of the active layer provides a back-side potential barrier. This avoids deep diffusion of excited photoelectrons in the semiconductor and keeps them close to the surface which results in enhanced electron escape probability. An anti-reflection coating optimizes the laser light transmission at the semiconductor-substrate interface to reduce the light reflection from about 30 % to 5-7 % at the required wavelength. For thermal reasons (see chapter 5) the new transmission mode photocathode (b) is based on a sapphire substrate whereas those used in the test electron gun measurements (a) are bonded to glass. The basic production principle of glass-sealed transmission mode photocathodes is described in [Ant75] and the Novosibirsk group developed the technology for sapphire bonding. For the photocathode transfer inside the vacuum, the samples have to be fixed in the holder. Type (a) holders clamp the substrate laterally by a circular spring mechanism and contact the outer metalization layer (Pd/Ti) of the sample disc. After long term operation for some of

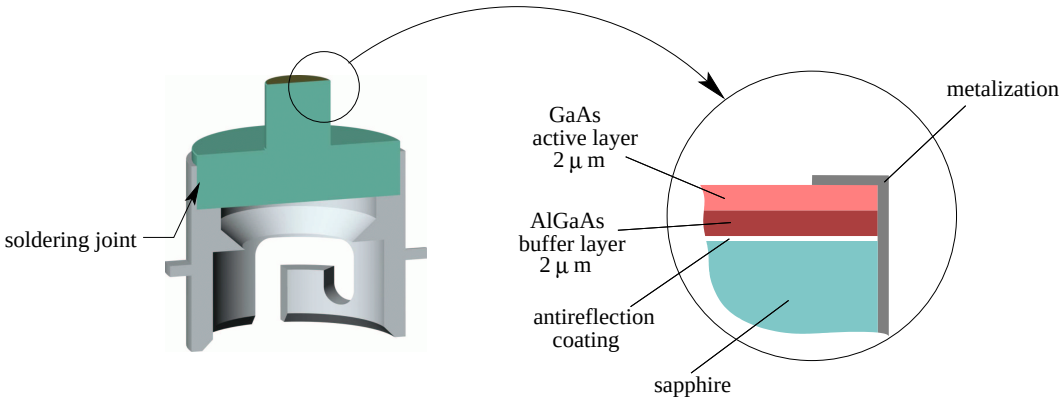

Fig. 3.2: *Layer structure of the new transmission mode photocathode (b) in a* 180°*-cut.*

these holders, a poor electrical contact arose and even the samples were freed. The new holder type is directly soldered and contacted to the sapphire substrate metalization (soldering joint shown in Fig.3.2). Commercial sapphire window blanks, cut in this special shape to meet the geometrical requirements of the new electron gun, served as substrates . The holders can be picked up by magnetically coupled manipulators using a bayonet-joint (see details at Fig.5.7). Two wings permit the fixation of cathodes in different places of the vacuum set-up.

3.2 The photocathode test bench

Our photocathode set-up, shown in Fig.3.3, intended for installation at the electron target, consists of a three parts: The preparation chamber, the loading/hydrogen chamber, and the gun chamber shown in the figure. The photocathode test bench is completed by an electron energy analyzer set-up linked to the gun chamber and by a separate glove box.
Prior to the insertion of cathodes in the vacuum system, the glove box enables wet-chemical treatments under pure nitrogen atmosphere. In the transfer vessel up to four samples could be installed on a target ladder. Pulling back a bellow-sealed spindle drive encloses the ladder hermetically under nitrogen and enables transport to the loading chamber without contact to the laboratory atmosphere. After passing the load lock, the samples can be picked up by manipulators, which place them for the next preparation steps either in hydrogen cleaning position or pass them through a separation gate valve to holders on the carousel of the preparation chamber. The magnetically driven carousel permits to rotate each of its four holders in front of an oven or a Cs-dispenser. Laterally mounted dispensers (labelled “O-dispensers”) expose the sample to oxygen on demand. Viewports in front of two Cs-dispenser and an oven position open up optical access to the photocathode during the treatments.

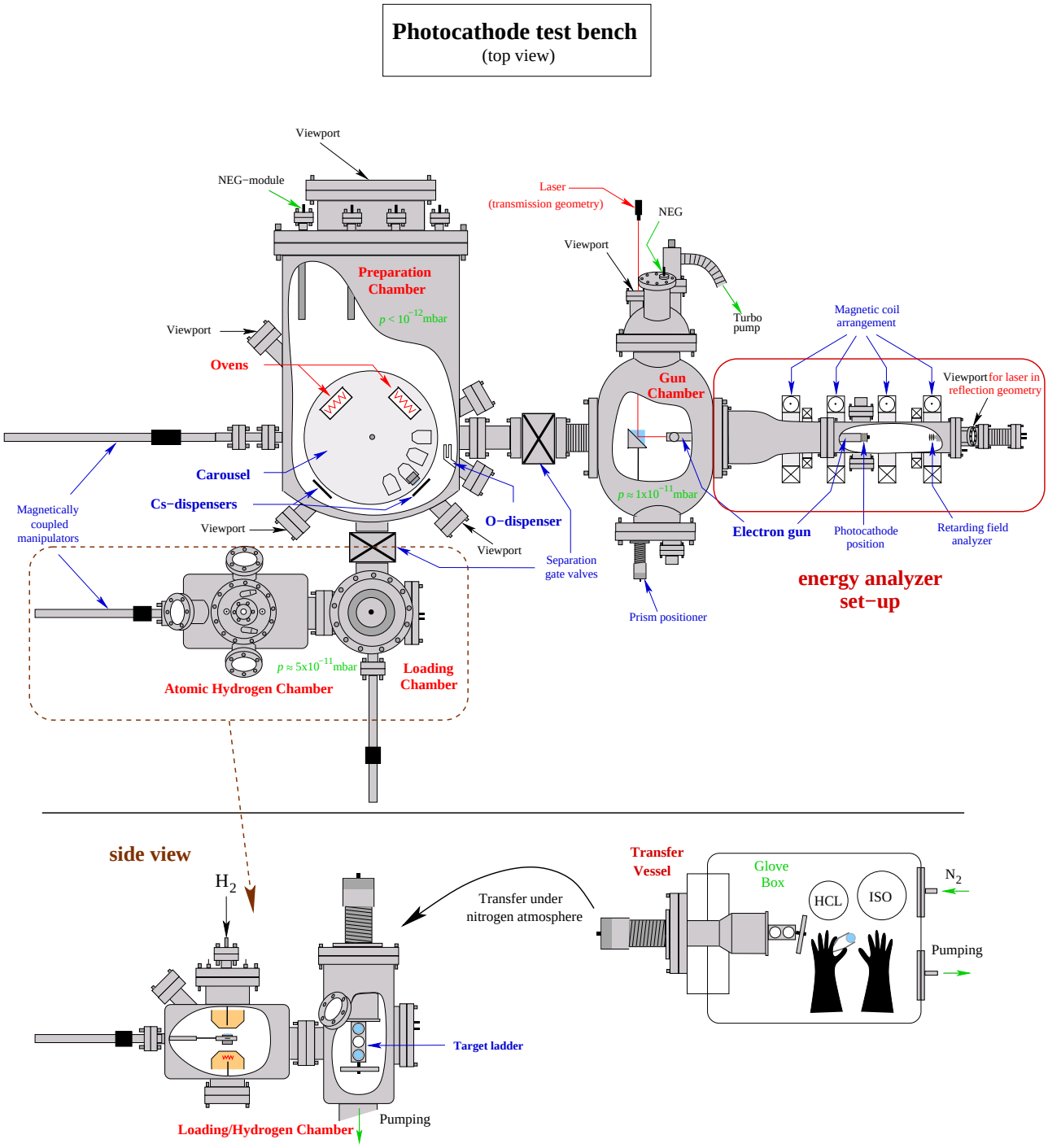

Fig. 3.3: *Photocathode test bench:*
The system consists of the preparation chamber, the loading/hydrogen chamber and the gun chamber with the linked energy analyzer set-up. Before insertion of the photocathodes to the vacuum system, etching procedures are performed in the glove box.

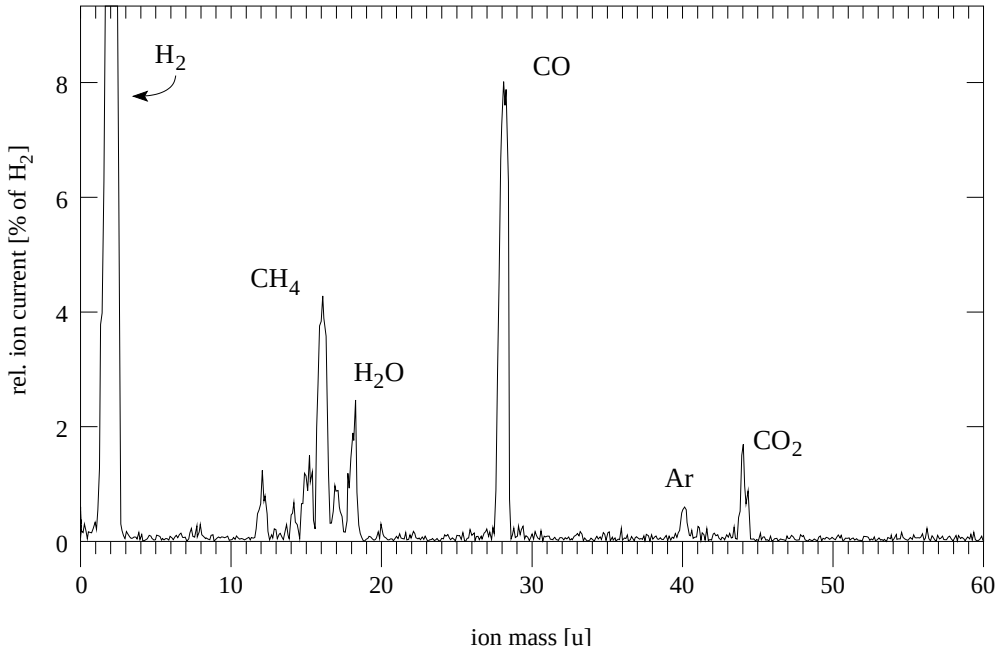

Fig. 3.4: *Measured ion current of the residual gas composition. The data is referred to the height of the hydrogen peak. The total pressure was below* 10^{-12} mbar.

The photocathode can also be handed over to another manipulator which transfers it through a gate valve to the electron gun, assembled in the gun chamber, where an electron energy analysis can be performed. Laser access to the photocathode in the electron gun is provided at one side in transmission geometry via a lateral viewport and a movable prism or at the other side in reflection geometry by direct illumination from the analyzer side.
The main chamber of the system, the preparation chamber, is pumped by an ion getter pump (230 l/s Star Cell, Varian) and eight passive NEG-modules (non-evaporable getter, 8x880 l/s, Saes Getters) attaining a base pressure better than $1 \cdot 10^{-12}$ mbar after a careful bakeout at 300°C. A quadrupole mass spectrometer (QMA 112A, Balzers) attached to the chamber monitors the residual gas composition (Fig.3.4). The strong hydrogen peak dominates the spectrum and other components are referred to it in percent of its peak height. In particular, the harmful species H_2O and CO_2 limit the dark lifetime of activated photocathodes which amount to an e^{-1}-value of typically several 100 hours.

The combined loading/hydrogen chamber is equipped with an ion getter pump (60 l/s) and a turbo molecular pump backed by a diaphragm pump. Samples can be passed on after a few hours of pumping without disadvantageously high pressure rises during the gate valve opening to the preparation chamber. For long term operation in closed state, the pressure in the loading/hydrogen chamber reaches $\approx 5 \cdot 10^{-11}$ mbar after a bakeout at $150 - 200$°C.

Pumping facilities in the gun chamber comprise an ion getter pump (60 l/s), a turbo molecular pump, and a NEG module. In the presented test bench configuration with mounted analyzer set-up (additional ion getter pump and NEG-module), the base pressure amounts to $\approx 1 \cdot 10^{-11}$ mbar. In the configuration at the electron target, the installed beamline pumping in that place strongly influences the final vacuum conditions of the photoelectron gun. The present vacuum at the acceleration region of the target is in the low 10^{-10} mbar range and work to improve it is in progress.

3.3 Surface preparation techniques

The surface of our p^+-doped GaAs semiconductor samples is subjected to a multi-step preparation procedure to obtain the state of effective negative electron affinity. This process can be separated into two major parts: first, several treatment steps provide an atomically clean and flat initial GaAs surface and secondly, the subsequent activation is achieved by controlled deposition of cesium and oxygen on the surface. Related to the first major part, two cleaning methods will be discussed below, on one hand a procedure based on wet-chemical treatment with subsequent heat cleaning and on the other hand a technique which we recently implemented with respect to the requirements of the electron target application, basing on an atomic hydrogen (H·)-treatment. Concerning the second major part, previous comparative investigations of different oxidizing species performed by [Pas97] favored the (Cs,O)-deposition in comparison to a (Cs,F)-activation for its relative simplicity at similar results; the (Cs,O) method will be presented below.
While the dark lifetimes of activated photocathodes, previously reported for our vacuum conditions in [Pas97], are not supposed to cause any limits in the application, the photocathodes suffer from noticeable degradation under operation, e.g. in the electron gun. Fortunately, samples with a performance decreased in such way can be recovered by a partial or full rerun of the initial preparation procedure. The extent of a repeated preparation depends on the degree of degradation and can range from a simple "recesiation" by redeposition of parts of the activation layer on the given surface, via a "reactivation" with a partial removal of the present activation layer prior to a new activation, up to a "refreshing" including a complete removal of all activation layers and a preparation of a cleaned GaAs surface to reobtain its initial surface quality as basis for a new activation. In cases of strongly polluted samples even "drastic" measures like an etching of the emitters with a solution of H_2SO_4 in H_2O_2 and H_2O are taken but, if possible, avoided since this could also lead to a deterioration of the surface morphology and is generally very rarely needed. A "recesiation" recovers the photocathode only in cases of minor degradation and can be repeated very often; a "reactivation" will yield a performance as for

freshly prepared photocathodes only 2-3 times in typical cases. Further reactivations do not fully recover the cathode quality. A "refreshing" either by chemical treatment or by the atomic hydrogen method repeats basically the complete preparation procedure and was successfully done for some of our samples more than fifteen times so far.

3.3.1 Wet-chemical treatment and vacuum annealing

Wet-chemical etching of GaAs surfaces by HCl has proved to make an atomically flat surface structure available extending over a macroscopic area [Kan97, Son95] at a reproducible low concentration of contaminations [Ter99b].
Although an effective removal of all observed native oxides on the GaAs(100) surface, viz Ga_2O_3 and As_2O_3, is consistently reported in all studies for varying HCl concentrations, the residual contamination after the treatment shows differences. In case of etching with concentrated HCl for 10 min, overlayers of gallium chlorides and gallium oxichlorides were formed with a thickness of 2 Å [Son95], whereas an etching with a 3 M solution of HCl in isopropanol (2 min) exhibits solely the $GaCl_x$ contributions in a ≈ 10 times thinner overlayer. Other gallium and arsenic compounds with HCl are not found in these wet-chemical treatments, but arsenic chlorides could be constituted under HCl gas etching at higher temperatures [Sai90].
Chlorine can exist on the GaAs surface as a mixture of $GaCl_x$ with states for x = 1-3. Since $GaCl_3$ and GaCl start to desorb at 80°C and 330°C [Bon98], an atomically clean GaAs surface with structural, compositional, and electronic properties similar to those of MBE-grown samples could be obtained by UHV vacuum annealing at relatively low temperature (400°C for 10 min) [Ter99a, Ter99b].
These lower temperatures in comparison to a cleaning based exclusively on heating, which then requires much higher temperatures, reduce thermal roughening effects and in particular surface destruction caused by non-congruent evaporation (setting on at about $620 - 660$°C [Rud03, Kar97, Kur95, Pie80]). The high solubility of the native oxides in hydrochloric acid assures their complete removal after about 10 seconds even in the diluted case. Nevertheless, longer etching periods are favorable since a partial release of gallium atoms in the form of chloric compounds to the etching leaves behind an excess layer of elemental As°, insoluble in acid solution (for pH below ≈ 3). The As°-overlayer is removed during the vacuum annealing but serves as an effective protection against contaminants on the surface. Hydrocarbon contaminations, adsorbed in the course of sample transfer to the vacuum system, were demonstrated to desorb entirely together with As° at the 400°C-annealing, even though hydrocarbons bonded directly to the surface require temperatures above 600°C [Ter02].
Our procedure corresponds to the diluted HCl wet-chemical etching mentioned above. Cathodes

are pre-cleaned by boiling in toluene and isopropanol, for five minutes in each case, and were immersed in pure isopropanol for transport to the glove box. Under the nitrogen atmosphere of the glove box, the etching in 1:60-solution of concentrated HCl in isopropanol for two minutes is performed. Two subsequent rinsings in fresh isopropanol and a drying by nitrogen flow accomplish the etching procedure. All chemicals used comply with the high purity standards of the LSI-semiconductor technology. The samples are placed on the target ladder of the transfer vessel laterally flanged to the glove box. Under slight overpressure of nitrogen, the vessel is closed hermetically and then transported to the load lock of the loading/hydrogen chamber (see Fig.3.3). After mounting and pumping down the chamber to $\approx 10^{-3}$ mbar, the vessel can be opened. Further pumping to a pressure in the lower 10^{-8} mbar range enables us to pass the samples to the preparation chamber without disadvantageous, longer lasting effects on the vacuum there. Cathodes are heated in the preparation chamber by thermal irradiation from the oven filaments. The pressure rises to not more than the 10^{-9} mbar range (at a base pressure $\leq 10^{-12}$mbar) during the annealing procedure. Prior to the nominal annealing temperature of 420°C, kept for 40 min, the temperature is slowly increased by ≈ 10°C/min to avoid thermal stress. Finally, a temperature jump to ≈ 560°C prepares a Ga-stabilized reconstruction which is required to get high quantum efficiency. In order to control the temperature, the photoluminescence spectroscopic method presented in section 3.4.3 was extended beyond the previous high temperature limit of this method reported in literature (400°C [Hal95]) to ≈ 620°C and used to calibrate the oven current with respect to the cathode temperature [Wei00]. Before proceeding with the activation, cathodes are kept in a position far from the ovens for about 2 hours to cool down to room temperature.

3.3.2 Hydrogen cleaning

The wet-chemical cleaning procedure of samples after several activations is a time-consuming process which requires to open (parts of) the vacuum system to atmosphere. This interferes especially with our goal of a quasi-continuous operation. In addition, etching does not necessarily provide a carbon-free surface (small carbon contributions are present in the residual gas even of our preparation chamber) whose presence could lead to a harmful interfacial barrier formation between GaAs and the activation layer [Ela98]. Concerning the morphology, wet-chemical cleaning is capable of recovering an initially flat surface but it did not show smoothing of initially rougher surfaces.

An alternative **in vacuum** cleaning technique enables us to operate the electron gun with a set of photocathodes, permanently kept under vacuum, on a long time scale compatible with beamtime requirements at the TSR. An increase of the annealing temperature alone leads to

the above mentioned enhanced roughening and damaging risks. Additionally, not all possible contaminations and the adsorbed cesium leavings of the previously deposited activation layer are removed.

A cleaning procedure basing on an **atomic hydrogen** (H•)-exposure reported by Petit *et al.* showed effective removal of As-oxides and a decrease of carbon contaminations already under room temperature conditions [Pet92]. This cleaning effect was found to work at moderate sample heating (300°C) even for Ga-oxide. Other authors observed a complete removal of carbon at 200°C [Sug91] and of all native oxides on GaAs at 400°C under (H•)-exposure [Ide94, Yam94, Rou93, Sug91]. The flux of H• in the different studies is hard to compare since the pressures (or exposures) are usually given for molecular hydrogen which was cracked at hot tungsten filaments and the real flux of H• could strongly depend on cracking efficiency and geometry. Nevertheless, complete contamination removal was obtained even for the studies with lower fluxes working at sample temperatures of 400°C.
The *chemical* reaction suggested by Ide *et al.* to release non-volatile Ga_2O_3 with (H•)-exposure:

$$Ga_2O_3 + 4H\bullet \rightarrow Ga_2O \uparrow + 2H_2O \uparrow$$

requires only the temperatures for a desorption onset of Ga_2O suboxides amounting to ≈ 350°C-400°C. *Thermal removal* of Ga_2O_3 would also involves the constitution of the suboxide Ga_2O by a reaction of Ga_2O_3 with substrate Ga atoms, and sets in only above 600°C [Ter02], too high considering the risk of surface roughening. Roughening of heat-cleaned samples could be explained by the extraction of the Ga-atoms from the substrate at the formation of volatile gallium suboxide. This involves a partial "etching" of gallium which preferentially proceeds in voids and creates, therefore, small pits [Yam95].
Yamada *et al.* investigated the native oxide removal by direct observation of species released during deoxidation. They proposed a two stage process with an arsenic liberation prior to the above mentioned gallium oxide removal according to:

$$As_2O_x + 2xH\bullet \rightarrow xH_2O \uparrow + As_2\left(\frac{1}{2}As_4\right) \uparrow$$

where $x = 1$, 3 or 5 stands for the oxides of arsenic.
Atomic hydrogen cleaning results moreover in a smooth arsenic-stabilized surface [San94]. The morphology of GaAs(100) surfaces subjected to atomic hydrogen exhibited a roughness on a mono-atomic level [Got95] and epilayers grown on hydrogen cleaned GaAs substrates showed an atomically flat terrace-like surface structure [Ada00]. Such (H•)-cleaned surfaces are demonstrated to provide a morphology on the same quality level as cautious wet-chemical etching. The (H•)-treatment can even be expected to enhance the smoothness of initially rough surfaces [Ela98]. Performance parameters as good as for conventionally cleaned photocathodes

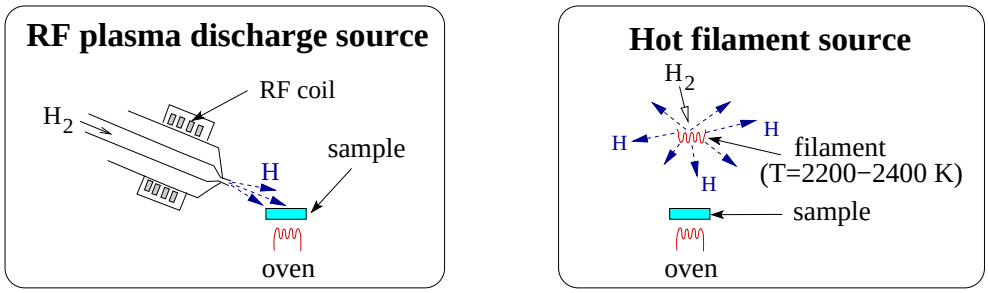

Fig. 3.5: *Principle of an RF plasma discharge and a hot filament atomic hydrogen source.*

were already received with (H•)-cleaning of GaAs(Cs,O)-cathodes [Ela98]. The optimal surface cleaning scheme for GaAs(100) is still controversial and some authors received excellent results with strongly different treatments. Meanwhile Petit *et al.* obtained the best results for a two step (H•)-cleaning at a sample temperature of 300°C with slightly varying doses [Pet97], Yamaguchi *et al.* suggest two steps with constant (H•)-dose but at 400°C in a first "cleaning" step, followed by a "smoothing"-step at higher temperature [Yam97]. Detailed investigations of the influence of different (H•)-cleaning schemes on the electron energy distribution of so prepared GaAs-photocathodes have to our knowledge not yet been reported. On this basis, in order to realize a reliable and efficient **in vacuum** cleaning technique for our photocathode preparation, we decided to implement an atomic hydrogen system in our set-up.

Common *sources of atomic hydrogen*, are based on plasma discharges, and on hot fil-

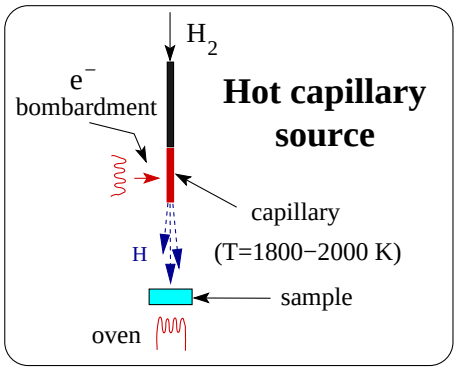

Fig. 3.6: *Principle of an atomic hydrogen source based on a hot capillary.*

ament or capillary cracking. The working principle for a RF plasma discharge source and a hot filament source are illustrated in Fig.3.5. Basic advantages of a plasma source are its high efficiency and a well directed (H•)-flux with a relatively low vacuum deterioration. On the other hand, there is a risk of higher energetic particles hitting the sample. The hot filament source

produces lower energetic particles and can be easily realized. However, low efficiency owing to the undirected (H•)-flow and the high tungsten filament temperatures causing harmfully high partial pressures of tungsten in the order of 10^{-8} mbar are critical points for this source type. In addition, the tungsten filament could heat the sample in an uncontrolled way.

A new type of source, developed in the last ten years, basically consists of a tungsten cap-

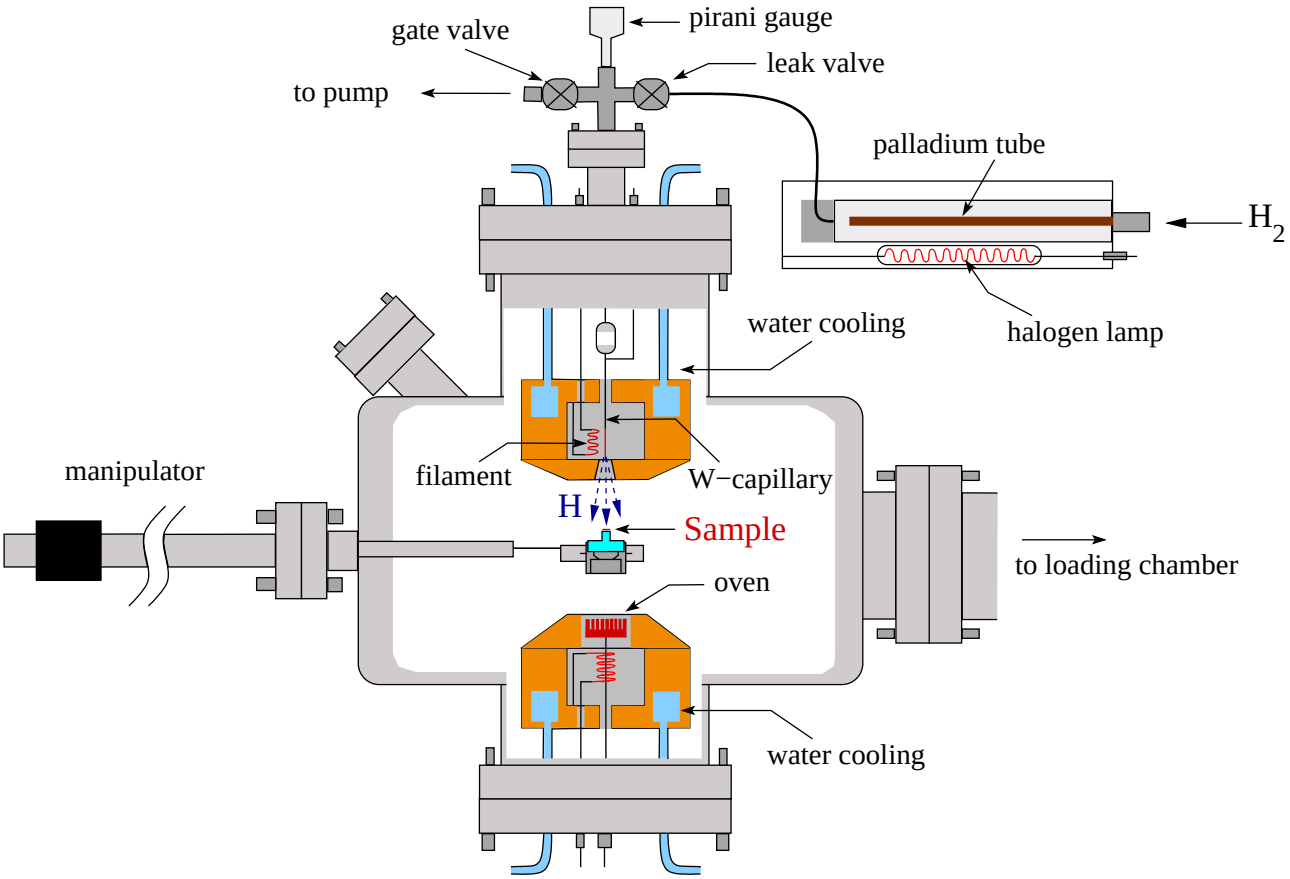

Fig. 3.7: *The atomic hydrogen chamber. Molecular hydrogen is cleaned by diffusion through a heated palladium filter. Then,* H_2 *is let in to the W-capillary by a leak valve and dissociates at about 1900 K. The directed atomic hydrogen flow is finally applied to the GaAs samples.*

illary traversed by molecular hydrogen and heated at the outlet by electron bombardment to 1800-2000 K (see Fig.3.6). This eliminates the disadvantages of a simple W-filament, connected with tungsten evaporation. The source proposed by Bischler and Bertel achieves nearly total H_2-dissociation under the relevant working pressures of $\approx 10^{-8}$ mbar [Bis93]. Effusion profiles from capillaries of similar dimensions exhibit a forward directed (H•)-output of almost beam-like shape [Eib98, Tsc98].

Our Bischler-type source features a W-capillary of 50 mm length with an inner diameter of

ϕ 0.6 mm, see Fig.3.7. Electron bombardment heats the last 5 mm before the end of the capillary. A water cooled copper screening with an aperture (ϕ 2 mm, aperture angle = 30°) prevents the surrounding from being heated. Samples are taken on holders at the manipulator head in the loading chamber and transferred to the hydrogen chamber. They can be positioned directly under the aperture at a distance of about 30 mm from the capillary outlet. An oven heats the sample radiatively from below.
Molecular hydrogen is filtered by a palladium tube and let in to the volume behind the capillary through a leak valve. The Pa-tube is heated to a temperature of typically 400°C, where H_2 effectively diffuses through the thin tube walls but possible contaminations are blocked. The inlet pressure of H_2 is monitored by a pirani gauge and this volume has a separate pump connection for bakeout reasons. Implementation and first tests of the atomic hydrogen cleaning will be presented in section 4.6.

3.3.3 Surface activation

Starting with a carefully cleaned GaAs(100) surface, the activation by oxygen and cesium deposition is performed. Similar to the alternating deposition of both species called "Yo-Yo"-technique commonly used since the early development of NEA-devices [Bel73], we keep the Cs-flow constant and add oxygen exposure for short periods. The cesium and oxygen dispensers allow a precise and very pure temperature-controlled release of the species on basis of cesium-chromate and oxygen-peroxide. In order to avoid desorption of contaminants during the operation, the dispensers are heat-cleaned prior to each activation run. The evolution of the photocurrent is supervised for a cathode negatively biased with about 30 V. A negative voltage applied to the carousel in this order proved to be sufficient to extract all electrons at our laser intensity (P $\approx$ 1 μm, $\lambda =$ 670 nm). The laser is modulated ($\nu \approx 29$ Hz) and applied in reflection mode. Red light is particularly suited since its visibility permits an easy focus adjustment on the cathode and the photoresponse sets in even before the activation reaches the state of negative electron affinity (at small positive electron affinity) in comparison to IR-light. Lock-in detection of the current flowing from the carousel to ground potential furnishes the relative evolution and a precise dc-calibration finally the absolute quantum efficiency (QE), see Fig.3.8. The quantum efficiency is displayed together with the pressure evolution. A "Yo-Yo"-like electron emission shape corresponds to alternating peaks emerging under sole cesium deposition (1^{st} Cs-peak), then under combined cesium- *and* oxygen-deposition (so-called 1^{st} oxygen-peak), again under sole cesium deposition (2^{nd} Cs-peak) and so forth. Time recording starts simultaneously with the cesium exposure.
The first Cs-peak occurs at about 21 min, indicating a typical time for a "reactivated" cathode,

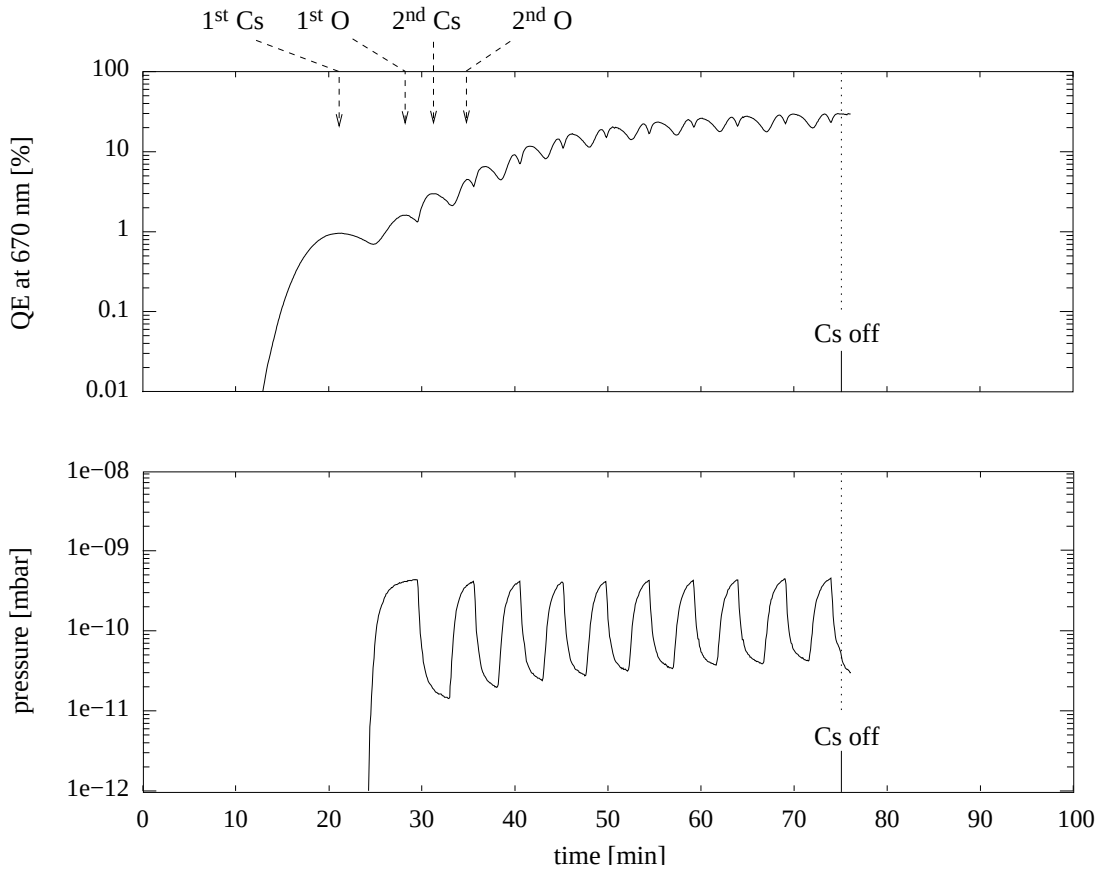

Fig. 3.8: *Full activation to maximum quantum efficiency and the respective pressure evolution in the preparation chamber. Time scale is referred to the start of the cesiation and the cesiation stopped at 75* min. *The final quantum efficiency amounts to 27%.*

viz a second activation at our cesium flux and geometry. Some sites on the GaAs(100)-surface are still occupied with stronger bound cesium atoms after a standard heat-cleaning procedure. They originate from the *first activation* performed previously with an etched or (H·)- cleaned surface and their incomplete removal at the heating. The presence of Cs on the surface is assumed to enable a favorable reconstruction during the heat-cleaning, since the quantum efficiency in the 2nd activation is usually higher than in the 1st activation, which was reproducibly found also in other studies [Rod86, Pas97]. Therefore, a 2-step activation is used and residual cesium on the surface becomes manifest in a reduced Cs-deposition time to reach the 1st Cs-peak. This particular time indicates, in consequence, the completeness of the Cs-removal prior to the activation.

After the first local maximum, further cesiation decreases the photocurrent. Slightly before reaching about 80% of the peak value, oxygen is switched on. The response of the electron current to the oxygen exposure is a little delayed in this early stage of activation, so that the

signal goes through a minimum several ten seconds after the oxygen was switched on. Later on, this response time reduces to a few seconds. Then, a first "oxygen" peak emerges and the oxygen is switched off again slightly before the next minimum to provide a dip at about 85% of the respective peak value. This procedure increases $|\chi_{\text{eff}}|$ and is repeated for "full activations" up to maximum quantum efficiency. The relative gain in QE for each pair of cesium and oxygen peaks decreases and finally saturates at typically ten repetitions. The activation is finished by a cesium peak, since a final Cs-deposition shows better stability of the photocathode with respect to residual gas contamination by oxygen species.
In case of carefully cleaned dispenser surroundings, the pressure shows no observable increase with beginning Cs-release. The clear pattern demonstrates the partial pressure originating from the oxygen exposure. After the dispensers were switched off at 75 min, the pressure reached its initial value before the activation of below $1 \cdot 10^{-12}$ mbar within 25-30 min.
A total oxygen exposure of 0.32 L (Langmuir, unit for exposure := 10^{-6} Torr·s) was applied in this particular case. Oxygen-exposures range between 0.2-0.35 L for full activations.
For good cathodes, the total quantum efficiencies reach 20-27% at 670 nm in reflection mode. Further activations following the standard heat-cleaning at 400°C, come to similar QE for two to three times. The QE reached in subsequent activations decrease gradually.
The (Cs,O)-layer thickness can not be measured directly in our set-up. However, considering the linear increase of the thickness with the time of Cs-exposure observed in other studies, the Cs-peak corresponds to approximately 0.5 monolayers of Cs-coverage [Kam91].

3.4 Cathode operation aspects

The operation at the electron target imposes high demands on the photocathode with respect to its performance parameters and in particular to its durability. A common stability parameter for NEA-GaAs cathodes is the time after which the initial photocurrent drops to e^{-1}, referred to as the "lifetime of the photocathode". Effects limiting the lifetime are discussed in the following section.

Spatial and temporal variations of the exciting laser beam profile have a direct impact on the emitted electron beam. The short response times of photocathodes ($\approx$ 100 ps [Dun95]) pick up even high frequency laser fluctuations. A reasonable choice for the light source (see section 3.4.2) is necessary for the application in the electron target to avoid beam heating originating from the excitation laser.

3.4.1 Photocathode lifetime

Lifetimes measured at very low light intensities (so-called "dark" lifetimes) evidence with values of several hundred hours under favorable vacuum conditions very good stability [Pas96, Pas97]. Limiting factors found in this operation regime are residual gas components particularly H_2O and CO_2, meanwhile CO, which is known as a harmful species for various photocathodes and makes the strongest contribution in our chamber besides H_2, has little effect on the stability of NEA-GaAs cathodes [Wad90]. A possible further limiting mechanism could be a slow, partial reconstruction of the activation layer. However, this should have a noticeable impact only for a certain disordered (Cs,O)-layer after the activation. Such "not properly" activated cathodes will feature also otherwise a reduced performance and can be easily reactivated.
The lifetimes at higher illumination and drawn electron current, respectively, are substantially lower than the dark lifetimes. Obviously, other mechanisms promote a stronger degradation in this case. Since a great part of the excess energy of the excited electrons is converted by surface recombination into phonons, photocathode heating was observed. Cs-desorption starts already at about 70°C and thus a strong illumination can lead to the partial evaporation of the activation layer. However, this heating problem was solved for the new electron gun (see chapter 5). In addition, the surface recombination can possibly induce chemical reactions of the activation layer.
In another degradation channel, the drawn photoelectron current gives rise to electron stimulated desorption in the vacuum chamber in particular at higher energies and to ionization of residual gas particles. This deteriorates the vacuum itself and leads additionally to a very harmful ion backflow. Ions can, depending on the electron optics, be guided and accelerated towards the cathode and hit the surface with high kinetic energy. In order to estimate degradation under vacuum conditions similar to those in the electron target (envisaged pressure there, lower 10^{-11} mbar range), lifetimes were measured in our gun chamber at $2 \cdot 10^{-11}$ mbar for initial electron currents of 1 μA and 1 mA, respectively (see Fig.3.9). They were presented in [Hop01]) and are reproduced here for completeness.
The analyzer, placed in-line with the electron gun at the photocathode test-bench, (see Fig.3.3) was cleaned prior to the measurements by electron bombardment. In case of an initial current of 1 μA, the extraction and acceleration voltage, respectively was set to 100 V and a fitted lifetime of (41.5 ± 0.5) hours was obtained. For an initial photoelectron current of 1 mA an acceleration voltage of 270 V was applied and lifetime amounted still to (10.2 ± 0.5) hours. The proven photocurrent decrease of less than 20 % within $\approx$ 2 hours is already acceptable for the operation at the electron target. The two fitted values demonstrate clearly the decisive influence of current induced degradation mechanisms on the lifetime.

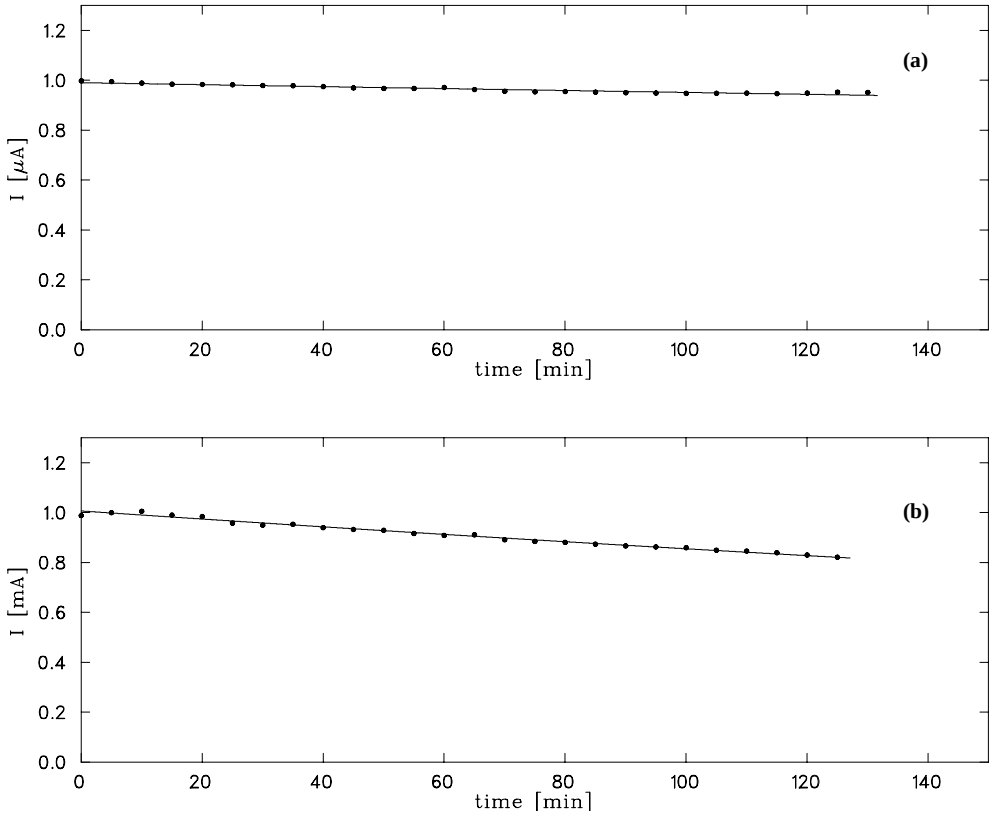

Fig. 3.9: *Photocathode lifetimes measured at cryogenic sample temperatures,* $p = 2 \cdot 10^{-11}$ mbar. *Fitting exponential curves results in* (e^{-1})*-lifetimes of (41.5 ± 0.5) hours in (a), the low-current regime (initial current 1* μA*) and (10.2 ± 0.5) hours in (b), high-current regime (initial current 1* mA*)[Hop01]).*

3.4.2 Illumination

A homogeneous illumination of the photocathode enables an almost constant emission profile of the GaAs(Cs,O)-surface. On the other hand, electrons emitted inhomogeneously according to a slightly inhomogeneous density profile of the laser experience a certain spatial *homogenization* if the space-charge limited emission is used. Since not all electrons are extracted fast enough from the region near the surface, a space charge cloud emerges in front of the cathode. This cloud represents a potential barrier for the following electrons. Locally enhanced electron emission results in a likewise locally increased space charge and thus a further blocking of potentially emitted electrons.

Applying small voltages to the Pierce electrode opens up additional possibilities to shape the electron beam in the required way [Spr03]. Laser density plots shown in Fig.3.10 exhibit a drop between the peak density and the edges of the actively used cathode area (limited by the pierce shield to ϕ 3 mm) of about 50%. The fiber-coupled diode laser with a peak wavelength

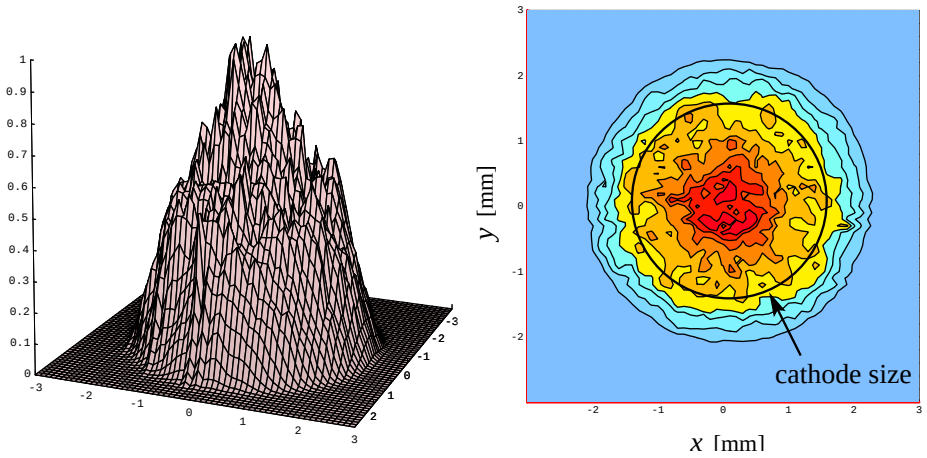

Fig. 3.10: *Laser density profile and contour plot at illumination with 0.75* W*. The electron emitting cathode size, depicted in the contour plot, is limited by the aperture of the Pierce electrode (see chapter 5).*

of 795 nm supplies up to 2.4 W cw-output power at the fiber end (core ϕ 200 μm).

Anomalous broadening was observed for longitudinal energy distributions of GaAs-photocathodes in cases that *multi-mode* lasers were applied [Gui96]. This multi-mode spreading was attributed to fast intensity fluctuations of the laser, known as mode beating. The fast photocathode response impressed the laser fluctuations on the electron beam, leading to energy relaxation and the observed broadenings. A possible, but in the high power range very costly, option to avoid this effect is the use of single mode lasers. Another approach is to employ a laser type where a variety of modes averages the intensity. We followed the second idea with our diode laser.

3.4.3 Temperature measurement

A well known *temperature dependency of the electronic properties* of GaAs arises from the influence of lattice vibrations on the energetic states of bulk electrons. One of the most important electronic characteristics of a semiconductor, the **band gap energy** E_{gap} features an increase in consequence of a decreasing temperature. This general behavior applies to intrinsic as well as doped samples for a large temperature range [Ole80] and is described by the Varshni equation [Var67]

$$E_{\mathrm{gap}}(T) = E_{\mathrm{gap}}(0) - \frac{\alpha \cdot T^2}{\beta + T}, \tag{3.1}$$

with the empirical parameters α, β and $E_{\mathrm{gap}}(0)$. Thus, measurements of E_{gap} allow to control the sample temperature, that is important in different applications. The photoluminescence technique was actively used for this purpose. Some of the electrons, which are photoexcited from the valence band to the conduction band and subsequently thermalized at the bottom of the conduction band, recombine radiatively with holes by emission of photons with $\mathrm{h}\nu \approx E_{\mathrm{gap}}$. Hence, photoluminescence spectra give direct data on the value of E_{gap}. However, for strongly doped samples (i.e. our case), E_{gap} is not well defined due to electron states within the band gap. The density of these states has a maximum close to the bottom of the conduction band and close to the top of the valence band. Moreover, tails of these states are distributed in the band gap with a density decreasing exponentially (with respect to the middle of the band gap). The exponential factor is a weak function of the temperature but depends strongly on the doping level. Practically, to employ the dependence according to eqn. (3.1) for strongly doped samples in temperature measurements, the following procedure was applied. Calibration PL-spectra are taken at defined temperatures for the used sample. The shift of the spectra at different temperatures allows to obtain the change of the band gap energy and, as a result, to define the absolute temperature. At small temperature changes (and usually at low temperatures), the shift of the photoluminescence maximum was determined according to

$$\Delta E_{\mathrm{peak}}(T) = E_{\mathrm{peak}}(T) - E_{\mathrm{peak}}(T_{\mathrm{ref}}) = -\frac{\alpha \cdot T^2}{\beta + T} + c(T_{\mathrm{ref}}), \tag{3.2}$$

with $\Delta E_{\mathrm{peak}}(T)$ and $c(T_{\mathrm{ref}})$ denoting the shift of the peak positions and a constant depending on T_{ref}, respectively. When the used temperature range is large, the shape of the spectrum is strongly modified (especially at higher temperatures). To detect the change of E_{gap}, the shift of the low-energy wing (which is only a weak function of the temperature) is measured.
The photoluminescence technique was used in our measurements in the temperature range from 80 K to 900 K. For example, we measured heating effects under high density laser illumination of LN_2-cooled photocathodes (block diagram, see Fig.5.10). For excitation of photoluminescence light, a modulated red probe laser illuminated a spot on the GaAs sample at low intensity which proved to produce negligible local heating (f = 330 Hz, $P \leq 20$ mW, spot size $\approx \phi$ 0.8 mm). Photoluminescence light was collected at the same spot with a double lens system and focused on a monochromator. The signal, detected by a silicon-diode, was amplified and analyzed by frequency-sensitive lock-in technique. Figure 3.11 shows a series of spectra taken with a LN_2-cooled sample without laser heating (reference spectrum) and four spectra recorded under different laser heating. The presented spectra show with increased heating a shift of the whole spectrum towards lower energy. The high energy tail of the spectra is governed by the combined density of states in the conduction and valence band, described to first approximation by an exponential drop according to $e^{-(\mathrm{h}\nu - E_{\mathrm{gap}})/kT}$. The low energy side corresponds to light emitted

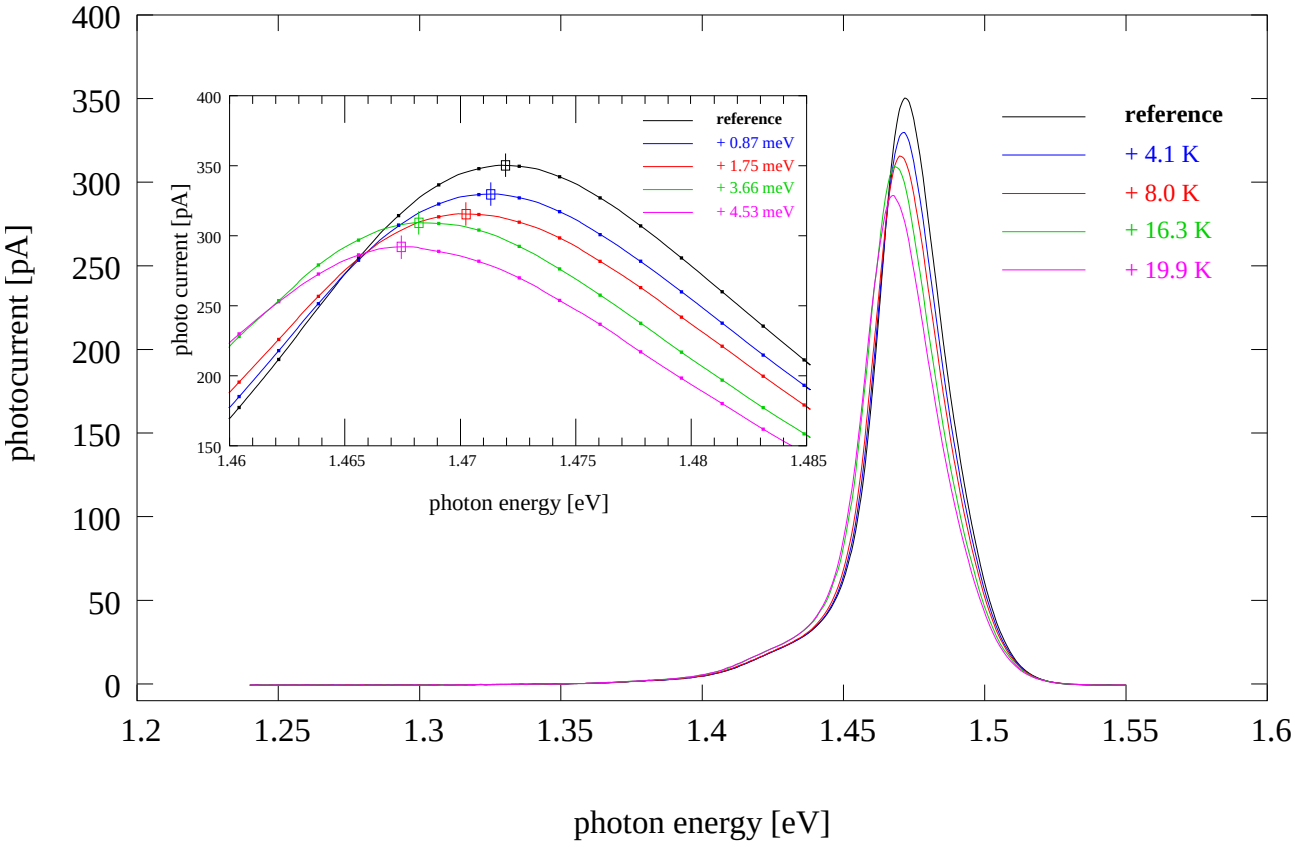

Fig. 3.11: *Photoluminescence spectra of* LN_2*-cooled samples used for temperature measurements of the GaAs bulk based on peak shifts. The series shows a reference spectrum without external heating and four spectra with applied laser heating (increments are non-equal). In the detailed view around the peak, each measured value (dotted) and the evaluated peak position (boxes) are plotted. Peak shifts from the reference position are given here in energy units. The resulting temperature shifts are indicated on the upper right side.*

at the recombination of electrons in states within the band gap. Absolute temperatures can be obtained with higher accuracy, if demanded, with an enhanced calibration for the individual sample. The Varshni parameters α, β for our samples were determined by calibration measurements, and T_{ref} amounts to (79 ± 2) K [Wei00]. Measuring ΔE_{peak} (see upper Fig.3.11) enables us to determine the absolute temperature within ± 2 K, limited by the accuracy of T_{ref}. The accuracy in the determination of *relative* temperatures is limited by the error in $\Delta E_{\mathrm{peak}}(T)$ of typically ± 0.17 meV for each curve. It corresponds to ± 0.8 K in the low temperature range and complies with the spreading among different measurements performed at the same temperature.

The method was applied with reduced accuracy even in the high temperature range up to (900 ± 15) K. In this range, the shift of straight lines fitted to the low energy tail was evalu-

ated and used in the temperature calibration of the preparation procedure (heat-cleaning) and of the hydrogen-cleaning (see section 4.6).
A possibility of *in-situ* temperature supervision opens up for cathodes activated to NEA. The state of negative electron affinity enables electrons excited to the valence band to escape to vacuum. In quantum yield spectroscopy (QYS), a steep onset of electron emission is thus observed when the photon energy exceeds E_{gap}. Analog to the calibration of the varshni parameters in case of photoluminescence, measurements at stable and well known temperatures have to be performed to determine the parameters in case of QYS. Work towards an implementation of this method is in progress.

4. Optimization of electron energy distribution and yields

The realization of a cold intense electron source based on NEA-GaAs poses problems which could be attributed to two main issues, investigated in the following chapters. The first issue combines aspects of providing high quantum efficiencies for cold electrons by optimization of the photoelectron energy distributions. Energy spreads below 10 meV will be regarded as cold in this sense. Investigations on energy distributions under different basic conditions (varying temperature and activation layer thickness) of the GaAs(Cs,O) cathode, performed in the energy analyzer set-up at low electron currents, will be presented and discussed in the present chapter. The second issue concerns the technological question of how to realize and operate a cold electron gun at high electron currents (a few mA) with these photocathodes and will be the subject of chapter 5.

The first section introduces the measurement procedures employed to analyze photoelectron energy distributions, followed in section 4.2 by a comparison of distributions at room and low temperature. In section 4.3, the production of of cold electron beams is discussed. Influences of the (Cs,O)-layer thickness are analyzed in section 4.4 and complete the presented studies on an optimized photocathode preparation. The results for the effective quantum yield of cold electrons are summarized subsequently in section 4.5. Finally, tests of the hydrogen cleaning technique with a continuously operated set of cathodes are described.

4.1 Measurement procedures

The methods used to get access to the energy distributions of photoelectrons are based on a retarding field technique. In a linear set-up (see Fig.4.2) with a constant longitudinal magnetic guiding field, the emitted electrons are accelerated, drift in the B-field over a distance of about 26 cm and are analyzed with respect to their longitudinal energy. This basic method will be described in the following section 4.1.1. By applying adiabatically changing magnetic fields in the drift region an amount of energy proportional to the initial transverse energy can

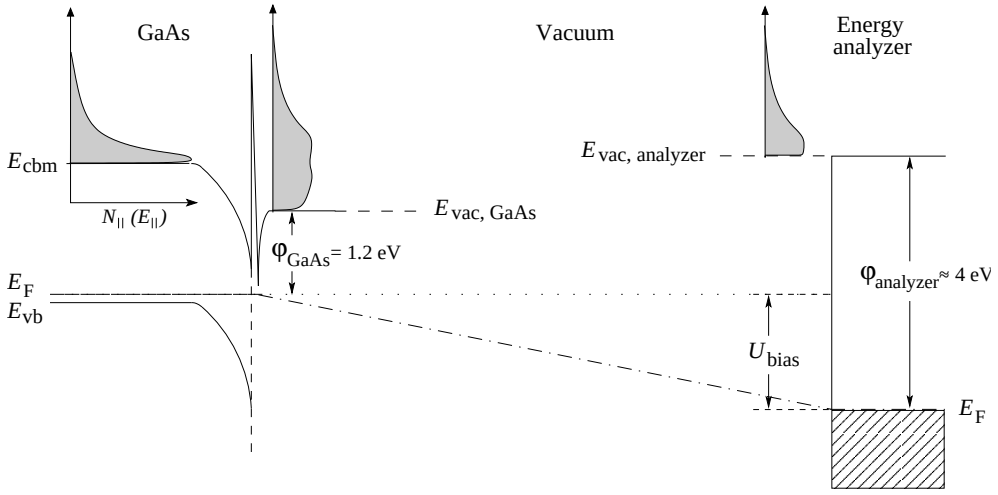

Fig. 4.1: *Band diagram of the photocathode and the analyzer region. By applying external voltage differences* $U_{\mathrm{bias}} := U_{\mathrm{acc}}$ - U_{ret}, $E_{\mathrm{vac,analyzer}}$ *traverses the longitudinal energy range of the photoelectron distribution.*

be transferred to the longitudinal degree of freedom. The controlled transfer opens up the possibility to measure mean transverse energies (MTE) for a part of the electron distribution [Pas00]. Finally, we succeeded in measuring the complete two-dimensional energy distribution $N(E_{\parallel}, E_{\perp})$ by marking electrons with a fixed longitudinal energy prior to the magnetic field change. Subsequent analysis of the energy transfer enabled us to reconstruct the complete emitted distribution [Orl01a]. These developments will be discussed in section 4.1.2.

4.1.1 Longitudinal energy distribution

The energy distribution of a rotationally symmetric, magnetized electron beam is given as a function of its longitudinal and transverse degree of freedom

$$N(E_{\parallel}, E_{\perp}). \tag{4.1}$$

It is considered to be normalized: $N(E_{\parallel}, E_{\perp}) = \int_0^{\infty} dE_{\parallel} dE_{\perp} \cdot N(E_{\parallel}, E_{\perp}) = 1$. The longitudinal distribution can be written as

$$N_{\parallel}(E_{\parallel}) = \int_0^{\infty} dE_{\perp} \cdot N(E_{\parallel}, E_{\perp}) \tag{4.2}$$

and is experimentally accessible via a retarding field method. A potential barrier of the energy height $e \cdot U_{\mathrm{ret}}$, with U_{ret} denoting the externally applied retarding voltage, is established and its transmission can be described by a step function $\theta(E_{\parallel} - E_{\parallel}^{\mathrm{ret}})$, with $E_{\parallel}^{\mathrm{ret}} = e \cdot (U_{\mathrm{ret}} - U_{\mathrm{acc}} + U_{\mathrm{offset}})$. U_{acc} denotes the externally applied acceleration voltage and $U_{\mathrm{bias}} := U_{\mathrm{acc}} - U_{\mathrm{ret}}$. A remaining

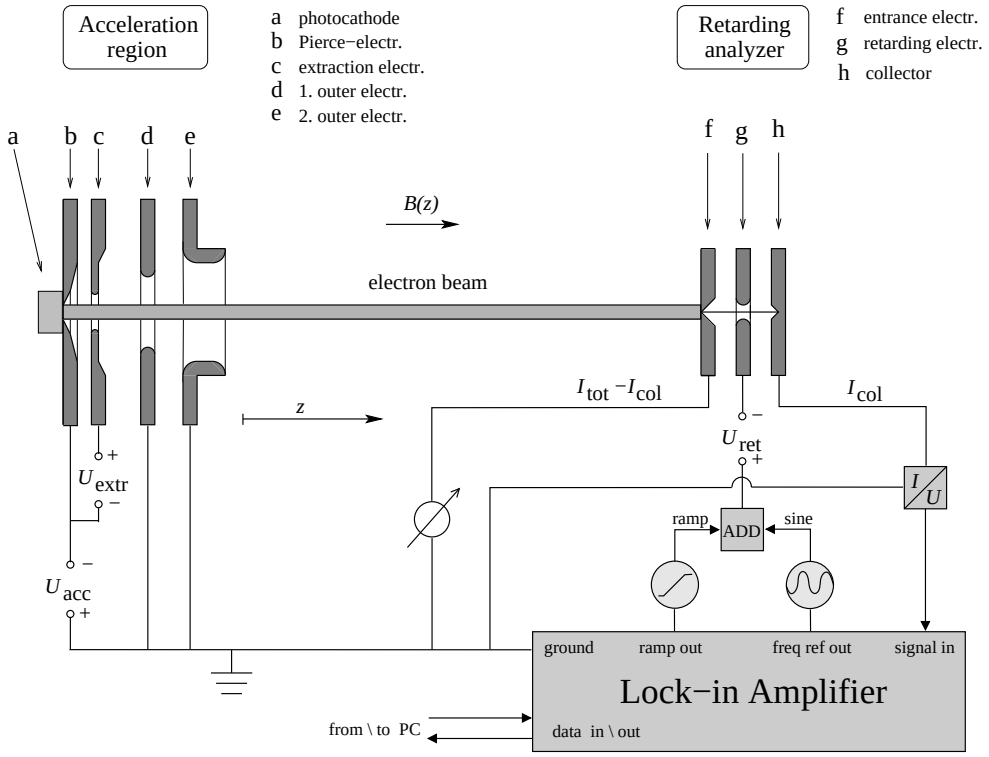

Fig. 4.2: *Sketch of the electronic arrangement used for the measurement of longitudinal EDCs. At the acceleration region the photocathode (a) is pressed to the Pierce electrode (b) and they are set to* U_{acc}*. A voltage applied to the electrode (c) serves to extract electrons. At the presented measurements, further electrodes (d & e) are grounded. On the analyzer side, an entrance diaphragm (f,* $\phi = 25$ μm*) cuts out a small fraction of the beam and the drained off current determines* $\approx I_{\mathrm{tot}}$*. The retarding voltage, a ramp and the sinusoidal modulation of the amplitude* ≈ 10 meV *are applied to the middle electrode (g). Finally the transmitted current of the collector (h) is measured. The movable analyzer can be adjusted in the transverse directions* $\pm$ *3* mm *with an accuracy of 1.25* μm *to measure the beam profile.*

effective voltage difference for $U_{\mathrm{bias}} = 0$ is denoted U_{offset}. This voltage offset is mainly caused by different work functions of the cathode and the analyzer, see Fig.4.1. Collecting electrons which are able to overcome the barrier will amount to the current $I_{\mathrm{col}}(U_{\mathrm{ret}})$:

$$I_{\mathrm{col}}(U_{\mathrm{ret}}) = I_{\mathrm{col,tot}} \cdot \int_0^\infty dE_\parallel \cdot \int_0^\infty dE_\perp \cdot \theta(E_\parallel - E_\parallel^{\mathrm{ret}}) \cdot N(E_\parallel, E_\perp). \tag{4.3}$$

The normalization factor $I_{\mathrm{col,tot}}$ is determined by the total collected current. Modulation of the retarding voltage U_{ret} with a small amplitude yields under frequency- and phase-sensitive detection of $I_{\mathrm{col}}(U_{\mathrm{ret}})$ (lock-in amplifier) the differentiated retarding curve and thus the longitudinal energy distribution curve (EDC):

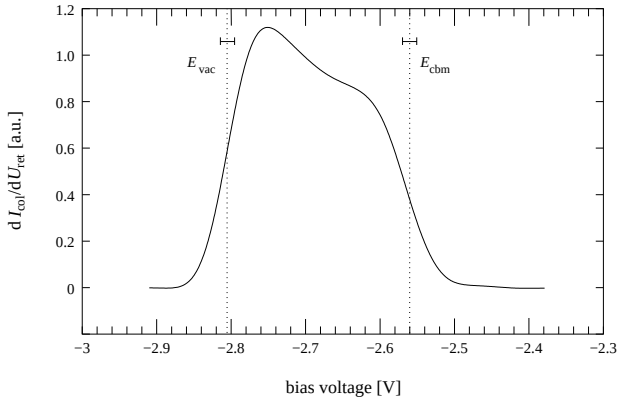

Fig. 4.3: *Longitudinal EDC, raw spectrum of the lock-in amplifier measured with a photocathode activated to maximum QE and then cooled down to 100* K *as a function of the applied bias voltage* $:= U_{\mathrm{acc}} - U_{\mathrm{ret}}$. *Vacuum level* E_{vac} *and conduction band minimum* E_{cbm} *are indicated by dotted lines. An error bar is added for* E_{cbm}. U_{acc} *amounts to -20* V.

$$\begin{aligned}\frac{dI_{\mathrm{col}}(U_{\mathrm{ret}})}{dU_{\mathrm{ret}}} &= -e \cdot I_{\mathrm{col,tot}} \cdot \int_0^\infty dE_\parallel \cdot \int_0^\infty dE_\perp \cdot \delta(E_\parallel - E_\parallel^{\mathrm{ret}}) \cdot N(E_\parallel, E_\perp) \\ &= -e \cdot I_{\mathrm{col,tot}} \cdot \int_0^\infty dE_\perp \cdot N(E_\parallel^{\mathrm{ret}}, E_\perp) = -e \cdot I_{\mathrm{col,tot}} \cdot N_\parallel(E_\parallel^{\mathrm{ret}}).\end{aligned} \tag{4.4}$$

Figure 4.2 shows the electrode arrangement in the energy analyzer set-up and the block diagram of the electronics. The applied procedure of an in-situ derivative measurement effectively suppresses noise and unwanted signals outside a narrow band around the reference frequency which enhances resolution compared to numerical differentiation. Furthermore, the response of the analyzer due to finite capacity with respect to the modulation can easily be filtered out since it is phase-shifted by about $\pi/2$ to the photoelectron current. A longitudinal EDC recorded with the lock-in method as a function of the applied bias voltage $:= U_{\mathrm{acc}} - U_{\mathrm{ret}}$ is shown in Fig.4.3. During the measurement, the electron density was kept low ($\lesssim 10^5 \mathrm{cm}^{-3}$) to avoid beam relaxation effects. The good quality of the raw data demonstrates the low noise level of the technique. An abscissa shift of about -2.8 V is caused by the differences between applied and effective voltages which will enter into U_{offset}. The vacuum level is conventionally assigned to the point of inflection at the low energy slope of the EDC [Ter94, Dro85] and could be determined with an accuracy better than ± 10 meV.

The linearity of the applied voltage and the *effective* voltage in the center of the retarding electrode was verified by measurements at different U_{acc} and the evaluation of $U_{\mathrm{ret}}^{\mathrm{f.m.}}$ corresponding to the first moments of the EDC. A one to one correspondence of the shifts of U_{acc} and $U_{\mathrm{ret}}^{\mathrm{f.m.}}$ was proved to be fulfilled very well (deviation $\ll 1$ meV) in the range of U_{acc} up to about -20 V. In order to assign the position of the conduction band minimum of GaAs to the energy scale, a

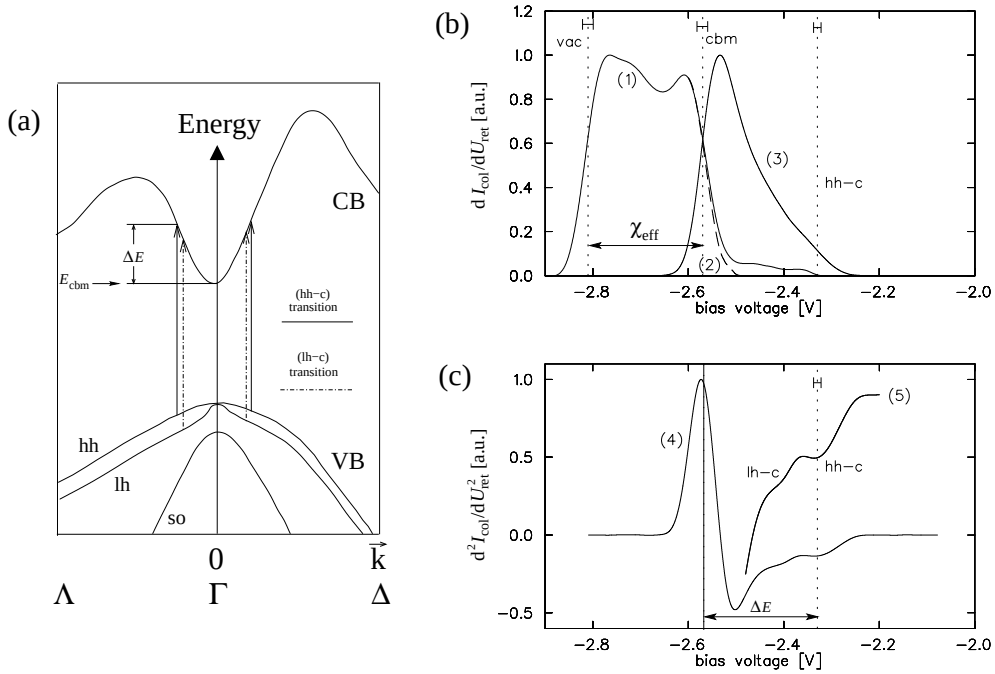

Fig. 4.4: *(a) Transitions of the electrons for a fixed photon energy from heavy-hole band to the conduction band (hh-c) and from the the light-hole band to the conduction band (lh-c). (lh-c)-transitions reach slightly lower states in the conduction band than (hh-c)-transitions. The length of the arrows corresponds to the photon energy (*hν *= 1.85* eV*). The known band structure fixes the energies of the upper energy level with respect to the* E_{cbm}*. To calculate* ΔE*, deviations from the parabolicity and isotropy of the electronic bands were taken into account.*
*(b) Example of a longitudinal EDC (1) taken with a red laser (*hν *= 1.85* eV*) at 100* K *[Hop01]. The dashed curve (2) was recorded with infrared illumination to demonstrate modifications of the high energy tail due to non-thermalized electrons. For an enhanced resolution, curve (3) was measured with an applied cutting barrier - blocking low energy electrons - and increased laser intensity to amplify the high energy tail.*
(c) Derivative of (3), plotted for the whole spectrum (4) and the upscaled high energy tail (5). The features of the (hh-c)- and (lh-c)-transitions differ for about 80 meV*. (The matching of the conduction band minimum and the maximum of the derivative is coincidental.)*

calibration procedure reported by [Dro85, Ter94] was applied. The emission energy of electrons excited from the heavy hole band to the conduction band (see Fig.4.4 (a)) serves as calibration point on the energy scale. Signatures of ballistic photoelectrons originating from the (hh-c) transitions can be resolved in the first derivative of the longitudinal EDC (Fig.4.4 (c)). With the known laser photon energy and electronic band structure data, the difference ΔE between E_{cbm} and the final energy of electrons being excited from the heavy-hole band was calculated. For our samples and laser (hν = 1.85 eV), ΔE amounted to (240±5) meV [Hop01]. Hence,

in the longitudinal EDC, E_{cbm} is located at an energy ΔE below the (hh-c) minimum. The accuracy of the calibration is $\pm$ 10 meV.

4.1.2 Complete energy distribution

In order to study the photoemission process from GaAs(Cs,O), a method to map out the complete energy distribution $N(E_\parallel, E_\perp)$ was applied. At this method, a class of electrons with fixed longitudinal energy is "marked" and subsequently transversely analyzed by an adiabatic magnetic compression technique. Along the drift path of the electrons from the acceleration region to the analyzer, the axial magnetic field $B(z)$ was varied. While the magnetic field at the cathode position B_0 was kept at 500 Gauss, the magnetic field $B_{\mathrm{a}} = \alpha \cdot B_0$ at the analyzer can be adjusted in the range of $\alpha = 1$ to $\alpha = 2.5$. As $E_\perp/B$ is an adiabatic invariant (eqn. 2.10) and the total energy is conserved (eqn. 2.9), the longitudinal and transverse energy of an electron are subjected to an energy transfer between the two degrees of freedom. The energies of an electron arriving at the analyzer $(E_\parallel{}', E_\perp{}')$ are related to those before the magnetic field change $(E_\parallel, E_\perp)$ by (cp. eqn. 2.12)

$$E_\parallel{}' = E_\parallel - \Delta\alpha E_\perp \tag{4.5}$$

$$E_\perp{}' = E_\perp + \Delta\alpha E_\perp, \tag{4.6}$$

with $\Delta\alpha = \alpha - 1$. Field changes with $\Delta\alpha > 0$ are called adiabatic magnetic compressions. Provided that the analysis is restricted to a class of electrons with fixed longitudinal energy $E_\parallel$, relation (4.5) allows to receive information about the initial transverse energy distribution by applying the conventional retarding field method to the longitudinal energy $E_\parallel{}' = f(E_\perp)$. The "marking" of the class proceeds with the help of a potential barrier directly after the emission of electrons from the cathode.

By a large positive extraction voltage U_{extr} applied to the first electrode (see Fig.4.1), all charges can be extracted from the region near the cathode (current limited emission). With a decreasing extraction voltage, low energy electrons start to get blocked according to the generated potential barrier. The transmission of the blocking potential barrier can be described by a step function. Taking into account the analyzer and blocking electrode transmission $\theta(E_\parallel{}' - E_\parallel^{\mathrm{ret}})$ and $\theta(E_\parallel - E_\parallel^{\mathrm{b}})$, respectively, as well as the transformation (4.5), eqn.(4.3) is modified to

$$I_{\mathrm{col}}(U_{\mathrm{ret}}) = I_{\mathrm{col,tot}} \cdot \int_0^\infty dE_\perp \cdot \int_0^\infty dE_\parallel{}' \; \theta(E_\parallel{}' - E_\parallel^{\mathrm{ret}}) \; \theta(E_\parallel{}' + \Delta\alpha E_\perp - E_\parallel^{\mathrm{b}}) \cdot N(E_\parallel{}' + \Delta\alpha E_\perp, E_\perp). \tag{4.7}$$

The derivative of $I_{\mathrm{col}}(U_{\mathrm{ret}})$ is given by

$$\frac{dI_{\mathrm{col}}(U_{\mathrm{ret}})}{dU_{\mathrm{ret}}} = -e \cdot I_{\mathrm{col,tot}} \cdot \int_0^\infty dE_\perp \cdot \; \theta(E_\parallel^{\mathrm{ret}} + \Delta\alpha E_\perp - E_\parallel^{\mathrm{b}}) \cdot N(E_\parallel^{\mathrm{ret}} + \Delta\alpha E_\perp, E_\perp), \tag{4.8}$$

equivalent to eqn.(4.4).

The control of the blocking energy $E_\parallel^{\mathrm{b}}$ before the adiabatic field change opens the possibility to "mark" a class of electrons with a fixed longitudinal energy (see Fig.4.5). A small modulation $\Delta E_\parallel^{\mathrm{b}}$ yields an ac-component of the analyzer current which represents only electrons with initial longitudinal energies $E_\parallel$ near $E_\parallel^{\mathrm{b}}$. This signal exists only where $\theta(E_\parallel - E_\parallel^{\mathrm{b}})$ changes. Recording only these "marked" electrons $I_{\mathrm{col}}^{\mathrm{mark}}(U_{\mathrm{ret}})$ and taking the derivative $dI_{\mathrm{col}}^{\mathrm{mark}}/dU_{\mathrm{ret}}$ directly measures a signal proportional to the transverse energy distribution for electrons with an initial $E_\parallel$ equal to $E_\parallel^{\mathrm{b}}$.

$$\frac{dI_{\mathrm{col}}^{\mathrm{mark}}(E_\parallel^{\mathrm{ret}})}{dE_\parallel^{\mathrm{ret}}} \propto \int_0^\infty dE_\perp \cdot \; \delta(E_\parallel^{\mathrm{ret}} + \Delta\alpha E_\perp - E_\parallel^{\mathrm{b}}) \cdot N(E_\parallel^{\mathrm{ret}} + \Delta\alpha E_\perp, E_\perp) \tag{4.9}$$

$$\propto N(E_\parallel^{\mathrm{b}}, \overbrace{(E_\parallel^{\mathrm{b}} - E_\parallel^{\mathrm{ret}})/\Delta\alpha}^{E_\perp}). \quad (\Delta\alpha \neq 0) \tag{4.10}$$

Hence, the integral in (4.9) has only contributions from $E_\perp = (E_\parallel^{\mathrm{b}} - E_\parallel^{\mathrm{ret}}) \;/\; \Delta\alpha$ at a longitudinal energy $E_\parallel = E_\parallel^{\mathrm{b}}$. If U_{ret} goes through all range, one receives the relative *differential* transverse energy distribution $N(E_\parallel^{\mathrm{b}}, E_\perp)$ for the longitudinal energy $E_\parallel^{\mathrm{b}}$. Normalization of the integral value to $N_\parallel(E_{\mathrm{b}})$ and scanning all longitudinal energies, yields the two-dimensional energy distribution [Orl01a].

Figure 4.5 illustrates a *differential* transverse energy distribution measurement in the potential band diagram. The longitudinal distributions in vacuum could be accessed by a measurement in a uniform magnetic field without a blocking potential barrier (b), with barrier (c), and with an adiabatic increasing field and barrier (d). Since longitudinal EDCs always integrate over all transverse energies, only the final longitudinal distribution (d), where exclusively electrons with the same longitudinal energy were analyzed, gives information about the transverse energy due to measured shifts for the final longitudinal energy. The block diagram of the electronic arrangement is presented in Fig.4.6. A first modulation on the extraction electrode (frequency f_{b}) marks electrons at $E_\parallel^{\mathrm{b}}$. The modulation at the retarding electrode (frequency f_{ret}) keeps up the conditions to measure directly the derivative of the signal. In order to receive a clean reference for the lock-in amplifier, a frequency mixer produces the reference frequency, i.e. the difference $\Delta f = f_{\mathrm{b}}$ - f_{ret}. Exclusive recording at this reference allows to obtain an ac-contribution related

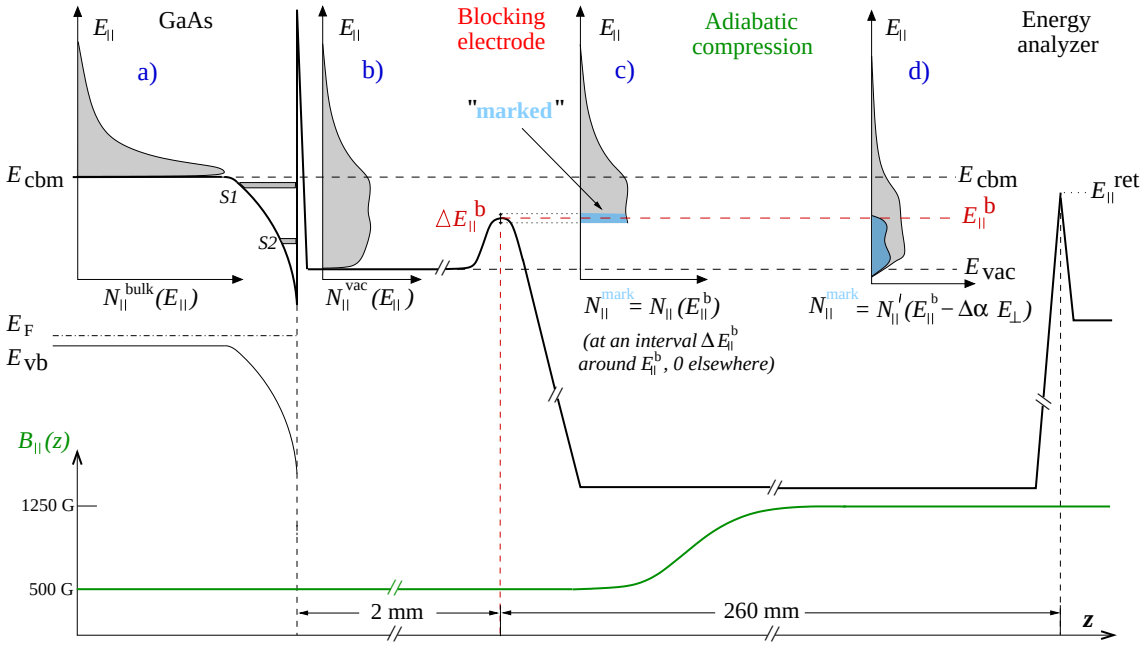

Fig. 4.5: *Sketch of the potential diagram of the* GaAs(Cs,O)*-vacuum-analyzer region to illustrate the measurement principle for the transverse energy distribution for a fixed initial* $E_{\parallel}^{\mathrm{b}}$.
A small modulation of the blocking potential $\Delta E_{\parallel}^{\mathrm{b}}$ *marks electrons with longitudinal energy* $E_{\parallel} = E_{\parallel}^{\mathrm{b}}$ *before an adiabatic change of the magnetic field. Shown are the initial bulk distribution (a) and the longitudinal electron distributions: (b) directly after the emission, (c) with applied blocking below* $E_{\parallel}^{\mathrm{b}}$ *and marking at* $E_{\parallel}^{\mathrm{b}}$ *before magnetic compression and (d) with blocking & marking after an adiabatic increasing field. In picture (c), an ideal marking for an exclusive recording of only the marked current would show the value* $N_{\parallel}(E_{\parallel}^{\mathrm{b}})$ *in an interval of width* $\Delta E_{\parallel}^{\mathrm{b}}$ *around* $E_{\parallel}^{\mathrm{b}}$ *and zero outside. After the adiabatic compression, all electrons will be shifted down by a value* $\Delta\alpha E_{\perp}$ *according to their initial transverse energy. Thus the whole distribution broadens and states below* $E_{\parallel}^{b}$ *are again populated. The analyzer signal in (d) for the marked electrons* $dI_{\mathrm{col}}^{\mathrm{mark}}/dU_{\mathrm{ret}}$ *at a certain* U_{ret} *is proportional to the broadened distribution* $N_{\parallel}{}'^{\mathrm{mark}}(E_{\parallel}^{\mathrm{ret}})$ *at* $E_{\parallel}^{\mathrm{ret}} = E_{\parallel}^{\mathrm{b}} - \Delta\alpha E_{\perp}$ *and the latter in turn equal to the value* $N(E_{\parallel}, E_{\perp})$ *of the initial distribution at* $E_{\parallel} = E_{\parallel}^{\mathrm{b}}$ *and* $(E_{\parallel}^{\mathrm{b}} - E_{\parallel}^{\mathrm{ret}})/\Delta\alpha$, *respectively. Magnetic field strength and dimensions are shown at the bottom.*

to both initial frequencies and thus to electrons characterized by both, the initial blocking energy and final retarding energy. Examples for the transverse EDC measurement procedure without and with the "marking" are plotted in Fig.4.7. The derivative signal of the collector current in a uniform magnetic field ($\alpha = 1.0$, black) is strongly broadened and shifted to lower longitudinal energies in an adiabatically increasing magnetic field ($\alpha = 2.5$, red, upper left side). The mean transverse energy arisen from the shift amounts to 62 meV. In order to compare the *differential* transverse EDCs at two different longitudinal energies, the corresponding marked signals are recorded and shown in the lower left diagram. At higher longitudinal energy

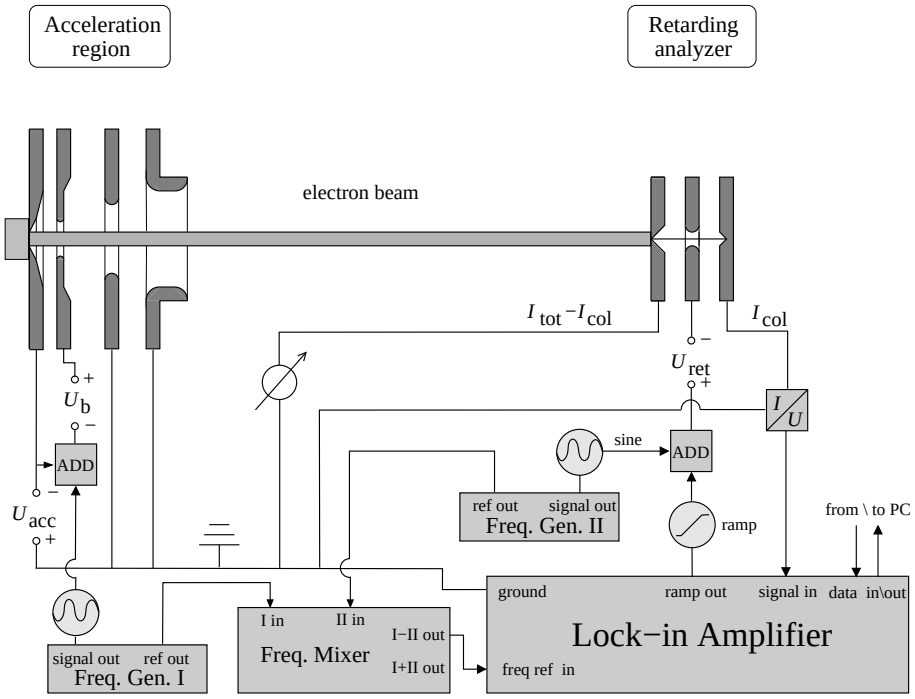

Fig. 4.6: *Electronic arrangement for a differential transverse energy measurement. Two function generators supply sinusoidal frequencies of a few hundred Hertz. The first one is added to the blocking potential U_b at the extraction electrode and the second one to the retarding electrode. Both frequencies are fed in a frequency mixer, which provides the difference (tens of* Hz*) as reference for the lock-in amplifier.*

(U_{bias1} = -2.54 V), the black curve is shifted only slightly to lower longitudinal energies under an increasing magnetic field. A *differential* mean transverse energy (dMTE) of 6 meV could be deduced from the shift, while the shape remains comparatively sharp. In case of low longitudinal energy (U_{bias2} = -2.77 V), a strong broadening and obvious shift indicates high transverse energy contributions resulting in dMTE = 98 meV.
With a step width for U_{bias} of 20 meV over the whole range, a series of *differential* EDCs was measured. After normalization of each integrated value to $N_{\parallel}(U_{\mathrm{bias}})$, a numerical interpolation yields a continuous two-dimensional energy distribution (right side of Fig.4.7).
Taking into account the finite resolution, the δ-function in eqn.(4.9) will be changed at a uniform magnetic field ($\Delta\alpha = 0$) to a sharply peaked function reflecting the combined width of the analyzer and the blocking electrode transmission function. The signal $dI_{\mathrm{col}}^{\mathrm{mark}}/dU_{\mathrm{ret}}$ at $\Delta\alpha = 0$ could be well fitted by a Gaussian distribution with the standard deviation of $\sigma_{\mathrm{LE}} = 17$ meV. This width is dominated by the analyzer and does not depend on the amplitude of the modulation for $E_{\parallel}^{\mathrm{b}} \lesssim 15$ meV. The transverse energy resolution is given by $\sigma_{\mathrm{TE}} = \sigma_{\mathrm{LE}}/\Delta\alpha$. Slight influ-

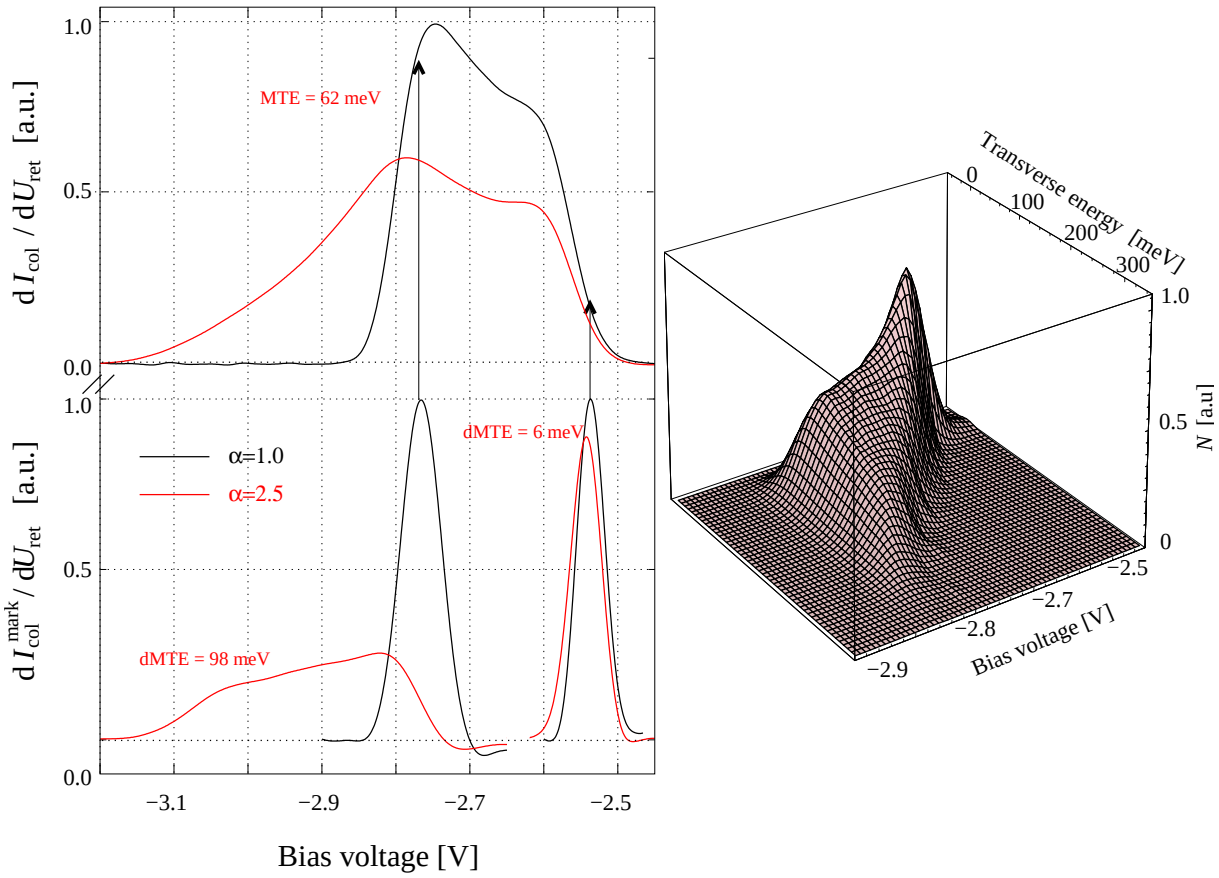

Fig. 4.7: *Left side: Derivative signal of the collector current for the total signal (top) before ($\alpha = 1$, black) and after adiabatic compression ($\alpha = 2.5$, red) as a function of the bias voltage. The lower plot shows the derivative signal of the marked current for two settings of $E_{\parallel}^{\mathrm{b}}$ before and after compression. The black curves are always normalized to unity and the red curves have integral values equal to those of the corresponding black distribution. At high $E_{\parallel}^{\mathrm{b}}$, the shape of the differential transverse energy distribution is very narrow and the shift due to the compression is only small. At low $E_{\parallel}^{\mathrm{b}}$, there is an evident broadening due to much higher transverse energies. Right side: Two-dimensional energy distribution interpolated from a series of differential transverse energy measurements.*

ences of the blocking potential modulation on the transmission of electrons above the marked range result in a contribution from these electrons to the ac-signal. The effect is strongest for low longitudinal energies where it contributes an integral fraction of ≈ 5 % to the signal.

4.2 Cryogenic operation

Before emission to the vacuum, the initial electron energy distribution in the conduction band of the bulk follows the Maxwellian law and longitudinal as well as transverse spreads are given by $\approx k_{\mathrm{B}}T_{\mathrm{bulk}}$. The temperature of the bulk can accordingly have a significant impact on electron distributions in the vacuum if electron energy and momentum are completely or partially conserved during the emission process.
In order to investigate these effects, a cathode activated to maximum total quantum efficiency ($QE_{\mathrm{tot}}^{670\mathrm{nm}} \approx 23$ % in reflexion mode), was cooled with LN_2 to ≈ 100 K and its two-dimensional photoelectron energy distribution $N(E_{\parallel}, E_{\perp})$ was compared to a room temperature spectrum (Fig.4.8, room and low temperature denoted by "rt" and "lt" below). The temperature was determined before by photoluminescence spectroscopy under comparable conditions [Wei00]. In the measurement, the applied laser power density was kept low to avoid beam relaxation effects at the resulting low electron densities ($\leq 10^5$ cm^{-3}). Integral collector currents amounted to 10 pA (rt) and increased to 12.6 pA (lt), representing $QE_{\mathrm{tot}} = 23$ % (rt) and $QE_{\mathrm{tot}} = 29$ % (lt), respectively. In order to permit an easy comparison, the spectra are scaled to have the same maximum value and the longitudinal energies are referred to E_{cbm} using the calibration described in section 4.1.1. It is evident from the figure, that the dominating peak structure ($E_{\parallel}^{\mathrm{peak}} \approx -9$ meV) became much more pronounced at low temperature. Whereas the high energy tail ($E_{\parallel} > 0$) shows a steep, in both cases exponential, drop-off with $\approx k_{\mathrm{B}}T_{\mathrm{bulk}}$, the signal evolves below E_{cbm} for low temperature after a stronger decrease into a plateau at ≈ 40 % of the maximum. Mainly due to a larger band gap for the cooled sample ($\Delta E_{\mathrm{gap}} \approx 80$ meV), $|\chi_{\mathrm{eff}}|$ increased from 160 meV (rt) to 240 meV (lt) which results in an expanded phase space. The presence of electron contributions at states below the initial energy in the bulk ($E_{\parallel} \geq 0$) which occupy all available phase space down to the cut-off at E_{vac} clearly demonstrates the influence of elastic and inelastic scattering processes at the GaAs(Cs,O)-vacuum interface.
In comparison to thermocathodes, where the high energy tail of the Maxwell-Boltzmann distribution spreads with about 110 meV ($T_{\mathrm{cathode}} = 1300$ K) and lower temperatures reduce these spreads, photocathodes exhibit opposite behavior. The total amount of strongly scattered electrons contributes so much that the overall mean transverse energy (MTE) rises from 59 meV (rt) to 66 meV (lt). In the contour plots (Fig.4.9), it is easy to comprehend the effect of scattering during the emission as energy shift in longitudinal and transverse direction. Bulk electrons start with positive $E_{\parallel}$ and longitudinal and transverse spreads of $\approx k_{\mathrm{B}}T_{\mathrm{bulk}}$. Inelastic scattering processes with conserved longitudinal momentum during the emission will cause vertical down shifts in the plot. On the straight line for $E_{\perp} = 0$, delimiting the left side of the nearly triangular distribution shape, electrons are found which accordingly underwent inelastic scattering but

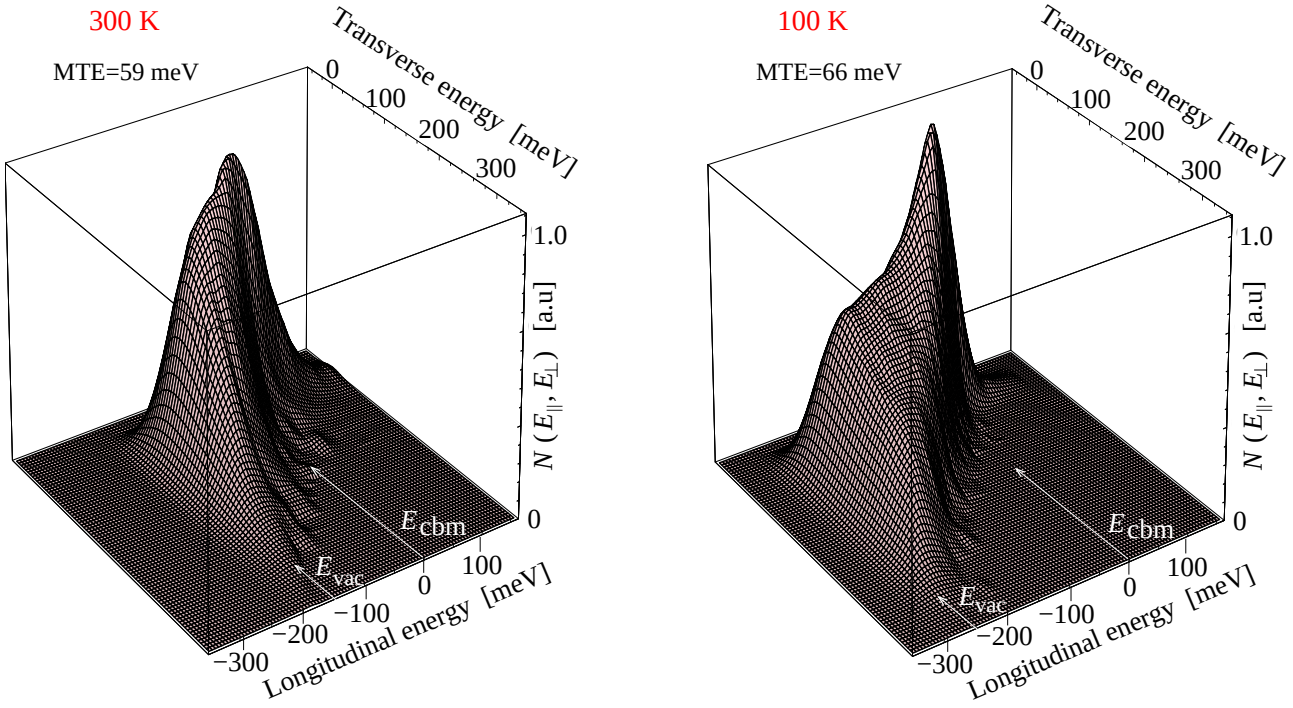

Fig. 4.8: *Two-dimensional photoelectron energy distributions at room and low temperature, scaled to have the same maximum value. The longitudinal energy scale is referred to* E_{cbm}*. Vacuum levels* E_{vac} *and conduction band minima* E_{cbm} *are indicated with white arrows.*

kept their initial, vanishingly low transverse energy. Small signals at negative $E_\perp$ result from broadening by the analyzer. Purely elastic scattering processes will shift electrons diagonally during the emission on straight lines parallel to $E_{\mathrm{tot}} = 0$. Thus the right side is delimited by electrons with the highest initial energy before emission having suffered purely elastic scattering. In between these two limits, all kinds of combined scattering processes cause a filling of the available phase space down to E_{vac}. Although a change in the shape at the transition E_{cbm} is not clearly resolved at room temperature, the high energy edge evolves for low temperature to a real nose-like shape. This sub-ensemble with $E_{\mathrm{cbm}} \geq 0$ represents transversely thermalized electrons which will constitute the effective quantum efficiency after an appropriate cutting of the scattered electrons.

4.3 Production of cold electron beams

In order to produce cold electron beams, the photoelectron distribution has to be restricted to a part of the distribution which exhibits a low energy spread. Applying a potential barrier

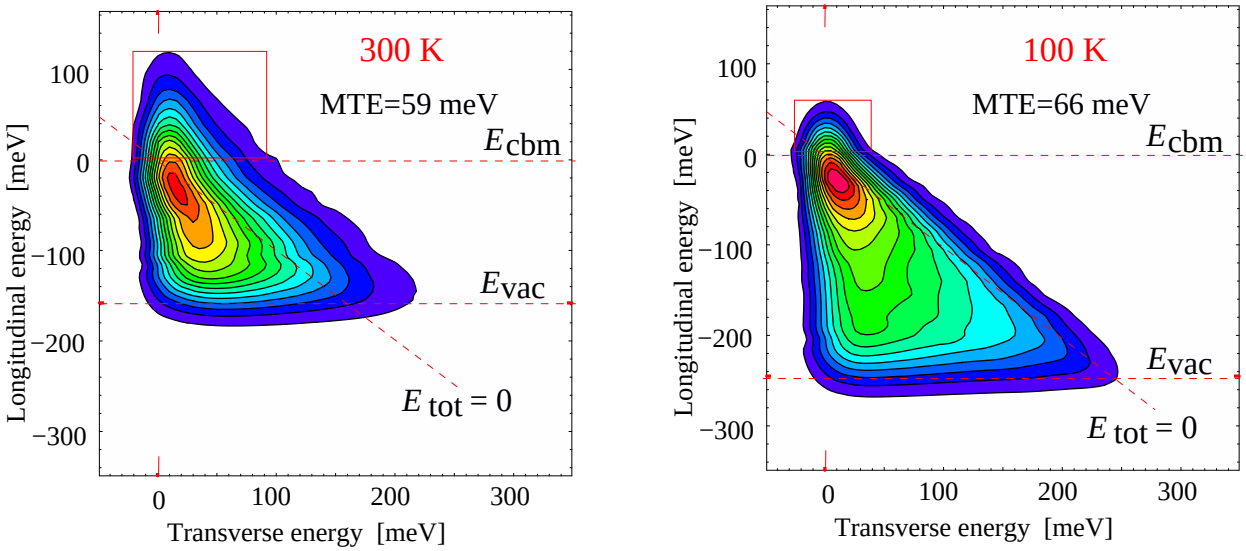

Fig. 4.9: *Contour plot of the electron energy distributions at room and low temperature. The line with vanishing total energy ($E_{tot} = 0$) corresponds to electrons initially situated in states about E_{cbm} in the bulk which are scattered mainly elastically.*

and blocking all electrons below E_{cbm} enables us to extract longitudinally and transversely thermalized electrons. These electrons are contained in the red boxes of Fig.4.9.
Since they play the crucial role in beam preparation from photocathodes, a corresponding performance parameter analog to QE_{tot} is defined. For the *effective* quantum efficiency only the yield of electrons contained in states above E_{cbm} are counted:

$$QE_{eff} = N_{el,\ eff}/N_{h\nu}.$$

Regarding the differential mean transverse energy $d\langle E_\perp \rangle$ of sub-ensembles defined by a fixed longitudinal energy $E_\parallel^b$ (see Fig.4.10), one finds for these electrons at longitudinal energies above E_{cbm} that $d\langle E_\perp \rangle$ stabilizes at (23 ± 2) meV (rt) and (6 ± 2) meV (lt). It demonstrates the diminishing effect of low temperature on transverse spreads. The values are slightly smaller than $k_B T_{bulk}$ (25.8 meV, rt and 8.6 meV, lt) which can be an indication for subthermal emission. However, the deviation is close to the present resolution limit and this point remains to be clarified. It is seen that the adjustment of a cutting barrier to arbitrary values higher than $\approx E_{cbm}$ allows to extract a transversely thermalized electron ensemble. Evaluation of the number of electrons cut exactly at E_{cbm} show that at room temperature QE_{eff} amounts to $\approx$ 2.6 %. Below E_{cbm}, there is a linear increase of $d\langle E_\perp \rangle$ with decreasing $E_\parallel^b$. The slope shows a rise of $d\langle E_\perp \rangle$ by about half of the $E_\parallel^b$ decrease and is in agreement for both cases.
In order to determine more accurately the longitudinal exponential slope, EDCs were measured

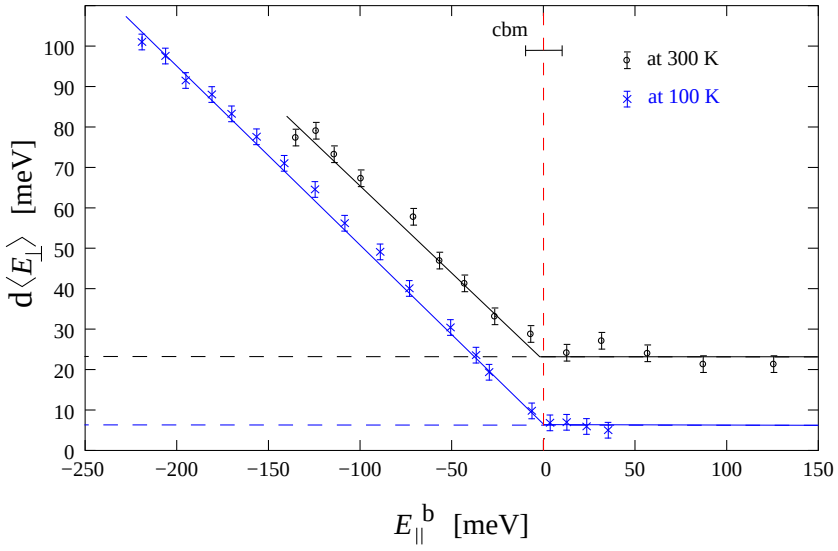

Fig. 4.10: *Differential mean transverse energy as a function of* $E_{\parallel}^{\mathrm{b}}$ *for room and low temperature. The dashed line corresponds to 23* meV *(rt) and 6* meV *(lt), the straight lines are added to guide the eye.*

with applied cutting and higher laser illumination for enhanced dynamic range. This determination showed (e^{-1})-intervals of (27 ± 1) meV (rt) and (12 ± 1) meV (lt), close to $k_{\mathrm{B}}T_{300\mathrm{K}} \approx 25.8$ meV and $k_{\mathrm{B}}T_{100\mathrm{K}} \approx 8.6$ meV. Small deviations of the longitudinal temperature, derived in this way, from the bulk temperature observed here are in agreement with other studies [Dro85, Ter94]. At low collector currents of typically integrated values of 10 pA, slopes can be fitted with a dynamic range of two orders of magnitude. Taking into account the limited analyzer resolution, it could be expected that, especially for the steeper slope at low temperature, a certain variance to higher values is inherent in the method. Electrons corresponding to the high energy part of the distribution seem to have suffered nearly no energy loss and momentum scattering during the passage through band banding region and surface barrier.
In this case longitudinal and transverse spreads are given by 27 meV and 23 meV, respectively. The low temperature operation enables to decrease these values substantially. Corresponding cutting yields QE_{eff} of ≈ 1 % (lt) at longitudinal and transverse spreads of 12 meV and 6 meV, respectively. This yield will be used to produce cold electron beams.

4.4 Studies on the transmission of the GaAs(Cs,O)-surface barrier

In order to find an optimum procedure for the activation of our photocathodes, a detailed knowledge about the evolution of the main parameters during the (Cs,O)-deposition is required.

At one side, the rise in QE_{tot} is mainly determined by a higher $|\chi_{\mathrm{eff}}|$. As mentioned in section 3.3.3, $|\chi_{\mathrm{eff}}|$ increases in the course of activation since successive adsorption of (Cs,O) at the surface lowers the vacuum level. In consequence, the minimum energy for electrons to escape to the vacuum decreases, resulting in additional contributions of low energy electrons. For very long activation times, however, it can be observed at longitudinal EDCs that this effect saturates and $|\chi_{\mathrm{eff}}|$ approaches a maximum value [Pas97].
On the other side, as seen in the evolution of the Cs-peaks for the standard activation curve on a freshly cleaned surface in Fig.4.11 (a), QE_{tot} reaches a maximum after ≈ 1.5 ML of Cs-coverage and drops almost linearly later on. This behavior was confirmed up to very strongly overactivated cathodes ($t \geq 300$ min). Thus, QE_{tot} is not completely governed by $|\chi_{\mathrm{eff}}|$. The linear dependence of QE_{tot} for over-activated cathodes with almost stable $|\chi_{\mathrm{eff}}|$ is in agreement with the linear increase in layer thickness during the activation as shown by the number of monolayers (black arrows) constituted on the surface. A counteracting thickness effect apparently partly compensates a further increase of $|\chi_{\mathrm{eff}}|$.
In order to clarify this behavior, a separation of the transmission through the surface potential barrier from effects of higher $|\chi_{\mathrm{eff}}|$, mainly on low energy electrons, is desired. High energy electrons will serve as a probe for the transmission and allow us to find an activation time range in which we have almost optimal QE_{eff}. Stability considerations then establish the best activation procedure among these and constitute an optimized preparation of our photocathodes.

In Fig.4.11 (b), longitudinal EDCs at different steps of activation are plotted. The colors refer to the colored arrows in the activation curve above. A clear shift of the left edges of in the spectra to more negative energy demonstrates a decreasing vacuum level during the activation. At the high energy side, governed by the combined density of states according to $k_{\mathrm{B}}T$ of electrons in the bulk, a vertical shift is observed between most of the spectra. The magnification of this part between $U_{\mathrm{bias}} = -2.6$ V and -2.5 V (c), proves well the exponential drop. Straight lines, fitted to this high energy tail were used to determine the relative vertical shifts for the different curves. Referred to the blue curve (100 %), the transmission drops to 78 % (green), 59 % (light blue), and 37 % (brown) at the respective activation steps within an accuracy of $\pm$ 3 %. The lowest, red curve, corresponding to the 1$^{\mathrm{st}}$ Cs-peak at the activation, exceeds only slightly the range of resolution. It was compared separately to the blue curve in picture (d). The resolution limit can be estimated by the noise contributions in the lowest decade. In order to minimize the influence of the noise as well as of deviations from the exponential dependence close to the peak, the curves were compared only in the indicated range. With an accuracy of $\pm$ 10 %, a transmission equal to that of the blue curve was obtained.
The absolute amount of electrons obtained within a certain interval of bias voltages at the regarded high energy tail depends strongly on the overall performance of each cathode. To show

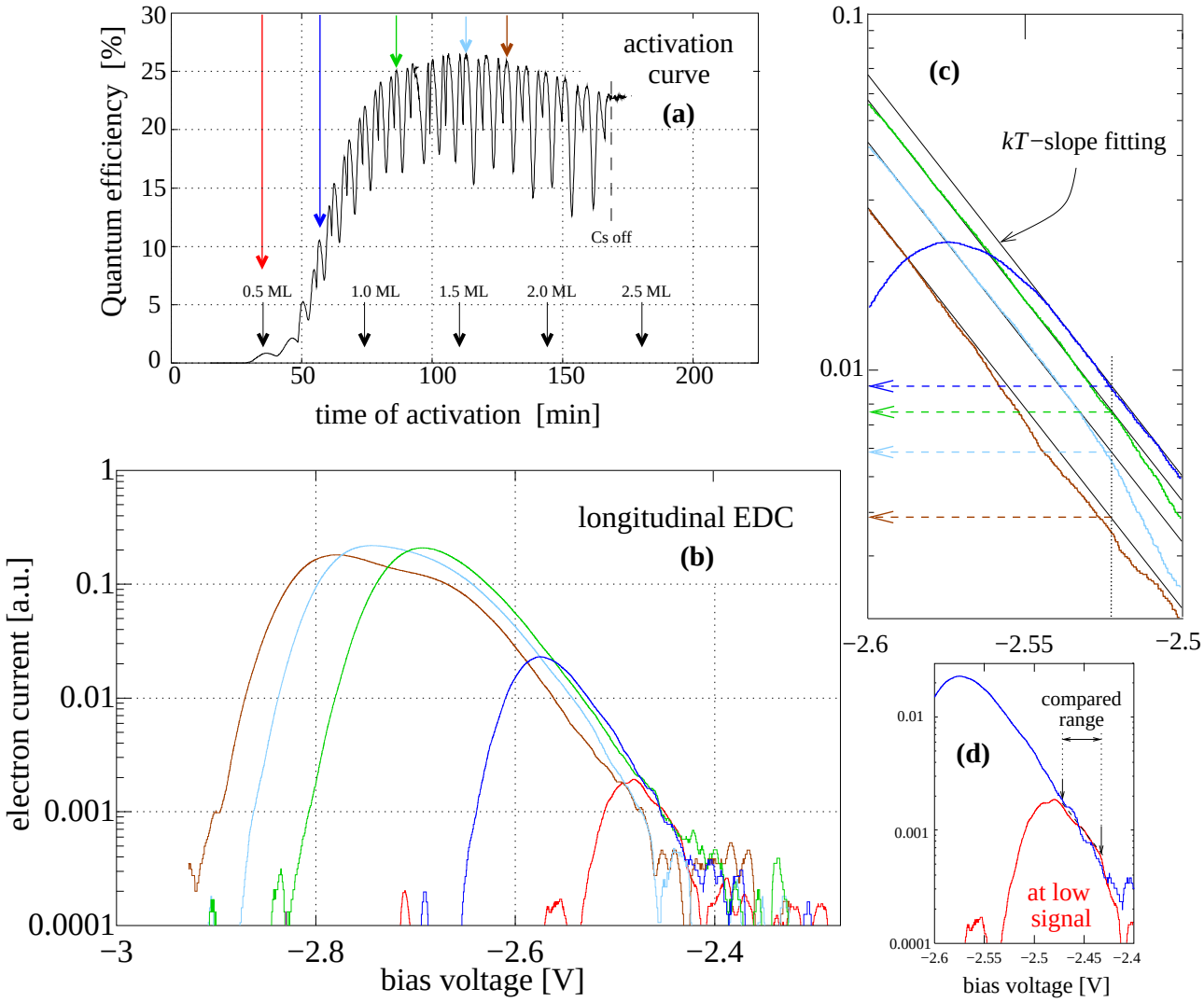

Fig. 4.11: *Full activation to maximum QE_{tot} (a). The activation was interrupted at times indicated by the colored arrows and longitudinal EDCs were measured (b). In order to show the fitting of exponential kT-slopes, magnified views of the blue reference curve and the curves taken at higher activation times (green, light blue, brown)(c) as well as the blue curve and and the red curve (d), are shown.*

the general trend of the transmission during the activation process, several series, representing different cathodes but also different activations of the same sample, were measured. The relative transmissions, scaled to equal initial values to permit a comparison, are plotted in Fig.4.12. At positive χ_{eff}, below the 1$^{\mathrm{st}}$ Cs-peak, blocking of electrons with energies even above vacuum level leads to very low signals. The first data point of each curve represents, therefore, the situation at the first Cs-peak, where a steep photocurrent onset enables longitudinal energy measurements. Except for the blue one, all curves are in agreement at the first and second

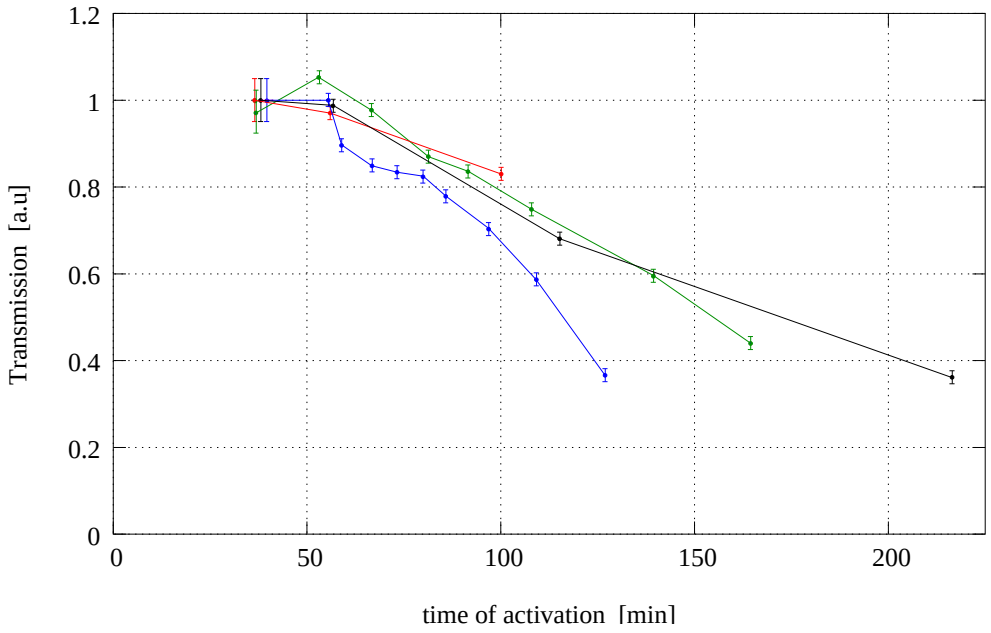

Fig. 4.12: *Relative transmission during the activation process, shown for different activations and samples (see text). The blue curve corresponds to the activation of Fig.4.11*

data point. A small deviation in case of the blue curve can be attributed to the low accuracy at the beginning. Later on, the activation runs differ in their slope, however, a clear tendency of decreased transmission is observed at higher activation times. The 50%-drop occurs in the range from 120 min to 175 min, representing ≈ 1.5-2.5 monolayers of Cs-coverage. This variance demonstrates that still the individual activation conditions strongly influence the transmission. Comparing the initial transmission to values obtained at about 110 min, corresponding to the maximum QE_{tot} at 1.5 ML, one observes a decrease to 60 % - 75 %. Hence, QE_{eff} can be enhanced accordingly for thinner activation layers. The constant regime of thin layers can be considered as range of activation with almost optimal QE_{eff}. It corresponds to the interval between the first and third cesium peak, at 0.5 - 0.7 monolayers of Cs coverage.

The complete energy distribution $N(E_{\parallel}, E_{\perp})$ for three layer thicknesses in different activation regimes at 100 K is presented in Fig.4.13. Respective activation states are indicated on the top with red arrows.

The left distribution (1) was obtained with a thin activation layer of ≈ 0.7 ML. At this state, $|\chi_{\mathrm{eff}}|$ and low temperature $QE_{\mathrm{tot}}^{100\mathrm{K}}$ amount to 120 meV and 16 %, respectively. The middle distribution (2) shows an activation to maximum $QE_{\mathrm{tot}}^{100\mathrm{K}}$ of 29 % (≈ 1.5 ML) at $|\chi_{\mathrm{eff}}| = 240$ meV, already compared in the previous section 4.2 to a room temperature spectrum. The right distribution (3) was received for a typical over-activated cathode (≈ 2.3 ML) with $QE_{\mathrm{tot}}^{100\mathrm{K}}$ of

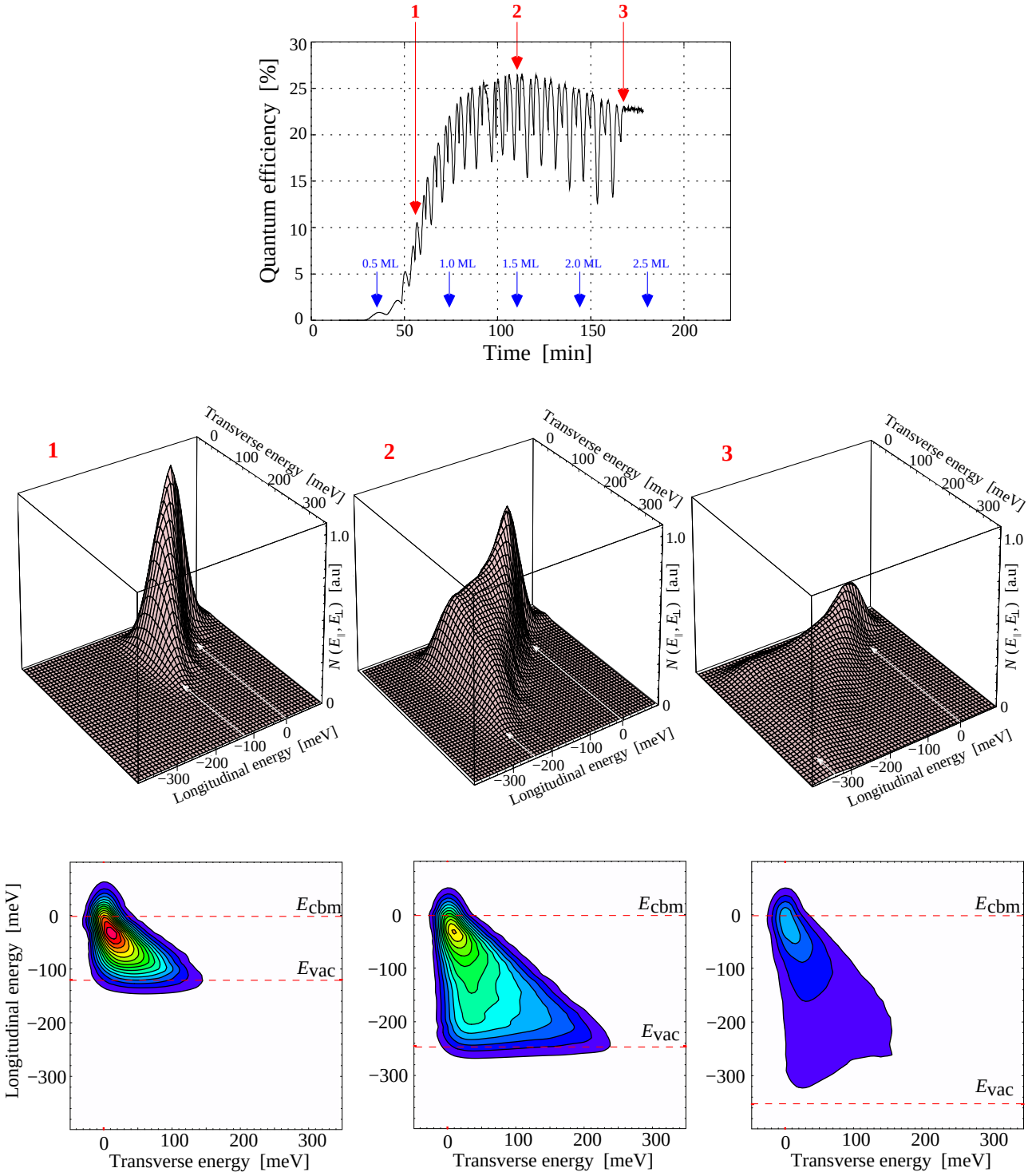

Fig. 4.13: *Electron energy distribution comparison for three different layer thicknesses. The running activation was interrupted at the three times indicated on the top to determine the energy distributions shown in 3D- and contour plots below. The diagrams in the middle correspond to full activation to maximum* QE_{tot}.

25 % at $|\chi_{\text{eff}}| = 320$ meV. The peaks are located to good approximation at $E_{\perp} \approx 6$ meV and $E_{\parallel} \approx$ -25 meV for all spectra. Independently of the thickness, the nose-like shape of the distribution ($E_{\text{cbm}} \geq 0$) remains unchanged apart from the number of electrons contained. Referred to the standard "maximum QE_{tot}"-activation ((2) in Fig.4.13), thin and thick (Cs,O) layers exhibit clear changes. In the following, the changes will be demonstrated in comparison to this standard activation.

For thin layers ((1) in Fig.4.13), the plateau is no more visible because of the cutting by the vacuum level. This removal of electrons with a high average transverse energy decreases indeed the mean transverse energy (no cutting barrier) from ≈ 66 meV to ≈ 37 meV. The peak height rises by a factor of 1.3, which is a clear evidence for increased transmission. On the other side, at thick layers ((3) in Fig. 4.13) the plateau becomes very broad and extends still up to the vacuum level even though the filling of these states is poor. The peak height falls by a factor of ≈ 0.5.

Based on these data, an enhancement for QE_{eff} by a factor of 1.3-1.5 can be realized with thin (Cs,O)-layers. At 0.7 ML of Cs-coverage one can reach high transmission of the GaAs(Cs,O)-vacuum interface for cold electrons associated with a $|\chi_{\text{eff}}|$ of ≈ 120 meV. An additional potential barrier can adjust the cutting level for electrons to longitudinal energies below E_{cbm}. The later finite rise of $|\chi_{\text{eff}}|$ in the course of possible degradation or due to small surface photovoltage effects under operation (cp. section 2.4) will not effect cutting until the vacuum level remains below the additional potential barrier. This should allow operating conditions, with photocathode lifetimes as reported in 3.4.1, at the upper end of the constant transmission range (≈ 0.7 ML).

4.5 The effective quantum yield for cold electrons

In the preceding investigations at small electron densities, thin activation layers (0.7 ML thickness of Cs coverage) were found to enable stable and efficient emission of thermalized electrons from GaAs(Cs,O).

An electron beam with longitudinal and transverse spreads of ≈ 27 meV and ≈ 23 meV, respectively, can be prepared under room temperature operation conditions with an *effective* quantum efficiency of 3.4 % to 3.9 % by cutting at E_{cbm}. The normalized effective emittance $\boldsymbol{\epsilon_{x,n}}$ (see appendix A) amounts to 0.64 mm-mrad in this case.

Low temperature operation has proven to enhance the beam quality substantially. Beams with longitudinal and transverse spreads of ≈ 12 meV and ≈ 6 meV, respectively, are received at ≈ 100 K. The *effective* quantum efficiency reached 1.3 % to 1.5 %. The normalized effective emittance $\boldsymbol{\epsilon_{x,n}}$ amounts to 0.33 mm-mrad at low temperature.

Based on these parameters it is necessary to apply a laser power of the order of 1 W to produce total beam currents in the range of a few mA. Since the low temperature conditions have to be kept during operation, good cooling performance is required.
An electron gun meeting these requirements will be presented in the following chapter.

4.6 Implementation and first tests of the atomic hydrogen cleaning

In order to implement the hydrogen cleaning for the GaAs-photocathodes in our preparation procedure, in a first step, temperature calibrations for the tungsten capillary and the samples were performed (hydrogen chamber, see chapter 3, Fig.3.7). The temperature of the tungsten capillary was measured pyrometrically at the outlet of the tube in dependence of the electron bombardment heating. According to reference [Bis93], the temperature was adjusted to $\approx$ 2000 K (at the tube center as seen from below; the tube walls showed temperatures of about 1800 K under the same conditions). For the sample temperature, determined by photoluminescence spectroscopy, we performed a calibration against the oven filament current for the range 300°-490°C.

In a first test of the hydrogen cleaning method, a series of 15 preparation procedures based on hydrogen cleaned surfaces was performed with the same cathode along the following scheme. Each freshly (H•)-cleaned photocathode was transferred to the preparation chamber and activated to maximum quantum efficiency. This 1^{st} activation was followed by a standard heat cleaning at 430°C for about 40 min, but without intermediate (H•)-cleaning. Then after the 2^{nd} activation, the samples were used for test measurements and degraded. Subsequently, the steps of heat-cleaning, activation and degradation followed several times until quantum efficiency could not be recovered with this procedure and the photocathodes were, therefore, passed back to the hydrogen chamber for the next (H•)-cleaning run.
The standard heat cleaning at moderate temperature is known *not* to remove all Cs from the surface. Only weakly bound Cs atoms desorb at this heat cleaning, while some surface sites are still occupied by Cs-atoms. This results in a reduced cesiation time until the first Cs-peak for surfaces with a residual Cs-coverage. After a *re-activation*, the cesiation time to reach the peak is typically half as long as for the first activation following a *successful* (H•)- or a wet-chemical cleaning. This opens up the possibility to establish a criterion to estimate the Cs-removal by the cleaning procedure. If the cesiation times for an emerging first Cs-peak at the 1^{st} activation after the (H•)-cleaning procedure is close to the time required for further *reactivations*, it is a sign of incomplete Cs-removal. A successful (H•)-cleaning, in contrast features a longer cesiation time, typical for conventionally prepared cathodes. The result with respect to this estimation is given in Tab.4.1 under "Cs-removal". As direct observation techniques

cleaning cycle	T_{exposure} x P_{H_2}	T_{GaAs}	Cs removal	QE_{tot}
1	10 min x 1.8 mbar	420°C	Yes	**18.2 %**
2	30 min x 1.8 mbar	420°C	Yes	**19.4 %**
3	15 min x 1.5 mbar	460°C	Yes	**19.4 %**
4	15 min x 1.8 mbar	440°C	Yes	**19.4 %**
5	10 min x 1.6 mbar	440°C	Yes	**20.7 %**
6	10 min x 1.5 mbar	440°C	Yes	**19.3 %**
7	10 min x 1.7 mbar	440°C	Yes	**17.2 %**
8	10 min x 1.7 mbar	440°C	Yes	**20.6 %**
9 *	11 min x 1.8 mbar	25°C	No	**15.0 %**
10	10 min x 1.8 mbar	25°C	Yes	**10.0 %**
11	10 min x 1.8 mbar	≈ 490°C	Yes	**19.2 %**
12	10 min x 1.8 mbar	≈ 490°C	Yes	**20.0 %**
13	10 min x 0.18 mbar	≈ 490°C	Yes	**17.4 %**
14	10 min x 0.017 mbar	≈ 490°C	Yes	**15.9 %**
15	10 min x 0.017 mbar	≈ 490°C	Yes	**15.9 %**

Tab. 4.1:
Hydrogen cleaning cycles with the same photocathode
*) H_2 flow in stead of (H•).

of the surface morphology and composition are not available in our set-up, we evaluate the activation performance of a NEA-GaAs cathode cleaned with atomic hydrogen mainly by its maximum quantum efficiency (@ 670 nm). In the second column, the settings for the cleaning are indicated with the time of (H•)-exposure and the H_2-pressure at the entrance of the tungsten capillary as a measure for the flow of H•. Column three shows the sample temperature during the (H•)-cleaning. In a conventional preparation based on wet-chemical etching, the photocathode used for this series showed a quantum efficiency of almost 20 %. The first cleaning cycles (1-8) were performed under slight variation of the dose between 10 min. to 30 min. at an H_2-pressure of 1.8 mbar and sample temperature between 420°C and 460°C. The cesiation times

fulfilled the criterion of a complete Cs-removal and the quantum efficiency recovered in all eight cycles without noticeable influence of the parameter variations. Cleaning cycle no.9 and 10 were performed with a room temperature sample. Since in case 9 even the W-capillary was not heated, the situation describes a simple flow of molecular hydrogen to the unheated surface which showed an activation pattern without Cs-removal. In case no.10, the capillary was heated and the situation should represent a cleaning by atomic hydrogen at room temperature. The Cs was removed, but the quantum efficiency has fallen even below the previous case indicating a poor surface quality. Then, when the samples were heated again at temperatures of $\approx 490°C$, Cs-removal and high quantum efficiency was reached again in cycle no.11 and 12. Cleaning cycles no.13 and 14/15 should explore the influence of doses decreasing by a factor of 10 and 100, respectively. Obviously, the Cs is still removed, but the QE reveals a worse surface quality with decreasing (H•)-doses.
Energy distributions measured during some cycles with high QE did not exhibit significant differences to those of conventionally cleaned photocathodes. The whole series demonstrates successfully the possibility of an *in vacuum* cleaning for our photocathodes with recovered performance, which enables us to operate them without time-consuming wet-chemical steps outside the vacuum on a largely extended timescale. However, the present investigations can not yet resolve any morphological advantages over our conventional wet-chemical cleaning. Work towards this is in progress.

In order to explore the effect of a surface smoothing as it is hoped for to occur in the application of atomic hydrogen as well as to investigate and optimize the surface morphology and structure under different cleaning conditions for our photocathodes, a second hydrogen source was built. It will be operated by the group at the Institute of Semiconductor Physics in Novosibirsk, where several direct surface diagnostic techniques are available.

5. A cryogenic photocathode gun based on GaAs(Cs,O)

The realization of a GaAs(Cs,O)-based electron gun capable of supplying a few milliamperes electron current with energy spreads below 10 meV is presented and discussed in this chapter. Particular importance in the construction was given to maintaining a low temperature of the cathode under high intensity laser illumination.

The first section discusses the geometrical restrictions in the electron target and the requirements regarding the thermal performance as well as the electrical arrangement. Section 5.2 is dedicated to the presentation of our cryogenic electron gun solution. In section 5.3, measurements on its thermal stability under intense laser illumination working conditions are reported. The closing section shows the implementation of the cryogenic photoelectron gun at the new electron target section of the Heidelberg Test Storage Ring.

5.1 Electron gun design aspects

The GaAs(Cs,O) photocathode lifetime measurements at high currents of about a milliampere demonstrated the possibility to obtain intense and stable electron beams (see section 3.4.1). We also found that an ensemble of cold electrons is obtained after filtering out the high energy part of the distribution; however, the quantum efficiency decreases strongly from $QE_{\mathrm{tot}} \approx 20\%$ - 27% to $QE_{\mathrm{eff}} \approx 1\%$ (see chapter 4).
In order to get both, cold *and* intense electron beams, high laser intensities have to be applied which in turn increase the heat load on the photocathode.
Although our present test gun is equipped with a double wall gun tube flooded with LN_2, the stabilization temperature without laser illumination is about 25 K above $T_{\mathrm{LN_2}}$ (77 K). Laser heat load measurements based on photoluminescence spectroscopy showed a strong cathode heating of at least 330 K/W at higher under laser illumination [Wei00]. The resulting temperature under LN_2-cooling for the envisaged operation at about 1 W exceeds room temperature

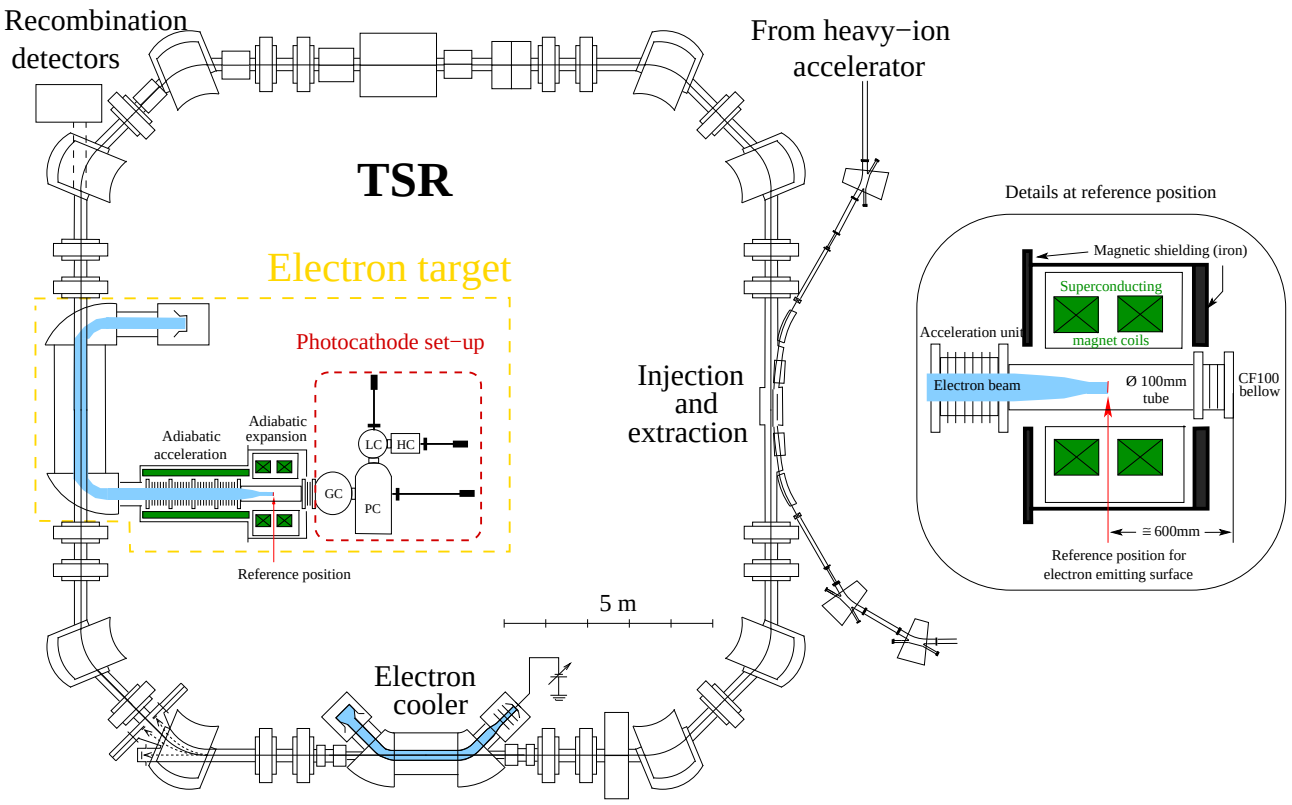

Fig. 5.1: *E-Target with photocathode set-up, i.e. gun chamber (GC), preparation chamber (PC), loading/hydrogen chamber (LC, HC) at the TSR. A detailed view of the region around the reference position for an electron emitting surface is shown on the right side.*

and practically causes the desorption of the (Cs,O) activation layer.
Since the entire gun construction around the AlGaAs/GaAs heterostructure (including the substrate that the semiconductor is bonded to) influences the thermal conditions of the photocathode, a new electron gun was designed and built in order to fulfill the geometrical, thermal, mechanical, and electrical requirements. These requirements will be discussed below.
The U-shaped electron target is placed in one of the linear sections of the TSR (see Fig.5.1). It can be equipped optionally with a thermionic electron gun or the photocathode electron gun. Presently it is tested and run with the thermionic gun [Spr03]. Relevant geometrical restrictions are indicated on the right side of Fig.5.1. For illustration reasons, the electron gun region is shown with an exemplary electron emitting surface, representing the AlGaAs/GaAs heterostructure (red), and an electron beam (blue), but without all parts belonging to a possible electron gun construction.

Precise and *stable positioning* of the emitting surface has to be ensured in the center of a ϕ 100 mm - tube. It should be placed perpendicular to the guiding magnetic field within

$\pm$ 5° and centering in the magnetic field maximum position of the superconducting magnetic coils to better than $\pm$ 1 mm is required. This position and the closest accessible flange outside the magnetic shielding are at a distance of about 600 mm.

The possibility of an *independent* electron gun axis *adjustment*, defining the extraction field axis by the electrodes mounted in front, would allow precise alignment of the electric and magnetic field. To fulfill the conditions, from a mechanical point of view, a cantilever construction attached to the accessible flange is desirable. Furthermore it would enable electrically insulated mounting far off the geometrically restricted area at the cathode position. The electric insulation with respect to ground should keep voltages up to 20 kV.

Special care is demanded for the electric *extraction fields* in case of the photocathode electron gun to preserve the initially much lower electron temperature in comparison to the thermionic gun. The electrode arrangement should avoid strong beam heating effects as far as possible by sufficiently slow and homogeneous acceleration. Unwanted electric fields originating from adsorbates, material contaminations and roughness near the cathode should be minimized especially near the cathode, since electrons at low velocities are most sensitive to inhomogeneities.

The choice of *vacuum materials* is strongly restricted in order to maintain an active GaAs(Cs,O) surface with low degradation. Certain contaminations, in particular oxygen species, are especially harmful even at low partial pressures. Excellent base vacuum conditions near the cathode ($p \lesssim 10^{-11}$ mbar) are essential to avoid degradation due to efficient residual gas absorption at the cold cathode surface. Vacuum conditions even in a wider area of the acceleration region at the electron target can influence the performance via destructive high energy backflow of ionized gas particles.

Access is required for photocathodes, in contrast to thermocathodes, in several respects. Laser light has to be shined in either from front or back side during the operation. The reported lifetimes (see section 3.4.1) demand additionally direct "in vacuum"-access since degraded cathodes have to be replaced by freshly activated ones regularly about every 10 h during a running beamtime to enable a "quasi-continuous" operation. From a thermal point of view, this flexible cathode access causes problems, since it must be realized with good thermal conductivity (i.e. low thermal resistance).

The design has to account for stabilizing the active GaAs-layer at low temperature under the required heat loads. In Figure 5.2, a typical thermal chain for a photocathode electron with the coolant (LN_2) on one side and the GaAs sample under laser illumination on the other side, is shown schematically. All elements between these two have to be chosen according to optimal thermal properties. The sample temperature is determined by the heat load and the cooling performance of the thermal chain. Each bulk link and especially the interfaces contribute

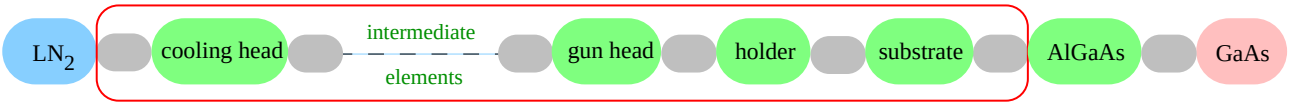

Fig. 5.2: *Schematic thermal chain of typical elements.*
Coolant LN_2 (blue) and heated GaAs (pink) are intended to link thermally. Bulk resistances (green) and especially each interface resistance (gray) determine the cooling performance of the entire chain.

with specific temperature gradients (per applied power) and thus increase the resulting sample temperature. The first chain links next to the AlGaAs/GaAs-heterostructure are its bonded interface to the substrate and the substrate bulk itself. The adjacent element, the holder keeping the substrate and allowing manipulators to take and move the sample, thermally contacts the gun head. Further on the gun head is linked to a cooling head via several intermediate elements. All elements in the red box of Fig.5.2 are basically controlled by the electron gun design.

Concerning the bulk links of the chain, thermal properties are well known and several UHV-materials with a high thermal conductivity can be found for the relevant temperature range around LN_2-temperature [Pob96].
Concerning the dry interfaces between dissimilar materials, the thermal conductivity depends strongly on surface roughness, flatness and hardness, as well as the temperature and pressure. Some of these parameters, especially the surface specific ones, are often either not very well known or hard to optimize. Data on these interfaces are reported for technically important materials like copper and stainless steel [Gme99]. Bonded interfaces can be roughly estimated considering the similarity of the two structures and the quality of the bonding technique. The $Al_{0.4}Ga_{0.6}As$ and GaAs layers for example were epitaxially grown and differ by less than 0.1% in a key property, the lattice constant [Ada85]. This allows us to regard to good approximation the whole heterostructure thermally as one bulk material. Thermal interface resistance between this heterostructure and the substrate, however, can considerably contribute to the temperature increase in the GaAs sample (see section 5.3.2).

5.2 A cryogenic photocathode electron gun

Based on the experience with the test gun, a new electron gun, including a new sample design and cathode insertion mechanism into the gun, was constructed to operate a cold, intense electron beam meeting the requirements at the electron target as given in previous section 5.1.

In this section our cryogenic GaAs(Cs,O) photocathode gun and its thermal performance are presented.

5.2.1 Electrical aspects

The upper end of the electron gun head and the electrode arrangement providing electric extraction and acceleration fields near the cathode are illustrated in Fig.5.3.

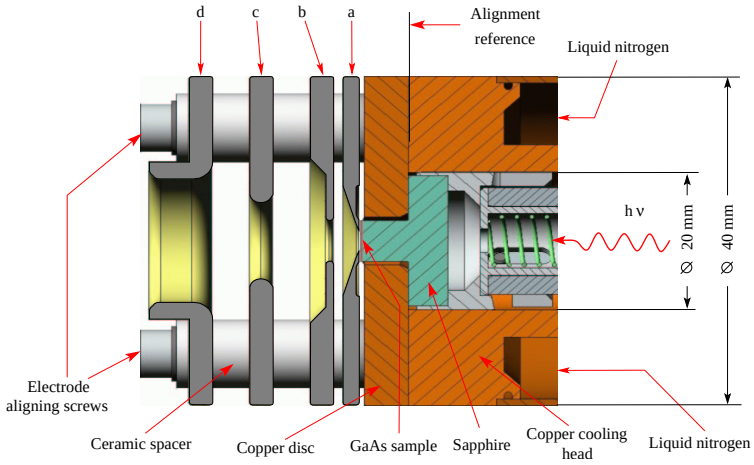

Fig. 5.3: *Sketch of the rotationally symmetric electron gun head and electrode arrangement (90°-cut).*

The dimensions of the rotationally symmetric construction (gun body ϕ 40 mm, outermost electrical contacts of electrodes at 29 mm off-axis) are limited by the insulation distance to the tube walls at 20 kV. An axial channel enables cathode access from behind (right side) and is surrounded by a LN_2-reservoir. The retracted face of the sapphire substrate is pressed to a terminating copper disc while the surface with the GaAs layer has no contact to other materials and is positioned at a distance of 0.2 mm from the Pierce electrode (a). The extraction (b) and outer (c,d) electrodes follow the Pierce electrode at distances of 2.4 mm, 10.0 mm, and 17.6 mm.

A *contactless* positioning of the cathode with respect to the Pierce shield enables all four electrodes and the cathode to be biased independently. In addition it ensures a durable GaAs surface quality. A hole of 3 mm diameter in the Pierce shield restricts the initial electron beam size to less than half of the active GaAs(Cs,O) surface. Edge effects due to small vertical variations of the cathode center after the insertion are thus excluded. All the stainless steel electrodes are gold plated in order to avoid oxidation and residual gas adsorption which can lead to electric field distortions.

Generally two *extraction regimes* are distinguished. At higher extraction fields all emitted

electrons are accelerated and leave the region near the cathode. In this so called *current limited regime*, a further increase of the voltage does not strongly effect the drawn electron current. With decreasing electric field electrons begin to stay longer near the cathode. Due to their space charge, a barrier is built up for electrons emitted subsequently. In this *space charge regime*, the barrier height and consequently the number of electrons with sufficient energy to overcome the barrier is governed by the extraction field strength. With a present space charge cloud the drawn electron current follows relation

$$I_{\mathrm{el}} = P \cdot U_{\mathrm{extr}}^{3/2}. \tag{5.1}$$

The factor P, called Perveance (in units Perv = $\mathrm{AV}^{-3/2}$), is determined by the special geometry at the extraction region of the electron gun and amounts in our case to ≈ 1.1 μPerv. Thus, the extraction voltage for I_{el} of about a milliampere is ≈ 100 V.

In the space charge regime, the Pierce geometry provides boundary conditions simulating a potential of an infinitely extended space charge cloud in front of the cathode. Transverse electric field components - leading to beam heating - vanish due to symmetry reasons. These Pierce conditions are based on equal potentials at Pierce shield and cathode. The differences in work functions between the activated cathode ($\varphi \approx 1.2$ eV) and the gold plating ($\varphi \approx 5.1$ eV) have to be accordingly compensated by an appropriate voltage applied to the Pierce shield.

Since the cathode axis requires *accurate alignment* along the electric field axis in a self-controlled way at each insertion into the gun, a large surface of high flatness at the left end of the copper cooling body, denoted alignment reference in Fig.5.3, serves as reference plane for the electrodes and the substrate. The electrode arrangement is kept by three screws at positions defined by precise ceramic spacers. Through cut-outs in the copper disc (not seen in the figure), the whole electrode unit is pressed directly to the reference surface. The highly flat right side of the copper disc is joint to the copper cooling head and provides at an area between $\phi_{\mathrm{i}} = 7$ mm and $\phi_{\mathrm{a}} = 20$ mm which forms the contact surface to the retracted face of the sapphire substrate. The GaAs surface will be oriented parallel to the reference plane as long as pressure keeps sapphire and copper in touch.

In order to evaluate beam heating effects during *acceleration*, two different regimes were simulated for the electrode geometry earlier [Pas97]. Equipotentials and electron trajectories are shown in Fig.5.4. For a gradual acceleration to 1000 eV (case I), the transverse energy increases by 0.2 meV at the outer trajectory. Therefore, using all electrodes, even higher kinetic energies at the extraction can be realized with low beam heating.
At fast acceleration to 100 eV (case II), the value at the outer trajectory amounts to 0.05 meV and decreases to $2{\cdot}10^{-4}$ meV for the central trajectory. Since a magnetic field suppresses heating and the field strength in the target (≥ 2000 G) exceeds the assumed 500 G of the simulation,

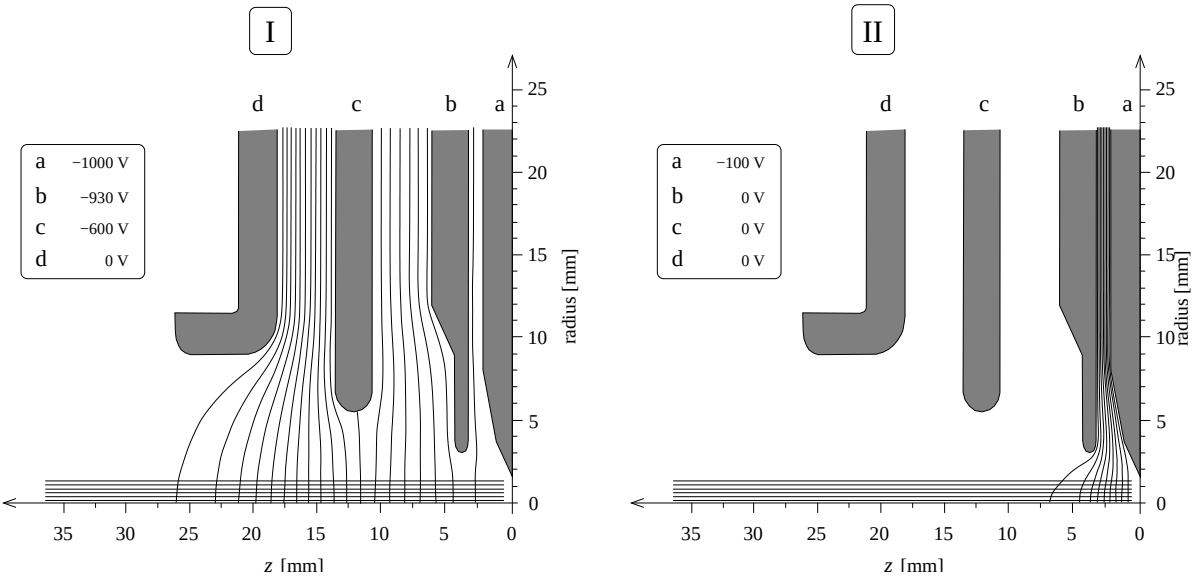

Fig. 5.4: *Numerical simulation of the electrode geometry for two different voltage settings: I. slow acceleration to 1000* eV, $U(z) \propto z^{4/3}$ *II. fast acceleration to 100* eV, *(b,c,d) grounded*

even lower values should be received. Accordingly, transverse heating due to acceleration could be effectively eliminated within a slow regime up to the keV-range.

5.2.2 Low temperature stabilization

5.2.2.1 Thermal chain and material choice

Regarding the exemplary thermal chain in Fig.5.2, the aim of the gun construction to provide a good thermal connection between GaAs and coolant LN_2 requires reducing as far as possible the number of thermal elements in the chain and optimizing the remaining ones with respect to their bulk and interface conductivities.

The *electron gun head* was designed to serve directly as **cooling head**. A reservoir, supplied with a continuous flow of LN_2, encloses cathode and holder. In order to separate the cathode thermally from the room temperature tube, all parts in contact with cathode/holder are kept at low temperature. The copper cooling head extends over the cathode bayonet unit and largely over the high pressure unit (see Fig.5.5). The excellent thermal conductivity of copper ($\lambda_{\mathrm{UHV-Cu}} \approx 600$ W/m·K at low temperatures) keeps estimated resistance in the bulk below $R_{\mathrm{bulk}} = 0.1$ K/W for the given geometry. The copper disc serves to provide a highly flat contact area for the substrate. The Cu-Cu interface resistance of the disc and cooling body should be less than $R_{\mathrm{Cu-Cu}} \approx 0.2$ K/W (assuming literature values for polished and pressed

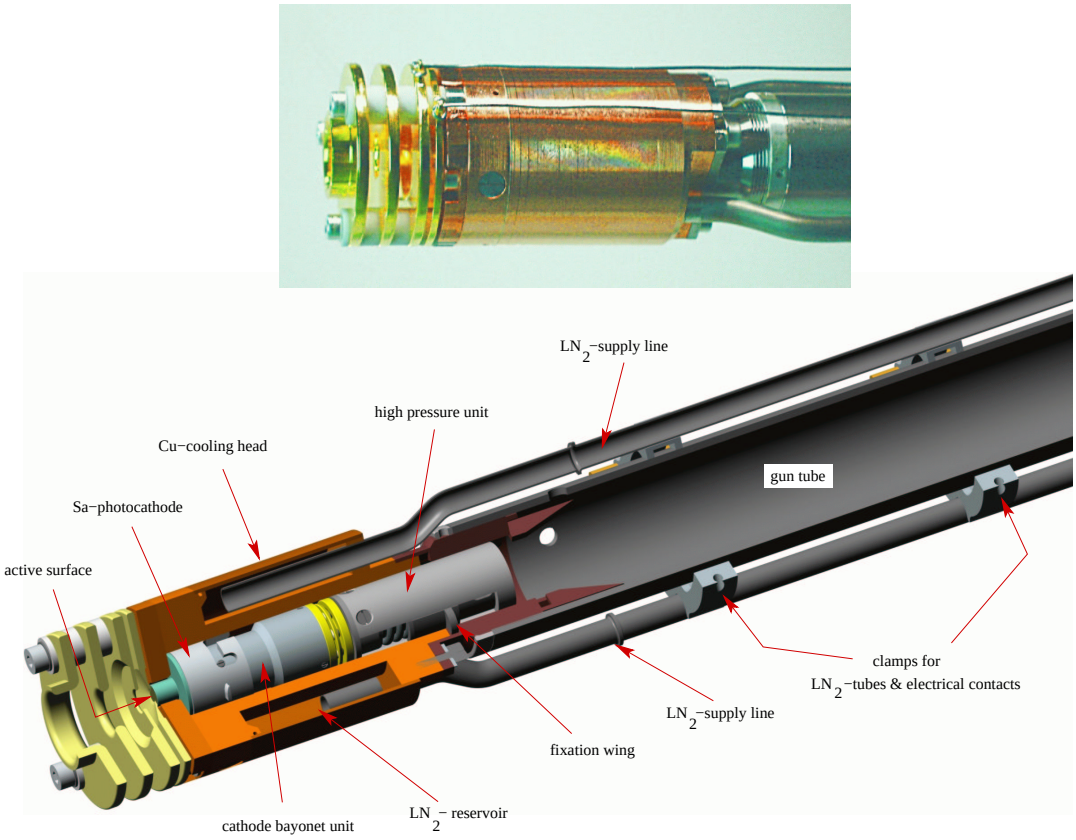

Fig. 5.5: *Electron gun head with inserted cathode and high pressure unit (120°-cut).*

Cu-joints). In total, an upper limit of 0.5 K/W can be assumed for the resistance in the entire cooling head.

The choice of materials for the **substrate** is restricted to materials transparent for the laser light and capable of serving as a base for a good bonding of the semiconductor layers. Sapphire exhibits in the low temperature range (80 K - 100 K) a thermal conductivity which exceeds even copper ($\lambda_{Sa} \approx$ 600-800 W/m·K). By a direct contact of the sapphire substrate with the copper cooling head, it is made sure that the holder is not included in the thermal chain. The titanium holder is mechanically connected by brazing sidewise to the metallized sapphire.

The **reduced thermal chain** of the new electron gun design shown in Fig.5.6 consists of three bulk elements and the respective interface resistances.

Due to its small dimensions (thickness 2 μm, $\lambda_{Sa} \approx$ 100 W/m·K) AlGaAs yields only a minor bulk contribution to the resistance but can play a role for the interface resistance.

Fig. 5.6: *Thermal chain of the new electron gun*

5.2.2.2 Interfaces

As stated in the section on design aspects, the thermal properties of the interfaces depend strongly on surface parameters which are not in every case precisely accessible and which can not be easily improved beyond the technical standard. We will, therefore, give a solution for our electron gun within the scope of commercially available parts and techniques.

The necessary **open interface** between sapphire and the cooling head, providing the access to the sample, was realized by a *pressed dry joint* of two high quality surfaces. The sapphire substrate was made of an "epi-polished" sapphire window blank trimmed to the special step-like shape shown in section 3.1. Its retracted face, provided to make a good thermal contact, as well as the copper counterpart, are standard polished to decrease roughness and flatten the surface. In order to press the sapphire to copper, a high pressure unit exerts force from behind to the installed cathode holder (see Fig.5.7).

The insertion of the cathode *under high force* ($\approx$ 200 N) is carried out with a magnetically coupled manipulator. In the preparation chamber, the cathode holder is docked to the high pressure unit using the cathode bayonet. A second rear bayonet mechanism enables the high pressure unit to be coupled to the manipulator head. All elements are pushed through the inner channel of the electron gun until the retracted substrate face touches the copper disc at its final position. Further pressure on the manipulator compresses the first, weakest spring (behind the button), then the spring at the rear bayonet and finally the high pressure spring. The courser behind the high pressure spring is moved forward and, by a rotation with the manipulator, its lateral wing can be fixed under pressure at a defined position. The rear bayonet opens during the rotation and the disengaged manipulator head can be pulled back. Since the pressure unit remains in the gun head, a channel of ϕ 6 mm allows laser light to be irradiated from behind. In order to facilitate and to center the motion along the gun tube, a guiding ball equipped with "bearing wheels" is mounted on top of the manipulator.

The photocathodes were developed and produced at the Institute of Semiconductor Physics in Novosibirsk and the bonding of the epitaxial grown AlGaAs to sapphire is done in the process of fabrication by thermo-compression bonding. The thermal resistance of such an interface can not reliably be predicted and will therefore be subject of an investigation in section 5.3.2.

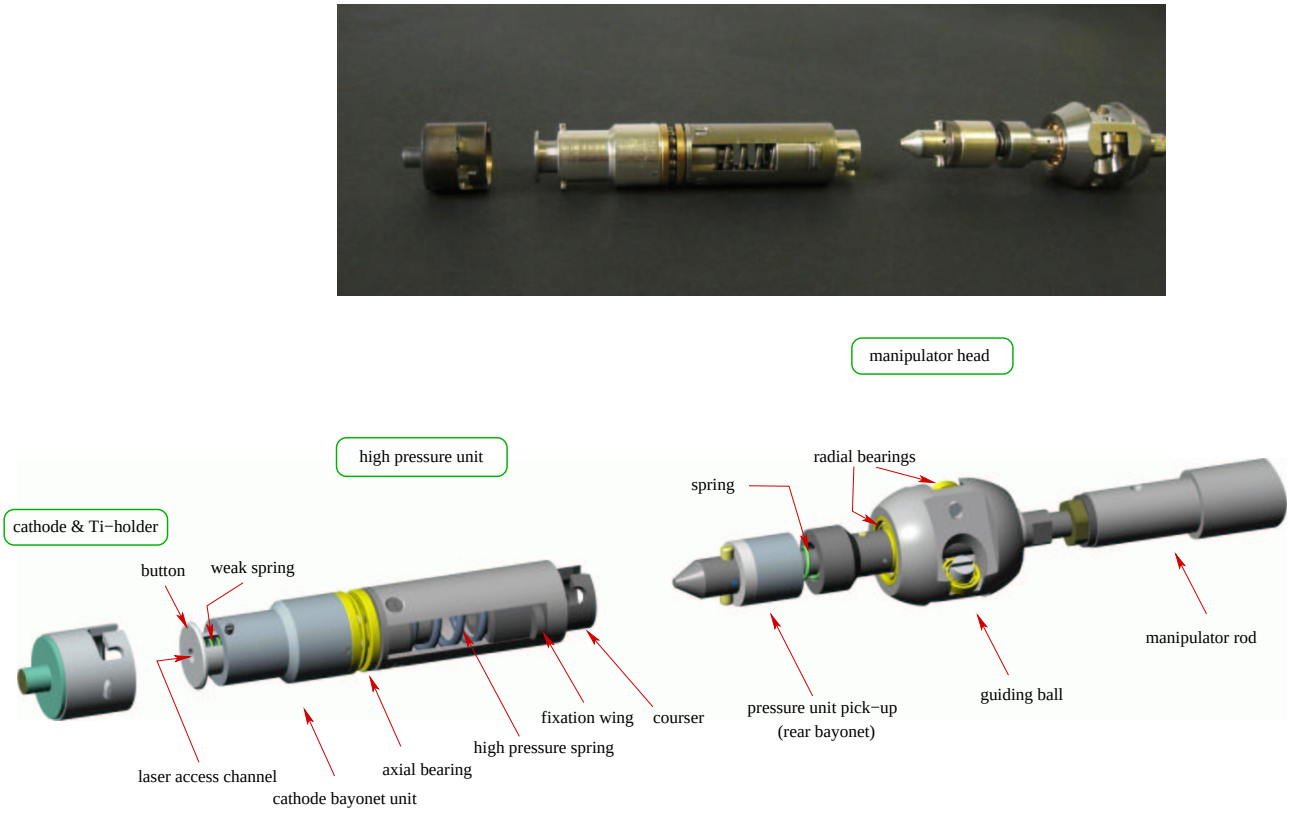

Fig. 5.7: *The mechanical elements providing high pressure on the joint between the sapphire substrate and the copper cooling head. The dark color at the cathode and its Ti-holder on the photography stems from the metal coating for the electrical contact.*

Epitaxially grown interfaces between GaAs and $Al_{0.4}Ga_{0.6}As$ are not expected to contribute remarkably to the overall resistance since the lattice structure of GaAs remains almost unchanged under replacement of gallium by aluminum atoms which benefits an efficient phonon transfer. The remaining interface in the thermal chain between the coolant LN_2 and copper also plays a minor role provided that nitrogen bubbles created at the copper surface do not inhibit further coolant contact (as it can happen for small hollows without effective drain of bubbles). At the relatively large dimensions of the contact and a continuous flow of LN_2 a sufficiently large bubble free area should always ensure effective heat dissipation.

5.2.3 Mechanical mounting

The mechanical support construction for the electron gun was designed to keep the gun electrically insulated and self-supported at the CF100 bellow of the electron target (see detailed view at Fig.5.1). A CF160-CF100 adapter flange links the photocathode set-up to the electron tar-

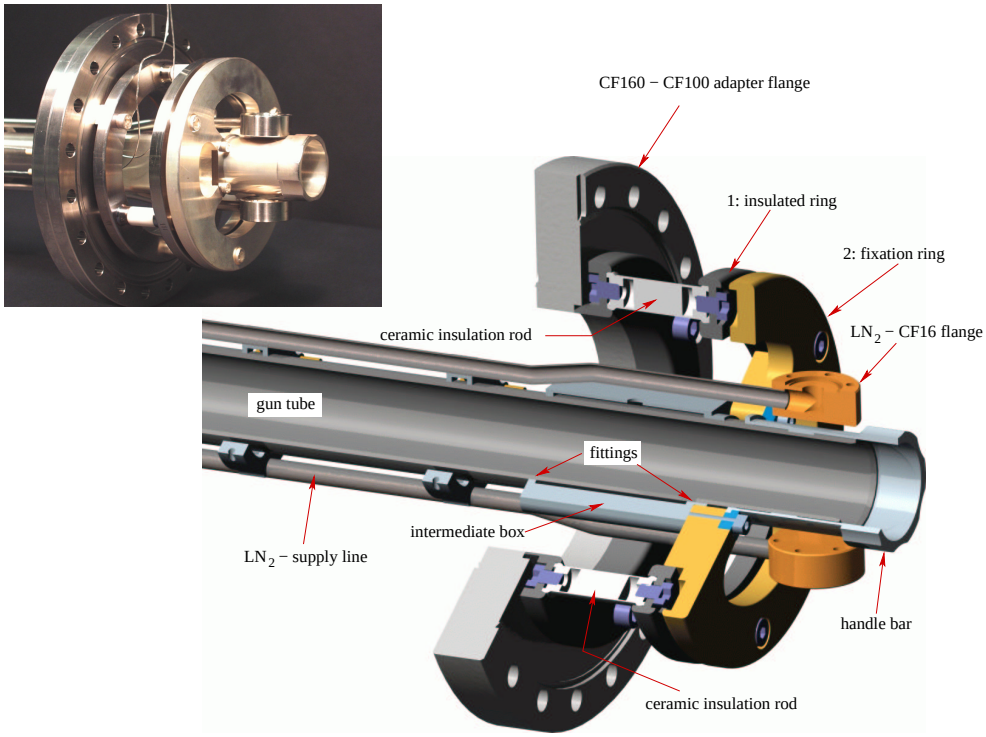

Fig. 5.8: *The electrical insulated mounting of the electron gun (120°-cut).*

get. In a cantilever mounting, the gun tube is electrically insulated by three ceramic rods (see Fig.5.8). A double ring attached to the ceramic insulators makes the joint to an intermediate box. Two fittings clamp the gun tube on each side of this box.

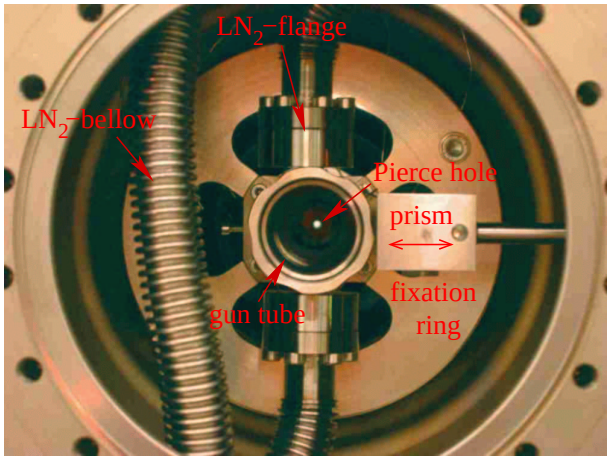

Fig. 5.9: *Rear view on the electron gun assembled in the gun chamber, after the first bakeout.*

The cathode distance on axis with respect to the flange can be adjusted with a handle bar pushing or pulling an outer fine thread on the gun tube through the intermediate box.
LN_2 flows through electrical insulated feedthroughs which are connected to CF16 flanges at the rear end of the LN_2-supply lines.

5.3 Thermal performance

In order to obtain the thermal performance of the new electron gun and the new cathode samples, several measurements were done under operating conditions. Since the new sapphire cathodes are of crucial importance in the thermal chain, a demanding production technology concerning the semiconductor-sapphire bonding was for the first time employed at Novosibirsk. According to the individual features of samples concerning surface properties and metallization, a certain variation of the produced sapphire cathodes also in their thermal properties can occur. In the first series, four sapphire photocathodes were successfully fabricated and the total thermal resistance of the electron gun, equipped with each of them and, for comparison, equipped with a reflection mode cathode, was evaluated.
Therefore, we measured the temperature rise in the GaAs bulk at several power steps of the laser which heated the samples. The employed photoluminescence spectroscopy probes the energy gap of GaAs and yields, especially at low temperature, pronounced spectra (see section 3.4.3). High precision in the order of $\pm$ 1 K for temperature changes is achieved up to $\Delta T \approx 50$ K. Using the start temperature (LN_2-cooled conditions, but without laser heating), estimated to be $T_S \lesssim 80$ K [Wei00] for our samples, the absolute operation temperature can be deduced for any applied laser power.

5.3.1 Total thermal resistance for the new sapphire cathodes

The total thermal resistance R_{tot} of the electron gun controls the temperature increase of the cathode in operation according to $\Delta T = R_{\text{tot}} \cdot \dot{Q}$, with $\dot{Q}$ denoting the absorbed power. Differences between *applied* and *absorbed* laser power at our wavelength are small and only weakly temperature-dependent, which allows us to refer this *linear* relation to the practically more useful applied power in accordance with the definition of the quantum efficiency as number of emitted electrons per number of *applied* photons.
For the relative temperature measurement, the new electron gun was assembled in the energy analyzer set-up complemented by the gun chamber (see upper Fig.5.10). By mounting windows at both ends, this linear temperature test set-up enabled easy optical access. The heating laser

with a profile presented in Fig.3.10 was shined in from behind and restricted to ϕ 3 mm by an aperture in the high pressure unit. For a calibration, laser light transmitted through this channel *without* photocathode was recorded by a powermeter placed on axis behind the chamber. The stability of the laser alignment was controlled during the temperature measurement with the small signal transmitted *through* the photocathode. The temperature was determined by photoluminescence (PL) spectroscopy from the front side of the cathode. A modulated red laser ($\lambda = 685$ nm, $f = 330$ Hz) probed the temperature in the cathode center with a spot size of $\approx \phi$ 0.8 mm at small intensity ($\approx$ 20 mW). Integrated PL-signals of the Si-diode behind the monochromator (see Fig.5.10 (a)) amounted to $\approx$ 1 nA. In this series, a force of 200 N was exerted on the sapphire-copper interface.

A typical heating curve obtained for sapphire cathode CR240.1.1/5* is presented in Fig.5.10 (b). First, a peak evaluation of several photoluminescence spectra after cooling down the sample ensured a stable start temperature ($\approx$ 80 K). The mean peak value was taken as reference ($\Delta T = 0$). Then, with each step of increased laser power, a new stabilization took place within about 30 min. Corresponding peak shifts yield ΔT to within $\pm$ 1 K. Typical accuracies for the power determination are in the order of $\pm$ 3%. The fitted straight line shows the linearity of the temperature increase with *applied* power, resulting in $R_{\mathrm{tot}} = (16.8 \pm 1.2)$ K/W. In case of reflection mode cathodes, the restriction to front illumination with a slightly reduced accuracy in the power determination results in an overall error of $\pm$ 4 K/W.

Table 5.3.1 summarizes the results for the first series of sapphire cathodes and, for comparison, a reflection mode cathode. The new electron gun provides with all four sapphire substrates

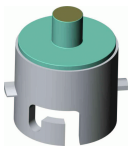

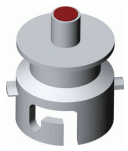

cathode	CR234.1.1/1*	CR234.1.2/5	CR240.1.1/5*	CR240.1.4/6*	reflection mode
resistance	(33.1 ± 1) K/W	(15.4 ± 1) K/W	(16.8 ± 1) K/W	(15.0 ± 2) K/W	(43 ± 4) K/W

a very high thermal conductance even though the first one shows with 33.1 K/W a higher resistance than the rest of the series. Three sapphire cathodes are equal within 15-17 K/W which is almost the range of accuracy. Since it is the first series of this type, it could be expected that the present bonding technique already yields a high percentage of photocathodes with a comparable good thermal performance. Studies on the first cathode, presented in the

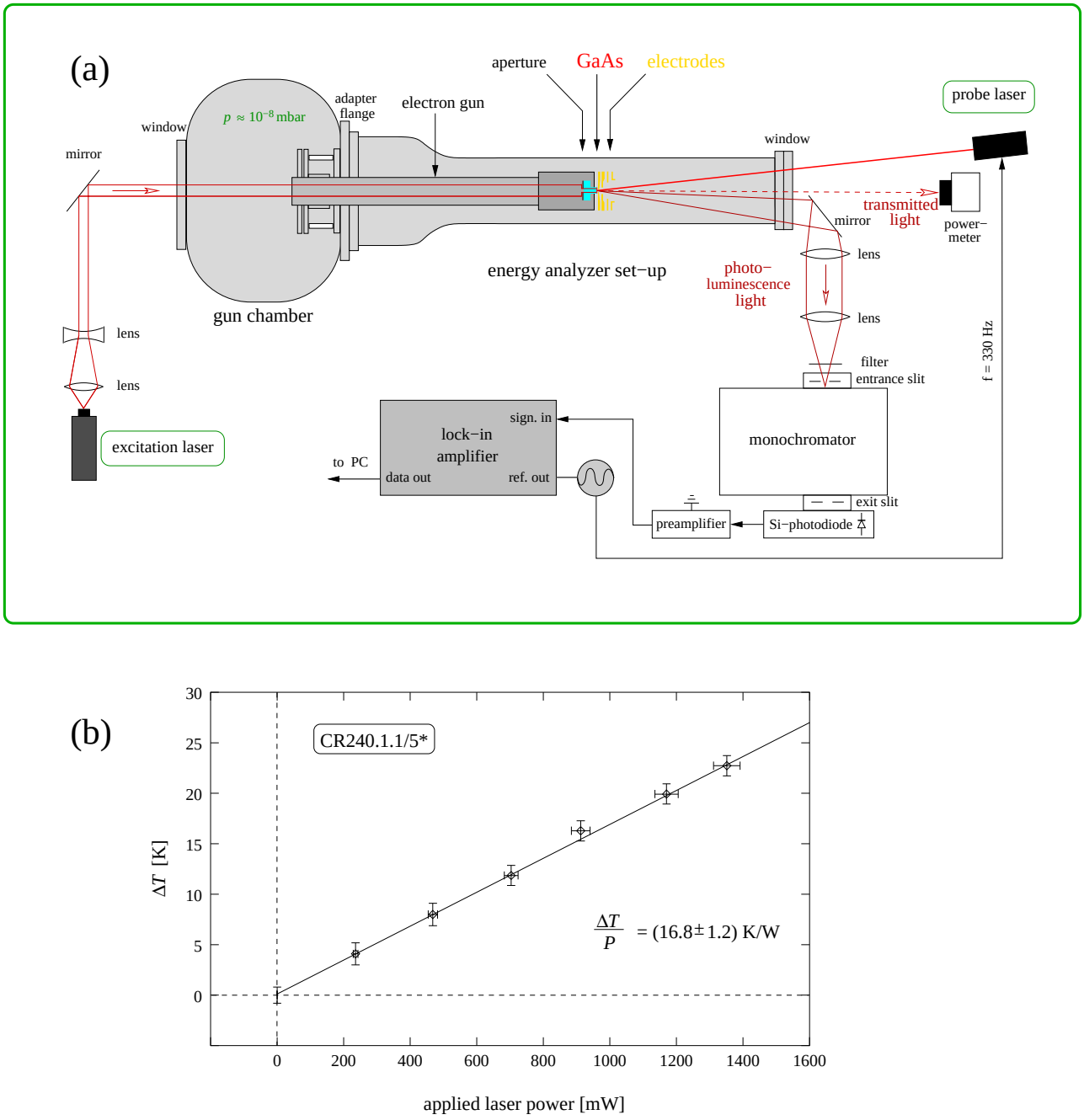

Fig. 5.10: *(a) Sketch of the in-line temperature test set-up and the measurement procedure. The excitation laser heated the sample in transmission geometry. Simultaneously a continuous flow of* LN_2 *supplied cooling. Photoluminescence based temperature determination was employed according to section 3.4.3. The pressure in the set-up ranged at* $\approx 10^{-8}$ mbar *in order to suppress cooling by an ambient atmosphere.*
(b) Heating curve exemplifying the measurement of R_{tot}*. The temperature change was determined by the peak shifts in the photoluminescence spectra.*

following section, will give hints which allow to attribute its higher thermal resistance to an increased heterostructure-sapphire interface resistance. The reflection mode cathode features a much lower thermal conductance. It is mainly caused by the reduced thermal conductivity of titanium in comparison to sapphire at low temperature accounting for $\approx$ 19 K/W. Nevertheless, the much easier production technology of the titanium reflection mode cathodes partly balances the disadvantages concerning the thermal properties and its restriction to front side illumination.

5.3.2 Investigations on the interface resistances in R_{tot}

The magnitude of the measured total resistances demonstrates that, besides the well known bulk elements in the thermal chain, there are strong interface contributions. According to their conductivity and geometry, all bulk elements together (copper, sapphire, AlGaAs and GaAs) account for $R_{\mathrm{bulk}} \lesssim 1$ K/W. The remaining difference with respect to the measured values will consequently be distributed among the different interface resistances.

Thus, R_{tot} *is largely governed by the interfaces.*

Specific thermal interface resistance is defined as $\Re = \frac{\Delta T}{\dot{Q}/A_c}$, with the steady-state difference ΔT between the surfaces and $\dot{Q}$ denoting the heat flow across the nominal area of contact A_c. Interfaces are highly sensitive to microscopic variations in the quality of the joint surfaces and the possible bonding. It could be expected that keeping up the major production conditions for the whole series does not necessarily guarantee an identical interface quality for all samples. Sapphire cathode CR234.1.1/1* features a total thermal resistance twice as high as the other cathodes of this type, which may be a sign for such a variation of interface conductance.
If we want to find out generally which are the limiting links in the conductance of the thermal chain, according to section 5.2.2.2 there are only the copper-sapphire and sapphire-AlGaAs interface which could account for the high measured R_{tot}. The following measurements will aim to distinguish these two relevant interfaces.
For cathode CR234.1.1/1* we performed a measurement with an aperture which reduces the heating laser power (see Fig.5.11). The temperature was determined *in the center* of the GaAs sample within a spot of the probe laser size ($\approx \phi$ 0.8 mm). Our standard hole limiting the heating laser (irradiating the sample from below in the figure) of ϕ 3 mm was reduced by insertion of an aperture to ϕ 1.5 mm. The measured temperatures and the heating laser power transmitted through the hole are given in Tab.5.1.

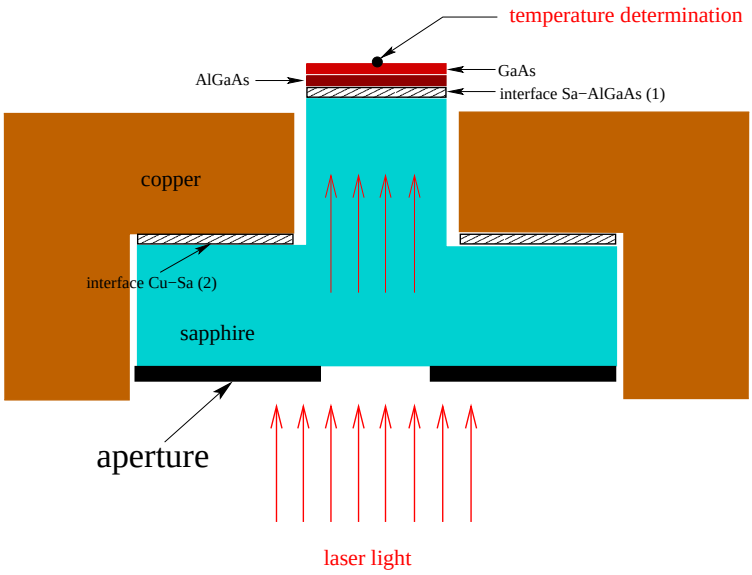

Fig. 5.11: *Heating measurement with inserted aperture to reduce the laser light.*

aperture	transmitted power	T_{GaAs}
ϕ 3 mm	1000 mW	(33.1 $\pm$ 1) K
ϕ 1.5 mm	410 mW	(29.9 $\pm$ 1) K

Tab. 5.1:

Basic idea in a simplified picture

A first discussion of the basic idea in a strongly simplified picture will result in a conclusion about the interface resistances. Afterwards, the influences of deviations from the idealized picture on the conclusion have to be estimated and reasonable values describing the real situation should be found. Finally, the two temperature measurements performed on cathode CR234.1.1/1* will allow to set an upper limit on the copper-sapphire interface and provide established information on the limiting link in our thermal chain.

In our picture, the following assumptions on the thermal bulk conductivity will be made:

a) $\lambda_{\mathrm{Sa}} = \infty$, c) $\dot{Q}^{\perp}{}_{\mathrm{AlGaAs}} = \dot{Q}^{\perp}{}_{\mathrm{GaAs}} = 0$ *in the plane of the semiconductor.*

b) $\lambda^{\parallel}{}_{\mathrm{AlGaAs}} = \lambda^{\parallel}{}_{\mathrm{GaAs}} = \infty$ *in the direction of the substrate axis,*

The extremely small layer thickness reduces strongly the lateral heat flow in the plane of the semiconductors. Assumption c) just expresses that we will neglect it for the present. Furtheron we will assume a box-like laser profile and a constant absorbed power density $\boldsymbol{\rho}_{\mathrm{abs}}$ in the illuminated GaAs-layer (and no absorption in any other layer).

Under these conditions, the temperature in the center of GaAs in such a serial connection of two interface resistors is given simply by the sum of the temperature drops at each interface:

$$T_{\mathrm{GaAs}} \quad = \quad T_{\mathrm{copper}} + \Delta T_{\mathrm{Sa-AlGaAs}} + \Delta T_{\mathrm{Cu-Sa}}. \tag{5.2}$$

We will denote the interfaces Sa-AlGaAs and Cu-Sa as interfaces 1 and 2, respectively. Let us regard the following situation of a measurement probing the temperature in the center of the cathode:

$$\Delta T_{\mathrm{Sa-AlGaAs}} = \Re_1 \cdot \boldsymbol{\rho}_{\mathrm{abs}} \qquad\qquad \Delta T_{\mathrm{Cu-Sa}} = \Re_2 \cdot \frac{\dot{Q}_2}{A_2} = \Re_2 \cdot \frac{\boldsymbol{\rho}_{\mathrm{abs}} \cdot A_{\mathrm{apt}}}{A_2} \tag{5.3}$$

with the aperture hole size A_{apt}, the heat flow $\dot{Q}_2$ across interface 2 and the area A_2 of interface 2. The heat load on interface 2 obviously changes, while the contribution of interface 1 remains constant. This is a consequence of assumption (a), since the infinite thermal conductivity of sapphire assures that all interface area contributes to the heat flow across interface 2. Two measurements for different apertures can yield the resistance $\Re_2$ from the temperature shift in T_{GaAs}. In short, the first interface temperature drop depends directly on the absorbed power density $\boldsymbol{\rho}_{\mathbf{abs}}$ and the second one, in contrast, is determined by the **total power** going through the sample.

Deviations from the idealized picture

The assumption for the semiconductor conductivity of negligible thermal flow in the plane of the layer (c) but free flow in the axial direction (b) would change for small $\dot{Q}^{\perp}$ and finite $\lambda^{\parallel}$ in a way that some heat originating from an illuminated area of GaAs flows in the lateral direction of the layers and heats up the surrounding material. In order to set an upper limit on this effect, we will estimate lateral heating effects in the GaAs-layer with a temperature simulation. It will also allow to give a maximum gradient in the sapphire substrate attributed to its high, but finite thermal conductivity.

We will base the *temperature simulation for lateral heating effects* in the GaAs-layer on the measured total thermal resistance of cathode CR234.1.1/1* and compare two measurements with our standard aperture (ϕ 3 mm) and the small aperture (ϕ 1.5 mm). The difference between both cases consists of an illuminated and thus heated ring of GaAs between radius 0.75 mm and 1.5 mm. Our aim of the simulation is to give an upper limit for the temperature increase in the center of the cathode (where temperature is measured) due to heating of this ring and our assumption is that both interfaces result together in the measured $R_{\mathrm{tot}} = 33.1$ K/W. Assigning all resistance to interface 1, we will get a conservative estimation since the lateral heat flow is most in this case. The opposite case of a R_{tot}-assignment to interface 2 would cause the

sapphire to heat up but the temperature gradient in the GaAs-layer will take a minimal value. So we will model our photocathode and the copper cooler with the given geometrical sizes and take the interfaces into account by resistances 33.1 K/W at interface 1 and no resistance at interface 2. The temperature simulation module of Mafia 3 was used [Maf94].

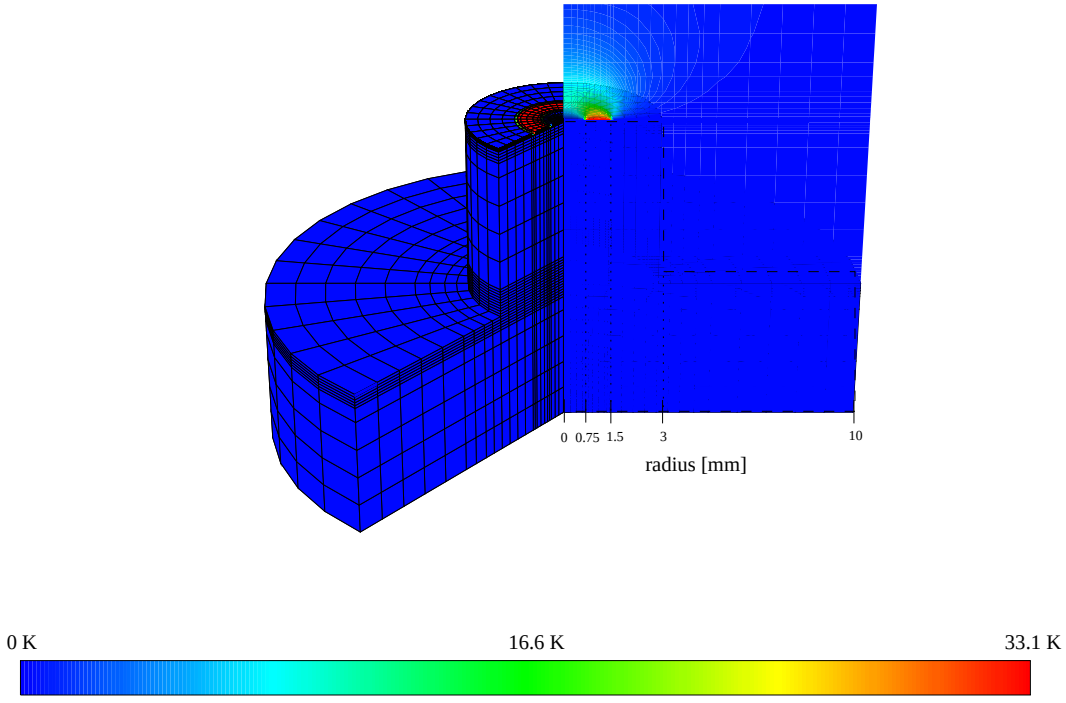

Fig. 5.12: *Temperature distribution in a* 120°*-cut color illustration. A GaAs ring was set to 33.1* K *and the outer copper cooling head to 0* K*. The cooling head, included in the simulation, is suppressed in the picture.*

The remaining free parameter, the thickness of interface 1, was set to a typical layer size, i.e. 2 μm. Temperatures were assigned to the heated GaAs ring (33.1 K) and the outer copper body ($T_{\mathrm{start}} = 0$ K). The simulation comprises the heated GaAs-ring (d = 2μm, 0.75 mm < r $\leq$ 1.5 mm) and the non-heated rest of the GaAs-layer (d = 2μm, r $\leq$ 0.75 mm and 1.5 mm < r $\leq$ 3 mm, $\lambda_{\mathrm{GaAs}} = 300$ W/m·K), AlGaAs (d = 2μm, r $\leq$ 3 mm, $\lambda_{\mathrm{AlGaAs}} = 100$ W/m·K), sapphire ($\lambda_{\mathrm{Sa}} = 800$ W/m·K) and the copper cooling head ($\lambda_{\mathrm{Cu}} = 600$ W/m·K). Plot 5.12 shows the result of the simulation in the temperature color code illustration (the copper cooling head was hidden in the picture for a better clearness). For the extrapolated residual gas conductivity, a value of 10^{-8} mbar was assumed. An enlarged picture of the GaAs ring border is shown in Fig.5.13.

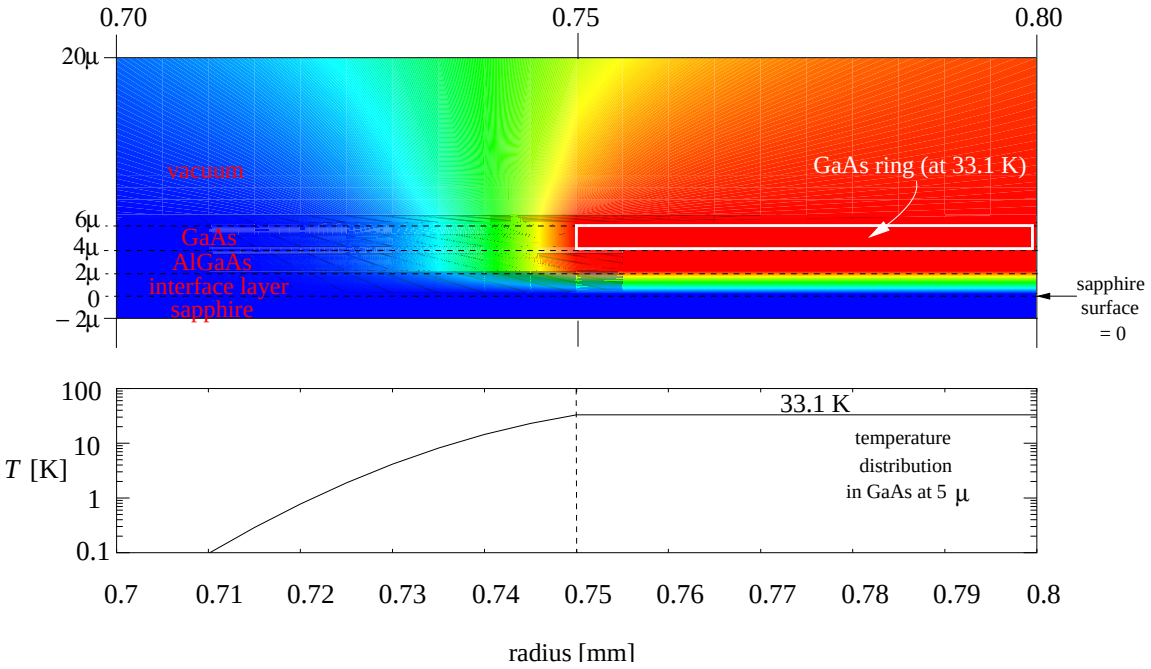

Fig. 5.13: *Magnification of the cut-plain in plot 5.12. The region is chosen to show the situation directly at the inner radius of the heated GaAs ring. The calculated temperatures in the plain of the GaAs-layer at $z = 5\mu$ are plotted below.*

The temperature strongly decreases with smaller radii and, as seen in the plot, it falls below 0.1 K already at r = 0.71 mm corresponding to ϕ 1.42 mm. The laser spot probing the temperature in the center of the cathode has a diameter of 0.8 mm. A measurable influence on the probed temperature in the cathode center due to lateral heat flow in the plain of the GaAs-layer is accordingly not expected from the heated ring.

A second simulation aiming to set an upper limit on temperature gradients in the sapphire and the **axial** direction of the semiconductor layers ensured *small* influences which were together below 0.2 K. In total, our assumptions given in the beginning of this section are fulfilled good enough to justify the conclusions within the range of accuracy for the temperature determination by photoluminescence. The assumption of a box like laser profile simplified the consideration but was not essential for the conclusion as long as it does not change during the measurements. According to our laser (see Fig.3.10) we can easily account for that by measuring the laser power transmitted through the aperture.

Comparison of T_{GaAs} for two apertures

According to Tab.5.1, a power difference of 590 mW, absorbed in the ring between ϕ 1.5 mm

and ϕ 3 mm, increased T_{GaAs} by 3.2 K in the first case. This results in a contribution of the interface *sapphire-copper* to the total thermal resistance of: (5.4 ± 1.4) K/W.
Referred to the area of contact the interface resistance amounts to $\Re_{\mathrm{Cu-Sa}} \approx 1.5 \cdot 10^{-3} \frac{\mathrm{K \cdot m^2}}{\mathrm{W}}$. This value is only a factor 3 smaller than polished copper-copper contacts under the same pressure [Ber56] which are assumed to make very good dry contacts and considerably better than stainless steel contacts [Gme99].

The results show a smaller resistance at interface 2 and demonstrate evidently a *dominating* influence of the remaining sapphire-AlGaAs interface to R_{tot} in the order of 28 K/W in case of cathode CR234.1.1/1* . This corresponds to $\Re_{\mathrm{Sa-AlGaAs}} \approx 2 \cdot 10^{-4} \frac{\mathrm{K \cdot m^2}}{\mathrm{W}}$. Assuming similar conditions for the copper-sapphire interfaces for all photocathodes of the series, it can be concluded that heating is dominated by the bonding of sapphire to the semiconductor and governed mainly by the applied *laser power density* according to the left equation in (5.3).

5.3.3 Force dependence of $R_{\mathrm{Cu-Sa}}$

The general behavior of contact resistances under load described in chapter 2 exhibits a broad range of linearity given by the correspondence: *higher forces on the interface results in lower resistances*. Nevertheless, at very high forces, depending on the individual properties of the interface, saturation takes place. After insertion into the gun, our sapphire substrate is pressed with a spring to the copper cooling head to enhance the interface conductance. In order to find out whether we are in the linear regime and could basically decrease the copper-sapphire interface resistance further or this effect saturated already, several spring load measurements were performed with the standard aperture (see Diagram 5.14). The standard spring used in the previous measurements exerted a force of 200 N. As seen from the diagram, a force variation from 100 N 300 N did not change the resistance significantly.

This almost invariant behavior is a sign of saturation above 100 N. Basically, springs between 100 N and 300 N could be used with similar result. Since a certain variation over different cathodes could not absolutely be excluded, a force value not too close to the strong resistance increase at lower force is recommended. Saturation seems to start between 20 N and 100 N for our contact. Literature values reported a saturation setting in at about 30 N for polished copper and stainless steel contacts at room temperature [Gme99]. For low forces, the expected increase of the thermal resistance was observed. In contrast to clearly defined and reproducible values in the saturation region, strong variations for different measurements were obtained at 10 N and 20 N. The outermost measured points are shown in the plot in these two cases. Compared to the small contribution of this interface at higher loads (≈ 5 K/W), it became in the low load region evidently very poor (≈ 12 K/W at 20 N, ≈ 37 K/W at 10 N). Especially the

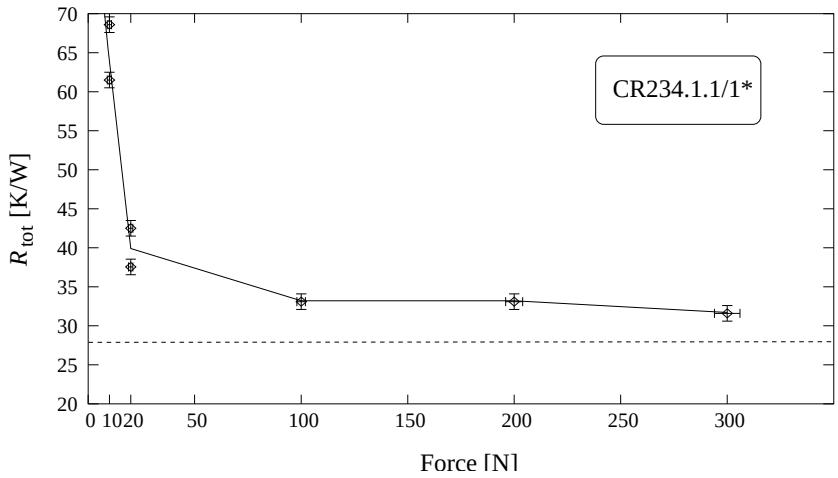

Fig. 5.14: *Measured total resistances in dependence of the spring force exerted on the copper-sapphire interface. A polygon line was added to guide the eye. It goes through the mean values for 10* N *and 20* N*. The contribution of the first interface (*Sa-AlGaAs*) reported in the previous section is indicated with a dashed line (≈ 28* K/W*).*

spread of points is a sign that in addition to the expected linear increase the surfaces seem to touch imperfectly since the difference clearly exceeds the error bars. A reason for poor contact could be a slight angular misalignment during the insertion of the cathode which occurs only at small spring forces. Friction with the cooling head thus can lead to imperfect positioning and is supposably overcome reliably only at higher forces.
Cycling loading measurements (≈ 20 insertions) at 200 N revealed no abrasion effects in a measurable degree.

5.4 Photocathode set-up at the electron target

The photocathode set-up is mounted on a frame independently of the target support. Fig.5.15 shows a view on the gun chamber and the new electron gun as they will be installed in operation position at the electron target.

The self-supporting construction allows the photocathode electron gun to be inserted from behind to the tube in the center of the superconducting magnet. Longitudinal positioning of the cathode in the magnetic field maximum is found by moving the entire photocathode set-up along the target axis. The adapter flange keeping the electron gun (see also Fig.5.8) is fixed at one side at the gun chamber and will serve for mounting of the interconnection tube to the CF100-bellow of the target set-up.

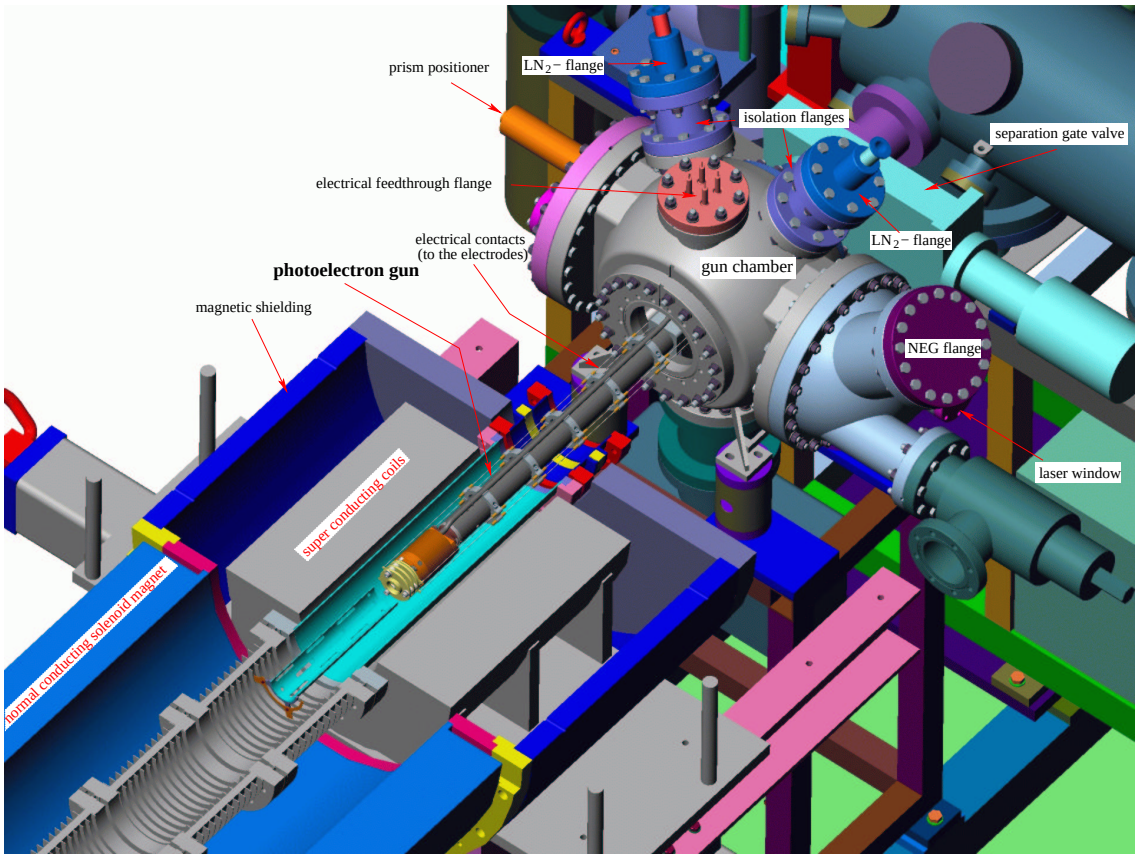

Fig. 5.15: *Photocathode set-up installed at the electron target.*
View on the new electron gun, the gun chamber as well as on a 180°*-cut of the superconducting magnet of the target.*

Alternatively a connection to the pumping chamber of the optional thermionic operation can be done (see [Spr03]).

Electrical contacts of the electrodes and the pierce shield are guided along the gun tube and can be accessed via the feedthroughs on top of the gun chamber. The cathode potential is applied to the electrically insulated LN_2-feedthroughs.

At the cut view of the electron target, the vacuum tube (ϕ 100mm) is surrounded by superconducting magnetic coils. A massive iron enclosure serves as magnetic shielding. Downstream, a normal-conducting solenoid magnet provides the magnetic guiding of the electron beam.

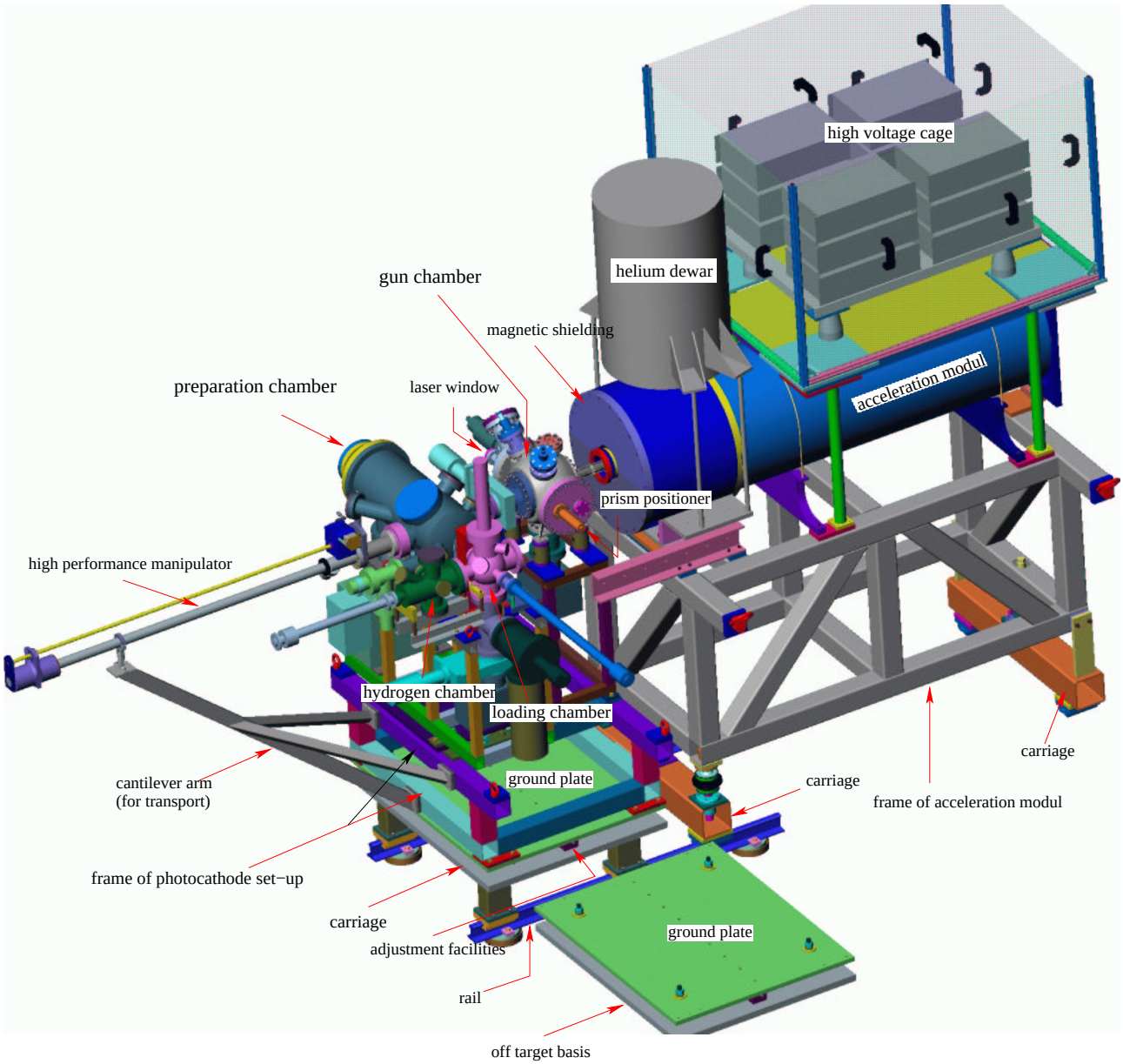

Fig. 5.16: *Lateral view on the modular target design.*

The gun chamber can be separated from the rest of the photocathode set-up by a valve to the preparation chamber and is equipped with an ion getter pump (star cell 60 l/s) and a NEG module (880 l/s). Pumping facilities in the near cathode region are NEG stripes along the beamline.

A lateral view on the complete photocathode set-up shows the modular construction of the electron target section (see Fig.5.16). It is kept in a frame assembled on carriages and shares the rails with the photocathode module [Spr03]. A precise positioning of the entire photocathode set-up construction is provided by adjustment facilities between a ground plate and its carriage. A second basis outside the electron target was built to enable further measurements at the energy analyzer set-up (not shown in the figure). This flexible solution allows easy two-way operation of our photoelectron gun and the thermionic electron gun.

For the operation of photocathodes, the long, high performance manipulator transfers the GaAs(Cs,O) cathode from the preparation chamber through the gun chamber and inserts it into the cooling head of the electron gun. After the manipulator head is drawn back, the lateral positioner in the gun chamber moves a prism on electron gun axis. The excitation laser can be shined in via a window perpendicular to the axis and is deflected by a mirror to illuminate the photocathode in transmission. During the operation of the photocathode, a new sample can be prepared and kept in reserve. Replacements of cathodes are usually done within a few minutes and a "quasi-continuous" electron beam operation is maintained.
In the present status of the photocathode set-up, the cryo-photoelectron gun, the newly built internals of the preparation chamber, loading/hydrogen chamber required to fit the sapphire/holder construction, as well as the manipulator guidance have been built and assembled. Test bakeouts were performed with the preparation chamber, gun chamber and loading/hydrogen chamber. The new support module was constructed and is presently built.

6. Conclusion and Outlook

This thesis reports the realization of an intense photoelectron gun based on GaAs(Cs,O) with a narrow energy distribution providing an electron source for the electron target set-up at the Heidelberg Test Storage Ring TSR.

It was demonstrated with photocathodes of reproducible high quantum efficiencies (QE_{tot} = 20-28%) that by cutting the photoelectron distribution below the conduction band minimum in the GaAs bulk and extracting only electrons with longitudinal energies above E_{cbm}, thermalized electron distributions with energy spreads of $\approx k_{\mathrm{B}}T_{\mathrm{bulk}}$ are obtained. In contrast to an increase of the mean transverse energy (MTE) for all emitted photoelectrons at low temperature ($T \approx$ 100 K) from 59 meV to 66 meV compared to room temperature, energy spreads of longitudinally 12 meV and transversely 6 meV were obtained for electrons above E_{cbm}. The reason for higher MTE is the emission of electrons with lower longitudinal energy but higher transverse energy due to a lowered vacuum level at 100 K. In order to produce cold electrons, the beam can be restricted to the cold part of the electrons with longitudinal energies above E_{cbm}. Yields for these electrons of $QE_{\mathrm{eff}} \approx 1\%$ were achieved. Cutting below E_{cbm} allows even to increase the yield with only slightly enhanced transverse energy spreads.

Activations with different layer thicknesses were tested quantitatively and a thickness of 0.5-0.7 monolayers of Cs-coverage proved to enhance QE_{eff} compared to the commonly used activations to maximum quantum efficiency at 1.5-1.7 monolayers, due to decreasing transmission of the semiconductor-vacuum interface with increasing layer thickness. It was found that QE_{eff} can be strongly enhanced by 30-50% with layer thicknesses of 0.7 monolayers Cs-coverage.

In order to produce a cold electron beam of a few milliamperes current at these effective quantum efficiencies, high laser illumination of about 1 W has to be applied. A main problem under these operation conditions is strong cathode heating. A new cryo-electron gun for high currents, including new sapphire substrate photocathodes, was constructed and built, considering in particular low temperature stabilization under high laser illumination. Thermal performance measurements showed indeed temperatures of $\approx$ 95 K at 1 W laser power. The known fitted e^{-1}-lifetime of the photocathode at milliampere electron currents, as measured in the gun chamber of the photocathode set-up under comparable vacuum conditions but better geometrical

configuration than in the ETS with respect to high energy ion backflow (a main reason for degradation), amounts to 10 hours.

The present parameters of cathode performance indicate an adequate result in order to achieve cold and intense electron beams with the GaAs photocathode electron gun after installation into the ETS. The implementation and successful application of the atomic hydrogen cleaning technique to our cathode preparation will enable us to operate the photocathode electron gun for a few months without opening the photocathode set-up to atmosphere.

Under application of adiabatic acceleration and adiabatic transverse expansion of the electron beam at the ETS, the operation of the GaAs(Cs,O) photocathode electron gun will make transverse electron temperatures down to $k_{\mathrm{B}}T_{\perp} < 1$ meV accessible, given by the initial transverse temperature $k_{\mathrm{B}}T_{\perp}^{i} \approx 8$ meV and an adiabatic transverse expansion by $\alpha \leq 1/8$ (transverse temperature decrease by ATE see p.15). In addition, the use of the photocathode allows to decrease strongly the first term in eqn.(2.17), which is especially important at low beam energies in atomic and molecular collision experiments.

With completion of its support module, the photocathode set-up will be installed soon into the electron target set-up. A dielectronic recombination resonance in lithium-like fluorine $^{19}\mathrm{F}^{6+}$ is planned to be used to determine the longitudinal and transverse electron temperature.

Appendix

A Transverse emittance

An important figure of merit for estimation of electron beam quality is the transverse emittance $\boldsymbol{\epsilon}$, signifying basically the product of beam width and the transverse velocity spread. In case of rotational symmetry along the z-axis, as it is given for the photocathode, the full information on the emittance is reduced to a single transverse component $\boldsymbol{\epsilon_x}$ and we will consider the $x-z$ plane. The divergence of the beam is associated with the slope of electron trajectories $x' = dx/dz = \dot{x}/\dot{z}$. At a given distance along the beam axis, every electron represents a point in the trace space $x - x'$. All particles in the beam occupy an area in the trace space

$$A_x \;=\; \int\int \; dx \; dx', \tag{A.1}$$

which is related to the emittance. In the literature, there is no consistancy between different authors concerning the emittance and the implicit or explicit use of the factor π. Since we are interested in the beam quality, we will adopt a definition which is closely connected to it even for nonlinear beam optics. Based on the second moments of the spacial and velocity distribution the *effective* emittance as given by [Rei94] is:

$$\boldsymbol{\epsilon_x} = \; 4 \; \tilde{x} \; \cdot \; \tilde{x}'_{\rm th} \;=\; 4 \; \tilde{x} \; \cdot \; \frac{\tilde{v}'_{\rm th}}{v_0}, \quad [\mathrm{mm-mrad}] \tag{A.2}$$

where $\tilde{x} = (\overline{x^2})^{1/2}$ is the rms width, $\tilde{x}'_{\rm th} = (\overline{x'^2})^{1/2}$ the x-component of the *random* or *thermal* rms divergence, $\tilde{v}'_{x,\rm th} = (\overline{v^2})^{1/2}$ the rms velocity spread, and v_0 the mean axial velocity of the electron distribution. In linear beam optics, this quantity can be referred to A_x by

$$\boldsymbol{\epsilon_x} \;=\; \frac{A_x}{\pi} \quad .$$

Calculation of the emittance for our beam of photoemitted electrons requires the determination of $\tilde{x}$ and $\tilde{v}'_{\rm th}$. To good approximation, the spacial density profile of the beam can be described with constant intensity n_0 inside the beam ($\phi = 3$ mm) and negligibly small intensity outside (see section 5.2.1).

$$\tilde{x} \;=\; \frac{(\overline{r^2})^{1/2}}{\sqrt{2}} = \frac{1}{\sqrt{2}} \left(\frac{2\pi n_0 \int_0^{d/2} r^3 dr}{2\pi n_0 \int_0^{d/2} r dr} \right)^{1/2} = \frac{d}{4}$$

For a thermal velocity spread according to a Gaussian distribution of the form $\exp[-m(v_x^2 + v_y^2)/2k_{\rm B}T_\perp]$ results in

$$\tilde{v}'_{x,\rm th} \;=\; \frac{(\overline{v_\perp^2})^{1/2}}{\sqrt{2}} \;=\; \Big(\frac{k_B T_\perp}{m}\Big)^{1/2}$$

Such a beam has an emittance

$$\boldsymbol{\epsilon_x} = d\Big(\frac{k_\mathrm{B}T_\perp}{mv_0^2}\Big)^{1/2}. \tag{A.3}$$

At typical energies in the electron target (2 keV) and for a photocathode at room temperature ($k_\mathrm{B}T_\perp = 25$ meV), the transverse emittance amounts to ≈ 10.6 mm-mrad. Since the emittance is inversly proportional to the axial velocity, it it desirable for an independent comparison of beams at different energies to get a normalized measure. The *normalized effective* emittance defined by $\boldsymbol{\epsilon_{x,n}} = \beta\gamma\ \boldsymbol{\epsilon_x}$ $(\beta = v_0/c,\ \gamma = (1 - \frac{{v_0}^2}{c^2})^{-1/2})$, eliminates the velocity dependence,

$$\boldsymbol{\epsilon_{x,n}} = d\Big(\frac{k_\mathrm{B}T_\perp}{mc^2}\Big)^{1/2} \qquad (\gamma \approx 1). \tag{A.4}$$

Under LN_2 cooling of the photocathode this value amounts to

$$\boldsymbol{\epsilon_{x,n}} = 0.33 \text{ mm-mrad}.$$

Typical reported values for free electron laser RF guns amount to 0.5-1 mm-mrad [Bri01]. Linac injector RF guns are typically ≥ 2 mm-mrad [Bro01, All99].

Bibliography

[Ada85] Adachi S., *GaAs, AlAs, and Al_xGa_{1-x}: Material parameters for use in research and device application*, J. Appl. Phys. **58** (1985), 1.

[Ada00] Adamcyk M., Pinnington T., Ballestad A., Tiedje T., *Effect of the starting surface on the morphology of MBE-grown GaAs*, Mater. Sci. Eng. B **75** (2000), 153.

[All99] Alley R., Bharadwaj V., Clendenin J., Emma P., Fisher A., Frisch J., Kotseroglou T., Miller R.H., Palmer D.T., Schmerge J. *et al.*, *The design for the LCLS RF photoinjector*, Nucl. Instr. Meth. A **429** (1999), 324.

[Alp94] Alperovich V.L., Paulish A.G., Terekhov A.S., *Domination of adatom-induced over defect-induced surface states on p-type GaAs(Cs,O) at room temperature*, Phys. Rev. B **50** (1994), 5480.

[Alp95a] Alperovich V.L., Paulish A.G., Scheibler H.E., Terekhov A.S., *Evolution of electronic properties at the p-GaAs(Cs,O) surface during negative electron affinity state formation*, Appl. Phys. Lett. **66** (1995), 2122.

[Alp95b] Alperovich V.L., Paulish A.G., Terekhov A.S., *Unpinned behavior of the electronic properties of a p-GaAs(Cs,O) surface at room temperature*, Surf. Sci. **331-333, Part 2** (1995), 1250.

[Ant75] Antypas G.A., Edgecumbe J., *Glass-sealed GaAs-AlGaAs transmission photocathode*, Appl. Phys. Lett. **26** (1975), 371.

[Bel73] Bell R.L., *Negative Electron Affinity Devices*, Clarendon, Oxford, 1973.

[Ber56] Berman R., *Some experiments on thermal contact at low temperatures*, J. Appl. Phys. **27** (1956), 318.

[Bis93] Bischler U., Bertel E., *Simple source of atomic hydrogen for ultrahigh vacuum applications*, J. Vac. Sci. Technol. **11** (1993), 458.

[Bon98] Bond P., Brier P.N., Fletcher J., Jia W.J., Price H., Gorry P.A., *Reactive scattering study of etching dynamics: Cl_2 on GaAs(100)*, Surf. Sci. **418** (1998), 181.

[Bri01] Brinkmann R., Derbenev Y., Flöttmann K., *A low emittance, flat-beam electron source for linear colliders*, Phys. Rev. Spec. Top. - Acc. and Beams **4** (2001), 053501.

[Bro01] Brown W. J., Korbly S.E., Kreischer K.E., Mastovsky I., Temkin R.J., *A low emittance electron beam formation with a 17 GHz RF gun*, Phys. Rev. Spec. Top. - Acc. and Beams **4** (2001), 083501.

[Bur78] Burt M.G., Heine V., *The theory of the workfunction of caesium suboxides and caesium films*, J. Phys. C: Solid State Phys. **11** (1978), 961.

[Cic91] Ciccacci F., Chiaia G., *Comparative study of the preparation of negative electron affinity GaAs photocathodes with O_2 and with NF_3*, J. Vac. Sci. Technol. A **9** (1991), 2991.

[Dro85] Drouhin H.-J., Hermann C., Lampel G., *Photoemission from activated gallium arsenide: I. Very-high-resolution energy distribution curves*, Phys. Rev. B **31** (1985), 3859.

[Dun95] Dunham B.M., Cardman L.S., Sinclair C.K., , Particle Accelerator Conference (Dallas), 1995.

[Ebe99] Ebert Ph., Zhang T., Kluge F., Simon M., Zhang Z., Urban K., *Importance of Many-Body Effects in the Clustering of Charged Zn Dopant Atoms in GaAs*, Phys. Rev. Lett. **83** (1999), 757.

[Eib98] Eibl C., Lackner G., Winkler A., *Quantitative characterization of a highly effective atomic doser*, J. Vac. Sci. Technol. A **16** (1998), 2979.

[Ela98] Elamrawi K.A., Elsayed-Ali H.E., *GaAs photocathode cleaning by atomic hydrogen from a plasma source*, J. Phys. D: Appl. Phys. **32** (1998), 251.

[Fis72] Fisher D.G., Enstrom R.E., Escher J.S., Williams B.F., *Photoelectron surface escape probability of (Ga,In)As:Cs-O in the 0.9 to $\approx$ 1.6 μm range*, J. Appl. Phys. **43** (1972), 3815.

[Gme99] Gmelin E., Asen-Palmer M., Reuther M., Villar R., *Thermal boundary resistance of mechanical contacts between solids at sub-ambient temperatures*, J. Phys. D: Appl. Phys. **32** (1999), R 19.

[Got95] Goto S., Yamada M., Nomura Y., *Surface Cleaning of Si-Doped/Undoped GaAs Substrates*, Jpn. J. Appl. Phys. **34** (1995), L 1180.

[Gui96] Guidi V., *Anomalous broadening of energy distributions in photoemitted electron beams*, J. Appl. Phys. **79** (1996), 8187.

[Hal95] Hallin C., Bergman J.P., Janzen E., *High temperature optical properties of GaAs/AlGaAs double heterostructures*, Semicond. Sci. Technol. **10** (1995), 841.

[Her96] Herrera-Gómez A., Vergara G., Spicer W.E., *Physics of high-intensity nanosecond electron source: Charge limit phenomenon in GaAs photocathodes*, J. Appl. Phys **79** (1996), 7318.

[Hop01] Hoppe M., *Differential energy analysis of electron beam: A study of photoemission from NEA-GaAs*, Ph.D. thesis, Universität Heidelberg, 2001.

[Ide94] Ide Y., Yamada M., *Role of Ga_2O in the removal of GaAs surface oxides induced by atomic hydrogen*, J. Vac. Sci. Technol. A **12** (1994), 1858.

[Jac98] Jackson J.D., *Classical electrodynamics*, John Wiley & Sons, New York, 1998.

[Jan90] Jansen G.H., *Coulomb Interactions in Particle Beams*, Adv. in Electronics and Electron Physics, Suppl. 21, Acedemic Press, Boston, 1990.

[Jar97] Jaroshevich A.S., Kirillov M.A., Orlov D.A., Paulish A.G., Scheibler H.E., Terekhov A.S., *Photocurrent saturation at GaAs(Cs,O)*, Proc. of the 7th Intl. Workshop on Polarized Gas Targets and Polarized Beams, AIP Conference Proceedings 421 (Urbana), 1997.

[Kam91] Kamaratos M., Bauer E., *Interaction of Cs with the GaAs(100) surface*, J. Appl. Phys. **70** (1991), 7565.

[Kan97] Kang M.-G., Sa S.-H., Park H.-H., Suh K.-S., Oh K.-H., *The characterization of etched GaAs surface with HCl or H_3PO_4 solutions*, Thin Solid Films **308-309** (1997), 634.

[Kar97] Karpov S.Yu., Maiorov M.A., *Model of the adsorption/desorption kinetics on a growing III-V compound surface*, Surf. Sci. **393** (1997), 108.

[Kir83] Kirschner J., Oepen H.P., Ibach H., *Energy- and Spin-Analysis of Polarized Photoelectrons From NEA GaAsP*, Appl. Phys. A **30** (1983), 177.

[Kra92] Krause P., *Temperaturrelaxation in magnetisierten Elektronenstrahlen*, Ph.D. thesis, Universität Heidelberg, 1992.

[Kud82] Kudelainen V.I., Lebedev V.A., Meshkov I.N., Parkomchuk V.V., Sukhina B.N., *Temperature relaxation in a magnetized electron beam*, JETP **56** (1982), 1191.

[Kur95] Kurihara Y., Omori T., Takeuchi Y., Yoshioka R., Nakanishi T., Okumi S., Tawada M., Togawa K., Tsubata M., Baba T., Mizuta M., Alley R.K., Aoyagi H., Clendenin J.E., Frisch J.C., Mulhollan G.A., Saez P.J., Schultz D.C., Tang H., Witte K.H., *A high polarization and high quantum efficiency photocathode using a GaAs-AlGaAs superlattice*, Jpn. J. Appl. Phys. **34, Part 1** (1995), 355.

[Maf94] Mafia V320.1, *Static Solver*, 1994.

[Mil73] Milnes A.G., *Deep impurities in semiconductors*, John Wiley & Sons, New York, 1973.

[Ole80] Olego D., Cardona M., *Photoluminescence in heavily doped GaAs. 1. Temperature and hole-concentration dependence*, Phys. Rev. B **22** (1980), 886.

[O'N85] O'Neil T.M., Hjorth P.G., *Collisional dynamics of a strongly magnetized pure electron plasma*, Phys. Fluids **28** (1985), 3241.

[Orl00] Orlov D.A., Andreev V.E., Terekhov A.S., *Elastic and Inelastic Tunneling of Photoelectrons from the Dimensional Quantization band at a p^+-GaAs(Cs,O) Interface into Vacuum*, JETP Lett. **71** (2000), 151.

[Orl01a] Orlov D.A., Hoppe M., Weigel U., Schwalm D., Terekhov A.S. and Wolf A., *Energy distributions of electrons emitted from GaAs(Cs,O)*, Appl. Phys. Lett. **78** (2001), 2721.

[Orl01b] Orlov D.A., Weigel U., Hoppe M., Schwalm D., Terekhov A.S., Wolf A., *Cold Electrons from GaAs(Cs,O)*, Proc. of the 7th Intl. Workshop on Polarized Sources and Targets (Nashville), 2001.

[Orl03] Orlov D.A., Weigel U., Hoppe M., Schwalm D., Jaroshevich A.S., Terekhov A.S., Wolf A., *Cold Electrons from Cryogenic GaAs Photocathodes: Energetic and Angular Distribution*, Hyperfine interactions (2003), to be published.

[Pas96] Pastuszka S., Terekhov A.S., Wolf A., *'Stable to unstable' transition in the (Cs,O) activation layer on GaAs(100) surfaces with negative electron affinity in extremly high vacuum*, Appl. Surf. Sci. **99** (1996), 361.

[Pas97] Pastuszka S., *Erzeugung kalter Elektronenstrahlen durch Photoemission aus GaAs*, Ph.D. thesis, Universität Heidelberg, 1997.

[Pas00] Pastuszka S., Hoppe M, Kratzmann D., Schwalm D., Wolf A., Jaroshevich A.S., Kosolobov S.N., Orlov D.A., Terekhov A.S., *Preparation and Performance of transmission-mode GaAs photocathodes as sources for cold dc electron beams*, J. Appl. Phys. **88** (2000), 6788.

[Pet92] Petit E.J., Houzay F., Moison J.M., *Interaction of atomic hydrogen with native oxides on GaAs(100)*, J. Vac. Sci. Technol. A **10** (1992), 2172.

[Pet97] Petit E.J., Huozay F., *Optimal surface cleaning of GaAs(001) with atomic hydrogen*, J. Vac. Sci. Technol. B **12** (1997), 547.

[Pie80] Pierce D.T., Celotta R.J., Wang G.-C., Unertl W.N., Galejs A., Kutatt C.E., Mielczarek S.R., *GaAs spin polarized electron source*, Rev. Sci. Instrum. **51** (1980), 478.

[Pob96] Pobell F., *Matter and Methods at Low Temperatures*, Springer, Berlin, 1996.

[Rei94] Reiser M., *Theory and Design of Charged Particle Beams*, John Wiley & Sons, New York, 1994.

[Rod86] Rodway D.C., Allenson M.B., *In situ surface study of the actvation layer on GaAs(Cs,O) photocathodes*, J. Phys. D: Appl. Phys. **19** (1986), 1353.

[Rou93] Rouleau C.M., Park R.M., *GaAs substrate cleaning for epitaxy using a remotely generated atomic hydrogen beam*, J. Appl. Phys. **73** (1993), 4610.

[Rud03] Rudolph P., *Non-stoichiometry related defects at the melt growth of semiconductor compound crystals - a review*, Cryst. Res. Technol. **38** (2003), 542.

[Sai90] Saito J., Kondo K., *Effects of etching with a mixture of HCl gas and H_2 on the GaAs surface cleaning in molecular-beam epitaxy*, J. Appl. Phys. **67** (1990), 6274.

[San94] Santos E.J.P., MacDonald N.C., *Selective emission of electrons from patterned negative electron affinity cathodes*, IEEE Trans. Electron Devices **41** (1994), 607.

[Sch65] Scheer J.J., van Laar J., *A New Type of Photoemitter*, Solid State Communications **3** (1965), 189.

[Sch00] Schmitt M., *Erzeugung energiescharfer Elektronenstrahlen*, Ph.D. thesis, Universität Heidelberg, 2000.

[Son95] Song Z., Shogen S., Kawasaki M., Suemune I., *X-ray photoelectron spectroscopy and atomic force microscopy surface study of GaAs(100) cleaning procedures*, J. Vac. Sci. Technol. B **13** (1995), 77.

[Spi58] Spicer W.E., *Photoemissive, Photoconductive, and Optical Absorption Studies of Alkali-Antimony Compounds*, Phys. Rev. **112** (1958), 114.

[Spi77] ———, *Negative Affinity 3-5 Photocathodes: Their physics and Technology*, Appl. Phys. **12** (1977), 115.

[Spr03] Sprenger F., *Production of cold electron beams for collision experiments with stored ions*, Ph.D. thesis, Universität Heidelberg, 2003.

[Sug91] Sugaya T., Kawabe M., *Low-temperature cleaning of GaAs substrate by atomic hydrogen irradiation*, Jpn. J. Appl. Phys. 2, Lett. **30** (1991), 402.

[Ter94] Terekhov A.S., Orlov D.A., *Fine structure in the spectra of thermalized photoelectrons emitted from GaAs with a negative electron affinity*, JETP Lett. **59** (1994), 864.

[Ter95] ———, *Photoelectron thermalization near the unpinned surface of GaAs(Cs,O) photocathode*, Proc. SPIE **2550** (1995), 157.

[Ter98] Terekhov A.S., *private communication*, 1998.

[Ter99a] Tereshchenko O.E., Chikichev S.I., Terekhov A.S., *Atomic structure and electronic properties of HCl-isopropanol treated and vacuum annealed GaAs(100) surface*, Appl. Surf. Sci. **142** (1999), 75.

[Ter99b] ———, *Composition and structure of HCl-isopropanol treated and vacuum annealed GaAs(100) surfaces*, J. Vac. Sci. Technol. A **17** (1999), 2655.

[Ter02] Tereshchenko O.E., Terekhov A.S., Paget D., Chiaradia P., Bonnet J.E., Belkhou R., Taleb-Ibrahimi A., *Local-order of chemically-prepared GaAs(100) surfaces*, Surf. Sci. **507-510** (2002), 411.

[Tsc98] Tschersich K.G., von Bonin V., *Formation of an atomic hydrogen beam by a hot capillary*, J. Appl. Phys. **84** (1998), 4065.

[Ueb70] Uebbing J.J., James L.W., *Behavior of cesium oxide as a low work-function coating*, J. Appl. Phys. **41** (1970), 4505.

[Var67] Varshni Y.P., *Temperature dependence of the energy gap in semiconductors*, Physica **39** (1967), 149.

[Wad90] Wada T. Nitta T., Nomura T., Miyao M., Hagino M., *Influence of Exposure to CO, CO_2 and H_2O on the Stability of GaAs Photocathodes*, Jpn. J. Appl. Phys. **29** (1990), 2087.

[Wei00] Weigel U., *Spektroskopische Verfahren zur Temperaturbestimmung an GaAs-Photokathoden*, Diplomarbeit, Universität Heidelberg, 2000.

[Yam94] Yamada M., Ide Y., *Direct Observation of Species Liberated from GaAs Native Oxides during Atomic Hydrogen Cleaning*, Jpn. J. Appl. Phys. **33** (1994), 671.

[Yam95] ———, *Anomalous behaviors observed in the isothermal desorption of GaAs surface oxides*, Surf. Sci. **339** (1995), 941.

[Yam97] Yamaguchi K., Qin Z., Nagano H., Kobayashi M., Yoshikawa A., Takahashi K., *Atomically Flat GaAs(001) Surfaces Obtained by High-Temperature Treatment with Atomic Hydrogen Irradiation*, Jpn. J. Appl. Phys. **36** (1997), L 1367.

[Zak82] Zakharchenya B.P., Mirlin D.N., Perel V.I., Reshina I.I., *Spectrum and polarization of hot-electron photoluminescence in semiconductors*, Sov. Phys. Usp. **25** (1982), 143.

Danksagung

Zunächst einmal möchte ich meinem Betreuer Prof. Dr. Andreas Wolf für die Unterstützung und das Vertrauen danken, welches mir auch in Phasen ohne erkennbaren Fortschritt entgegengebracht wurde. Ihm und Herrn Prof. Dr. Dirk Schwalm gilt zudem mein Dank für die hervorragenden Bedingungen in Ihrer Gruppe, in der ich meine Arbeit durchführen durfte.

Herrn Prof. Dr. H.-Jürgen Kluge danke ich für die freundliche Bereitschaft, das Zweitgutachten zu erstellen.

Dr. Dmitry "Dima" Orlov möchte ich besonders danken. Er war stets bereit sein reichen Schatz an Erfahrungen und Kenntnissen mit mir zu teilen. Zudem hat er durch seinen Ideenreichtum, seine Zielstrebigkeit bei steter Begeisterung für das Thema, außerordentlich zum Gelingen dieser Arbeit beigetragen.

Meinem ehemaligen Doktoranden-Kollegen Dr. Markus Hoppe danke ich für vielfältige Hilfestellungen und Diskussionen.

Herrn Prof. Dr. Alexander Terekhov danke ich für die die Fertigung der Saphir-Photokathoden in seinem Institut und die freundliche Bereitschaft sein Wissen mit mir und den anderen mit Photokathoden befassten Mitgliedern der Gruppe zu teilen.

Allen Mitglieder der Arbeitsgruppe danke ich für die von Hilfbereitschaft geprägte, angenehme Atmosphäre. Besonders erwähnen möchte ich die Kollegen aus dem Bereich des Elektronentargets, Herr Diplom-Physiker Frank Sprenger, Herr Diplom-Physiker Michael Lestinsky, sowie den ausserordentlich hilfbereiten Instituts- und Sportkollegen Herrn Diplom-Physiker Simon Altevogt. Dr. Guido Saathof danke ich sehr herzlich für die Bereitschaft meine Arbeit zu lesen und viele gute Korrekturvorschläge zu machen.

Frau Doris Cerny und Frau Helga Krieger gebührt mein Dank in organisatorischen Dingen, vor allem aber möchte ich zum Ausdruck bringen, daß mir unsere angenehmen Gespräche neben dem Mittagessen in Erinnerung sind.

Für die vielfältige und fachkundige Unterstützung der Werkstätten und der Konstruktionsabteilung des Institutes wäre vieles nicht möglich gewesen. Besonders herausheben möchte ich

dabei Herrn Mallinger und Herrn Wedel aus der Hauptwerkstatt. Herr Karl Hahn aus der Beschleunigerwerkstatt danke ich für sein stetes Bestreben auch in arbeitsreichen Zeiten immer seine Hilfe anzubieten, die mir einige Male ermöglichte kleinere Teile unter Aufsicht selbst herzustellen, was nicht nur lehrreich war, sondern auch Spass machte. Im Bereich der Konstruktion möchte ich insbesondere Herrn Weber, sowie Herrn Kantaci und Frau Buhrwitz für die Umsetzung meiner, wahrscheinlich nicht immer von Beginn an durchschaubaren, Zeichnungen in Konstruktionspläne wirklich fertigbarer Teile danken.

Einer Vielzahl von Freunden außerhalb der Physik danke ich für die nicht hoch genug einzuschätzende Hilfe insbesondere in weniger guten Zeiten aufmuntende Worte zu finden. Da ist sicher Herr Angel Chong das wohl beste Beispiel das ich anführen kann.

Besonders erwähnen möchte ich zudem meine Eltern, die mir ein Physikstudium ermöglicht haben und meine Frau Dahis, die mich bestmöglichst unterstützt hat.